Titre: Title:	Study of the solids conveying in single-screw extrusion
Auteur: Author:	Fu Huang
Date:	2002
Type:	Mémoire ou thèse / Dissertation or Thesis
Référence: Citation:	Huang, F. (2002). Study of the solids conveying in single-screw extrusion [Mémoire de maîtrise, École Polytechnique de Montréal]. PolyPublie. https://publications.polymtl.ca/7007/

UNIVERSITÉ DE MONTRÉAL

STUDY OF THE SOLIDS CONVEYING IN SINGLE-SCREW EXTRUSION

FU HUANG

DÉPARTEMENT DE GÉNIE CHIMIQUE
ÉCOLE POLYTECHNIQUE DE MONTRÉAL

MÉMOIRE PRÉSENTÉ EN VUE DE L'OBTENTION
DU DIPLÔME DE MAÎTRISE ÈS SCIENCES APPLIQUÉES (M.Sc.A)

(GÉNIE CHIMIQUE)

DECEMBER 2002

Université de Montréal

ÉCOLE POLYTECHNIQUE DE MONTRÉAL

Ce mémoire intitulé :

STUDY OF THE SOLIDS CONVEYING IN SINGLE-SCREW EXTRUSION

présenté par : HUANG Fu

en vue de l'obtention du diplôme de : Maîtrise ès sciences appliquées

a été dûment accepté par le jury composé de :

M. STUART Paul, Ph. D., président

M. LAFLEUR Pierre, Ph. D., membre et directeur de recherche

M. DUBOIS Charles, Ph. D., membre

ACKNOWLEDGMENTS

I am very grateful to my Director, Prof. Pierre Lafleur, for directing me to be thorough and independent and for offering his knowledge and experience during the course of my research. I also thank Claude Thibodeau for his suggesting and support.

I would like to thank CANPLAST CORPORATION for their financial support on this work.

I would like to acknowledge the technicians, Jacques Beausoleil, Robert Delisle, and Daniel Dumas for their considerable and continuous help with all the experiments. Additionally, my special thanks go to the people in the Chemical Engineering Department at Ecole Polytechnique de Montreal for their understanding and cooperation during my two years stay in the Department.

I am indebted to my Chinese friends, especially Ms. Zhijie Zhang, and Mr. Yunli Fang, for their encouragements, useful suggestions and helps during my study.

I would like to express my thanks to my parents, and sisters for their love and understanding.

RÉSUMÉ

Les extrudeuses mono-vis comptent parmi les pièces d'équipements les plus utilisées pour la mise en forme des polymères. Parmi les différentes zones fonctionnelles d'une extrudeuse mono-vis, la zone de transport solide joue un rôle majeur. Cependant, le mécanisme de convoyage de la matière à l'état solide n'est encore pas à ce jour complètement élucidé. Cette mauvaise compréhension est due en partie au manque d'intérêt accordé à la zone de transport solide. En effet, contrairement aux zones de fusion et de pompage, les relations entre le débit de la zone de transport solide et les conditions d'opérations (température, vitesse de la vis, pression) ont suscité peu d'études. Pour ces raisons, le développement d'un modèle capable de prédire avec acuité la pression et le profil de températures dans cette zone est nécessaire à la compréhension globale du procédé d'extrusion.

Les forces de friction entre le polymère solide et les surfaces du baril et de la vis jouent un rôle décisif dans le mécanisme de transport solide. De ce fait, la mesure du coefficient de friction est indispensable afin de modéliser adéquatement le transport solide. Dans cette optique, un dispositif expérimental nouveau a été implanté. Ce dispositif permet d'effectuer des mesures pertinentes du coefficient de friction dynamique du baril, de la vis et du polymère pour différentes conditions d'opération.

Les modèles prédictifs actuels présentant de sévères lacunes, un nouveau modèle a été développé pour simuler le transport solide. Ce modèle est basé sur une analyse bidimensionnelle des contraintes dans le lit de granules solides. Il fait intervenir deux paramètres nouveaux : le coefficient de friction interne et le module de cisaillement. Ainsi, il prend en considération le comportement en compaction du polymère et la friction dynamique.

Ce modèle a été validé à l'aide d'un plan d'expériences. Les expériences ont été réalisées en utilisant une extrudeuse miniature, spécialement conçue pour l'étude de la zone de transport solide. Le débit solide a été mesuré en fonction des conditions d'opérations pour trois formes de PVC : poudre, granules et flocons. Différentes situations de compression et différents modes de construction de la pression ont été observés. Des comparaisons entre le modèle de Broyer-Tadmor (incluant l'effet du ratio de contraintes latérales) et notre modèle ont été effectuées. Ce dernier montre un comportement plus réaliste.

ABSTRACT

The single screw extruder is the most useful piece of equipment used in the polymer processing industry. The solids conveying zone is an important section of the extruder, however, solid conveying has received less attention by extruder analysts than melting or pumping section. The lack of understanding for solid conveying was also caused by the unavailability of solids conveying rate data as a function of barrel and screw temperatures, screw speed, and discharged pressure. Developing a model capable of predicting the pressure and temperature profiles in the solids conveying zone accurately is crucial to develop a comprehensive model for the entire extrusion processing.

Friction forces between the solid polymer and barrel and screw surfaces play a decisive role in the solids conveying mechanism. Measurement of friction coefficient is an important part in modeling solids conveying. A new experimental device is designed to determine the dynamic friction coefficient of barrel, screw, and polymer surface under operating conditions found in the extrusion process.

Since almost all the previous model for the solids conveying zone are limited, a novel non-plug flow model was introduced to simulate the solids conveying. This model was based on bulk solid pellets mechanism and two-dimensional stress analysis. Two new parameters were introduced in this new model: internal friction force, and shear modulus. Taking into account the compaction behavior and dynamic coefficient phenomenon, this model could predict the behavior in the solids conveying section.

Finally, to verify the model, a special extruder that could measure solids conveying rate as a function operation conditions was built. Three shapes of PVC resin (powder, pellet, and flakes) were tested in this device. Different compressive situations, as well as

different pressure build-up were found. Comparisons between Tadmor-Broyer model with lateral stress ratios and the new non-plug solid model show a more realistic behavior for the new non-plug model.

CONTENU EN FRANÇAIS

L'extrudeuse mono - vis est de loin la pièce d'équipement la plus utilisée dans l'industrie des matières plastiques. Parmi les différentes zones fonctionnelles qui composent cet équipement, la zone de transport des solides est d'un intérêt capital pour la compréhension global du procédé d'extrusion. Cependant, contrairement aux zones de fusion et de pompage, cette zone n'a fait l'objet que de peu d'études à ce jour. Ce manque d'engouement provient en partie des difficultés rencontrées pour obtenir des données expérimentales fiables dans cette zone. Le développement d'un modèle capable de prédire avec acuité les profils de pression et de température dans la zone de transport des solides constitue donc une étape décisive pour la modélisation globale du procédé d'extrusion.

Les mécanismes intervenant dans la zone de transport des solides se sont révélés beaucoup plus complexes que la théorie originellement présentée par Darnell et Mol (1956). Darnell et Mol (1956) et Broyer et Tadmor (1972), pionniers de la modélisation du convoyage solide, considéraient en effet que les particules étaient étroitement compactées de manière à former un lit de polymère solide qui s'écoulait le long du chenal de la vis d'extrusion. Cette hypothèse est communément référée sous l'appellation d'écoulement piston. Plusieurs auteurs se sont employés à améliorer ce modèle, de manière à le rendre plus réaliste. Cependant, alors que la plupart des études réalisées étaient construites sur la base d'un modèle d'écoulement piston, Fang, Chen et Zhu (1991) ont mis en évidence l'existence de mouvements relatifs entre les particules dans la zone de transport des solides. Cette observation les a conduit à proposer un modèle d'écoulement traitant le polymère comme un ensemble de particules individuelles s'écoulant à l'intérieur du chenal à des vitesses différentes. Le modèle de Fang, Chen et Zhu (1991) est basé sur la mécanique des solides déformables. Une méthode d'éléments finis permet de résoudre le problème de manière tridimensionnelle. Ce type de

simulation conduit à des résultats plus proches des valeurs expérimentales. Cependant, la mise en œuvre mathématique du calcul numérique est trop lourde pour pouvoir donner lieu à une application industrielle immédiate. Pour cette raison, nous nous proposons dans ce travail d'introduire un nouveau modèle d'écoulement non piston, basé une analyse bidimensionnelle du champ de contraintes, et permettant de prédire le profil de pression en fonction du débit solide.

Les forces de friction entre le polymère solide et les surfaces métalliques du baril et de la vis d'extrusion jouent un rôle primordial dans le mécanisme de transport des solides. La mesure du coefficient de friction constitue donc un pré-requis nécessaire à la modélisation de ce mécanisme. Un dispositif expérimental nouveau a été développé afin de déterminer les coefficients de friction dynamique du baril, de la vis et du polymère dans des conditions de température, de pression et de vitesse de rotation similaires à celles usuellement observées en extrusion. En particulier, la détermination de la température exacte à l'interface a été évaluée numériquement en vue d'accroître la précision des mesures expérimentales. Les résultats expérimentaux obtenus pour un PVC ont montré que le coefficient de friction dynamique décroît avec la température et la pression. La vitesse de rotation, en revanche, n'a que peu d'influence sur les valeurs mesurées. Cependant, la dépendance des coefficients de friction vis - à - vis des conditions d'opération varie largement suivant la nature du polymère. De ce fait, pour un polymère différent du PVC, une simple extrapolation ne peut garantir la fiabilité des résultats.

La plupart des modèles théoriques de convoyage solide présentant certaines lacunes, nous avons introduit un modèle d'écoulement non piston complètement nouveau afin de simuler le mécanisme de transport solide. Ce modèle est basé sur une analyse bidimensionnelle des contraintes pour écoulement de particules solides élémentaires. Ce modèle fait intervenir deux nouveaux paramètres : la force de friction interne et le

module de cisaillement. Puisque le champ de vitesses de l'écoulement solide n'est pas uniforme, la friction interne joue un rôle primordial sur les mouvements relatifs entre les particules. Elle influence notamment la longueur de la zone de transport solide et dépend de la forme, de la taille, de la rigidité et des caractéristiques de surface des particules.

Afin de valider le modèle présenté, une extrudeuse spécialement conçue pour l'étude de la zone de transport solide a été utilisée. Cette extrudeuse est capable de mesurer le débit solide en fonction des conditions d'opération. Cet appareil est inspiré d'une extrudeuse conventionnelle, mais le fourreau métallique a été remplacé par un fourreau plus court équipé d'une vitre transparente. De plus, un dispositif permet d'appliquer une pression à l'extrémité du baril. Une caméra vidéo, située sur le côté de la vitre, permet une visualisation et un enregistrement de haute qualité de l'écoulement.

Trois formes de PVC (poudre, flocons et granules) ont été testées pour ce travail. Les débits solides ont été mesurés : ils dépendent d'une manière complexe des conditions d'opération et des propriétés physiques de la résine. L'effet de la pression finale sur le convoyage solide a été mis en évidence. Pour les trois formes de résine testées, le processus de compression et le comportement du solide à l'intérieur d'une extrudeuse mono - vis a été analysé pour la première fois. Les observations expérimentales indiquent que la taille des particules solides, la surface de contact entre ces particules et leurs propriétés de surface contrôlent la longueur de la zone de transport solide. Les données obtenues ont été utilisées afin de comparer les résultats numériques obtenus avec le modèle de Tadmor et Broyer (modifié pour tenir compte du coefficient de compaction latérale) et notre modèle. De plus, les propriétés physiques affectant le convoyage solide ont été mesurées et utilisées lors des simulations.

Les résultats numériques indiquent que le modèle de Tadmor et Broyer tend à sous - estimer la pressurisation et le profil de températures pour un débit solide fixé. Il semble que le fait d'inclure le coefficient de compaction latérale ne suffise pas à rendre compte de la distribution réelle des contraintes. Une analyse plus détaillée de l'anisotropie de distribution dans le solide compacté pourrait améliorer la précision des résultats. Le coefficient de compaction latérale dépend des conditions d'opération, de la forme, de la taille et des propriétés des particules de polymère.

Nous avons démontré que le modèle d'écoulement non - piston développé présentait une bonne corrélation avec les données expérimentales. Grâce à l'introduction du module de cisaillement, ce modèle permet d'obtenir un bon agrément entre les caractéristiques des particules initiales et le comportement de l'écoulement solide. À partir des résultats numériques, il a été possible de conclure que le module de cisaillement était une fonction de la pression locale, de la température et des propriétés physiques du matériau (forme, taille et propriétés de surface des granules).

TABLE OF CONTENTS

ACKNOWLEDGMENTS ..... **iv**

RÉSUMÉ ..... **v**

ABSTRACT ..... **vii**

CONTENU EN FRANÇAIS ..... **ix**

TABLE OF CONTENTS ..... **xiii**

LIST OF FIGURES ..... **xvii**

LIST OF TABLE ..... **xxi**

LIST OF APPENDIX ..... **xxii**

LIST OF SYMBOLS AND NOTATIONS ..... **xxiii**

CHAPTER 1: GENERAL INTRODUCTION **1**

1.1 Extrusion process **1**

1.2 Single screw geometry **3**

1.3 Solids conveying zone **4**

1.4 Objectives of the work **5**

CHAPTER 2: LITERATURE REVIEW **8**

2.1 Solids conveying modeling **8**

2.1.1 Conveying mechanism 8

2.1.2 Solid plug flow models 10

2.1.2.1 Darnell-Mol model (1956) 10

2.1.2.2 Broyer-Tadmor isothermal model (1972) 16
2.1.2.3 Lovegrove and Williams (1974): effect of gravitational forces 19
2.1.2.4 Tadmor-Broyer model (1972): non-isothermal model 21
2.1.2.5 Chung (1970): viscous drag model 22
2.1.2.6 Campbell and Dontula model (1995) 24
2.1.2.7 Hyun and Spalding model (1997) 27
2.1.3 Non plug flow models 30

2.2 Measurement techniques 35
2.2.1 Friction coefficient measurements 35
2.2.2 Solid bulk density measurements 39
2.2.3 Lateral stress ratio measurements 42

CHAPTER 3: FRICTION COEFFICIENT MEASUREMENT 45

3.1 Experimental method 45
3.1.1 Materials 45
3.1.2 Equipment 45
3.1.3 Procedure 48

3.2 Interface temperature calculation 49
3.2.1 Numerical calculations 49
3.2.2 Algorithm 53
3.2.3 Simulation results for the surface temperatures 54

3.3 Experimental results and discussion 58
3.3.1 Experimental plan 58
3.3.1 Speed effect for polished steel plate 60
3.3.2 Temperature effect for polished and rough steel plates 63
3.3.3 Pressure effect for polished and rough steel plates 65
3.3.4 Mechanical melting phenomena 67
3.3.5 Experiment results for PVC plate 67

3.4 COF modeling 70
3.4.1 Relations to solids conveying 70
3.4.2 Mathematic models for COF 71

3.5 Conclusion 74

CHAPTER 4: A SOLIDS CONVEYING MODEL ALLOWING MATERIAL DEFORMATION 75

4.1 Advantage of this model 75

4.2 A new non-plug solid flow model 76
4.2.1 Physical model 76
4.2.2 Two-dimensional stress analysis for polymer slices: 78
4.2.3 Stress balance on a solid conveying element: 80
4.2.4 Φ angle calculation: 81
4.2.5 Velocity profile calculation: 82
4.2.6 Flow rate calculation: 83
4.2.7 Pressure drops calculation: 84
4.2.8 Thermal effect: 85

CHAPTER 5:EXPERIMENTAL VERIFICATION 88

5.1 Introduction 88

5.2 Experimental method 88
5.2.1 Material 88
5.2.2 Experimental equipment 89
5.2.3 Experimental plan 94

5.3 Experimental results 95
5.3.1 Experimental observation of the solids conveying 95
5.3.2 Pressure measurement at the end of screw 97
5.3.3 Determination of solids conveying rate 99
5.3.3.1 Solids conveying rate for different types of screws at zero pressure 99

5.3.3.2 Solids conveying rate at different barrel T and discharged P 100

5.4 Comparison with numerical results 103
5.4.1 Parameters used in model simulations 103
5.4.2 Tadmor-Broyer model modified by lateral stress ratio 105
5.4.3 A new non-plug solid flow model 113
5.4.4 Comparison of two models 119

5.5 Conclusion 120

CHAPTER 6:CONCLUSION AND FUTURE WORKS 122

6.1 Conclusion 122

6.2 Future works 123

REFERENCE 125

APPENDIX I 130

1. Darnell-Mol model 130

2. Lovegrove and Williams model 133

3. New non-plug solid flow model 135

APPENDIX II 136

APPENDIX III 138

APPENDIX IV 139

APPENDIX V 143

LIST OF FIGURES

Figure 1.1: Shape of a typical metering type screw (Tadmor, Z., Klein, I., 1970). 2
Figure 1.2: Single-screw extruder (Broyer, E., Tadmor, Z., 1972) 4

Figure 2.1: Solid plug placed between two infinite parallel plates (Tadmor, Z., Klein, I., 1970). 9
Figure 2.2: Idealized model for the solids conveying mechanism (Tadmor, Z., Klein, I., 1970) 10
Figure 2.3: Section of the solid plug (Tadmor, Z., Klein, I., 1970). 11
Figure 2.4: Velocity vector diagram for calculating the velocity difference between barrel and solid plug (Tadmor, Z., Klein, I., 1970). 12
Figure 2.5: Forces acting on the solid plug(Tadmor, Z., Klein, I., 1970). 14
Figure 2.6: Geometry used by Broyer and Tadmor. 17
Figure 2.7: Schematic representation of (A) solid-solid friction and (B) viscous drag models (Chung, 1970). 23
Figure 2.8: Solid plug in a screw channel. (Chung, 1970) 23
Figure 2.9. Solid plug force diagram (Campbell and Dontula, 1995) 25
Figure 2.10 Forces on a differential slab 28
Figure 2.11: Physical model for non-plug solid conveying theory (Fang et al., 1991). ... 31
Figure 2.12: Relations between element (i, j) and its adjacent elements (Fang et al., 1991). 32
Figure 2.13: Stress balance on an arbitrary element (i,j) (Fang et al., 1991). 32
Figure 2.14: Schematic representation of the screw simulator (Chung et al., 1977). 37
Figure 2.15: Experimental setup for COF measurement (Gamache and al., 1999). 38
Figure 2.16: Compaction testing cell (Hyun and Spalding, 1990) 41

Figure 3.1: Schematic representation of friction measurement device. 46

Figure 3.2 Geometry used for the thermal computation. 50
Figure 3.3 Calculation algorithm for interface temperature..... 53
Figure 3.4 Polished steel plate calculation zone temperature profile underneath the sample, T_heat=55°C the interface temperature underneath the sample is: T_average = 61°C 55
Figure 3.5 Rough steel plate calculation zone temperature profile underneath the sample, T_heat=55°C the interface temperature underneath the sample is: T_average = 63°C 55
Figure 3.6 PVC plate calculation zone temperature profile underneath the sample, T_heat=45°C the interface temperature underneath the sample is: T_average = 70°C 56
Figure 3.7 Polished steel plate interface temperature as a function of time (one cycle), k=43, E_m=0.17, μ=0.37, T_{heat}=55°C, N=5rpm, P=4.03 MPa, Δt=0.06s, one cycle time=12s..... 56
Figure 3.8 Rough steel plate interface temperature as a function of time (one cycle), k=43, E_m=0.07, μ=0.48, T_{heat}=55°C, N=5rpm, P=4.03 MPa, Δt=0.06s, one cycle time=12s..... 57
Figure 3.9 PVC plate interface temperature as a function of time (one cycle), k=0.02, E_m=0.6, μ=0.54, T_{heat}=45°C, N=5rpm, P=1.95 MPa Δt=1.2s, one cycle time=12s.. 57
Figure 3.10 Statistic Experimental Result Analysis..... 60
Figure 3.11 COF as a function of screw speed for polished steel plate..... 62
Figure 3.12 COF as a function of interface temperature for polished steel plate and rough steel plate at N=8.5 rpm. 64
Figure 3.13 COF as a function of pressure for polished steel plate and rough steel plate. N=8.5 rpm. 66
Figure 3.14 COF as a function of interface temperature for PVC plate at N=8.5 rpm..... 69
Figure 3.15 COF as a function of pressure for PVC plate, N=8.5 rpm..... 69
Figure 3.16 Comparison of experimental and calculated values for f_s, f_b, and f_i at interface temperature is 60 °C..... 73

Figure 4.1 Physical model for non-plug solid conveying theory 77
Figure 4.2 Two-dimensional stress analysis 78
Figure 4.3 Stress analysis of an element for the polymer in the screw channel. 80
Figure 4.4 Algorithm for A new non-plug solid flow model 86
Figure 4.5 Numeric calculation algorithm 87

Figure 5.1 Over-all view of the solids conveying device 91
Figure 5.2 Schematic of the solids conveying device 92
Figure 5.3 Piston located at the end of the screw 93
Figure 5.4 Photo for solid conveying zone. Material, PVC pellets 96
Figure 5.5 Photo for solid conveying zone. Material, PVC powder. 97
Figure 5.6 Photo for solid conveying zone. Material, PVC flakes. 97
Figure 5.7 Section of an unwound channel: Measured pressure P(x,z); Calculated force Fx, and Fz 98
Figure 5.8 Flow rate comparison for the three shapes of PVC 102
Figure 5.9 (A) Pressure profiles, (B) Temperature profiles, (C) Density profiles for the three shapes of PVC resin by using modified Tadmor-Broyer model. N=12 rpm, P=0.21 MPa 108
Figure 5.10 (A) Pressure profiles, (B) Temperature profiles, (C) Density profiles, for PVC pellets at different operating conditions by using modified Tadmor-Broyer model. 110
Figure 5.11 Statistic analysis pareto chart of effects for lateral stress ratio K. (A) pellets (B) powder 112
Figure 5.12 Shear strain 113
Figure 5.13 (A) Pressure profiles, (B) Temperature profiles, (C) Density profiles, for three shape of PVC resin by using new non-plug solid flow model. 116
Figure 5.14 (A) Pressure profiles, (B) Temperature profiles, (C) Density profiles, for PVC pellets at different operation conditions by using new non-plug solid flow model. 117

Figure 5.15 Statistic analysis pareto chart of effect for shear modulus G. (A) pellets (B) powder 118
Figure 5.16 Comparison of pressure profiles for modified Tadmor-Broyer model and new non-plug solid flow model. 121

Figure III 3D Regression surface for plates 138
Figure IV. 1 Simulation Results 139
Figure IV. 2 Statistic analysis results of k value for PVC pellets and powder 140
Figure IV. 3 Statistic analysis results of G value for PVC pellets and powder 141
Figure V.1 Mini-screw geometry 143
Figure V.2 Screw geometry (large pitch and small pitch) 144

LIST OF TABLE

Table 2- 1 Comparison of experimental and numerical results for Darnell-Mol model (Fang, Chen and Zhu, 1991). 16
Table 2- 2 Comparison of flow rate and pressure between simulation and experiments (Fang, Chen and Zhu, 1991). 35

Table 3- 1: Physical properties of the PVC 45
Table 3- 2 Comparison of operation conditions ranges between three types plate and practical extrusion. 71
Table 3- 3 Equations used to calculate friction coefficients 72

Table 5- 1 Flow rate for different types of screws 99
Table 5- 2 Operation conditions 100
Table 5- 3 Geometric values used in simulations 103
Table 5- 4 Comparison of experimental mass temperature and simulation temperature at the end of screw 119

LIST OF APPENDIX

Table II.1: Design of experiments for polished steel plate. 136
Table II.2: Design of experiments for rough steel plate..... 137
Table II.3: Design of experiments for PVC plate. 137

Figure III 3D Regression surface for plates 138
Figure III.2 3D Regression surface for rough steel plate 138
Figure III.3 3 D Regression surface for PVC plate 138

Figure V- 1 Mini-screw geometry..... 143
Figure V- 2 Screw geometry (large pitch and small pitch)..... 144

LIST OF SYMBOLS AND NOTATIONS

A: Contact surface

C_p: Heat captivity

dP: Pressure increment

dt: time increment

dx: x direction increment

dy: y direction increment

dz: Down channel direction increment

dz_b: Distance increment of barrel surface

D: Diameter

D_b: Barrel diameter

Ds: Screw diameter

e: screw height

f_b: Coefficient of friction between polymer and barrel surface

f_s: Coefficient of friction between polymer and screw surface

f_i: Coefficient of friction between polymer and polymer

F: Force

G: Shear modulus

H: Height of screw channel

k: Lateral stress ratio

k_b: Thermal conductivity of barrel surface

k_s: Thermal conductivity of screw surface

k_p: Thermal conductivity of polymer

L: Length of screw

P: Pressure

N: Rotation speed

P_{before}: Down channel direction pressure

P_b: Pressure at barrel surface

P_s: Pressure at screw surface

q: Heat

q_{gen}: Heat generation

Q: Volume flow rate

Q_m: Mass flow rate

t: Time

T: Temperature

V_b: Barrel rotation speed

W: Width of screw channel

Z: Length of screw channel

Greek Letters

γ: Strain

$\dot{\gamma}$: Shear rate

θ: Screw angle

μ_d: Dynamic friction coefficient

ρ: Density

σ: Normal stress

τ: Shear stress

Φ: Angle of velocity to the barrel surface

CHAPTER 1: GENERAL INTRODUCTION

1.1 Extrusion process

Extrusion is probably the most important method employed to process polymers. Many well-known thermoplastic processes rely on an extrusion system to provide the heat-softened material for manipulation into finished articles. Indeed, almost all the polymers pass through an extruder at least once in the production path, from the polymerization reactor to the finished product. Injection molding, blow molding, transfer molding, and continuous thermoforming are also important plastic processing techniques.

The earliest recorded industrial "extruder" was invented by Joseph Bramah in 1795. The first screw extruder designed specially for thermoplastic materials was made by Paul Troester, in Germany, in 1935. Currently, extruders range from 2,5 to 30 mm in barrel diameter (although extruders with 90 mm barrel diameter have been built). These machines produce a tremendous variety of products at high rates: cables and wires, pipes, films, sheets, coatings, monofilaments, and various contoured profiles.

Most screw extruders in operation today are plasticating extruders. They are fed through a hopper with solid polymer in pellets, chips, beads, or powder form. The solid polymer may either be a homopolymer, a polymer blend or a compound (polymer charged with additives such as plasticizers, antioxidants, pigments, lubricants, foaming agents, or fillers).

Within the screw path, the extruder supplies heat energy to melt the polymer. There are two sources of heat energy:

➢ The hot barrel of the extruder, which is equipped with heaters, supplies thermal energy to the polymer by conduction.

➢ Mechanical energy is introduced through the rotating shaft before being converted to thermal energy by viscous dissipation.

In addition to melting the polymer, the screw extruder mixes and homogenizes the melt. Indeed, a measurement of the quality of the product is the temperature uniformity and the homogeneity of the melt leaving the extruder.

Once the polymer is melted and homogenized, it is pumped through the die at high pressure and temperature. The solids and melt are pumped forward by the relative movement of the screw and the barrel. The screw is turned by a motor through a gear box, but a thrust bearing prevents the screw from being pushed out of the barrel by the pressure that develops at the die. The screw "floats" in the barrel with a small clearance, and the polymer acts as a lubricant between the tip of the screw flights and barrel. A common type of screw is the metering screw (Figure 1.1), which comprises three geometrical sections: a deep feed section, a tapered compression or transition section, and a shallow metering section. Either right or left-handed screws may be used. Screws are made of steel and are often hardened for protection, but they wear with time.

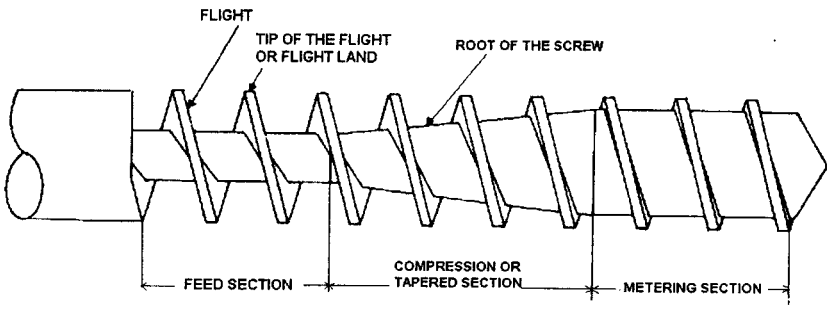

Figure 1.1: Shape of a typical metering type screw (Tadmor, Z., Klein, I., 1970).

The plasticating extruder can accomplish all these tasks despite a relative short residence time of polymer in the extruder, thus preventing the possibility of thermal degradation.

There are two types of extruders: single-screw extruders and twin-screw extruders. In this work, we will only focus on single screw extruders. The single-screw extruder is primarily a drag pump, suitable for working with highly viscous fluids, and capable of operating at the high pressures and temperatures required for processing high molecular weight polymers in their thermoplastic state. The single-screw extruder is also mechanically simple and robust, permitting high-energy inputs at relatively low speeds. It is also an effective conveyor of solids particles, at approximately the rate required by the melt section, so that gravity feeding is usually sufficient.

1.2 Single screw geometry

A typical extruder includes the following elements: a screw, a barrel (parallel cylindrical chamber in which the screw rotates and forwards the thermoplastic material), heating elements, and a cooling system. The performance of the extruder depends primarily on screw design and operating conditions.

It is customary to analyze the plasticating extrusion process as three distinct operations or functional zones: the solids conveying zone, the melting zone, and the melt conveying zone (Figure 1.2). These functional zones correspond to distinct material physical states. Initially, all the material remains solid. Then the solid and melted phases coexist. Finally, the entire polymer appears to be melted. A somewhat more careful analysis, however, reveals at least two additional functional zones: the hopper zone and the delay zone (separating the solid conveying from the melting zone).

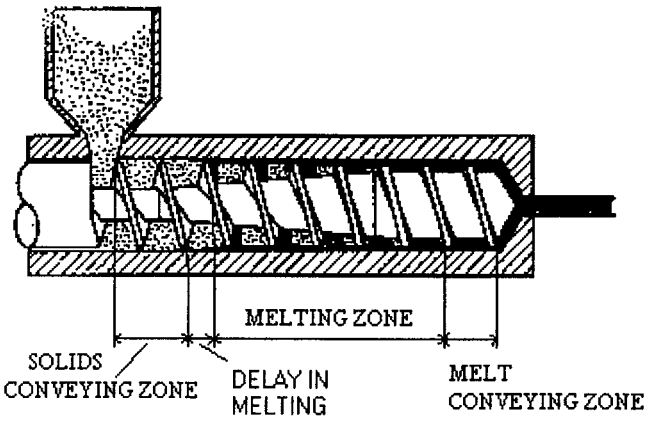

Figure 1.2: Single-screw extruder (Broyer, E., Tadmor, Z., 1972).

1.3 Solids conveying zone

The solid conveying zone is confined between the hopper zone and the delay zone, and its performance depends to a great extent on them. In the solid conveying zone, the polymer pellets are loose. They become compacted as they progress in the channel, resembling an elastic solid body. As a thin melt film occurs in the interface at the top of the solids or inner barrel wall, the delay zone begins.

There are three processes of solids conveying which are directly relevant to the performance of the extruder: gravity flow through the hopper, filling of the screw channel from the feed throat, and transport along the screw. During gravity flow, a pressure profile develops in the bulk of the material contained in the hopper. Fluctuations of the pressure at the base of the hopper lead to variations in the extrusion rate, power consumption and melt temperature. Filling of the screw may also affect the performance of the process. The feed throat must have a good cooling capacity to avoid the granules to stick to the walls, which would affect the flow stability. If the feed

pocked line is not suitable for the material being processed, this one may be forced back into the feed throat, hindering the inflow of fresh material. Finally, the flow of powdery and granular solids is affected by the geometry of the particles, the friction between particles and between particles and metal, and additional parameters such as moisture.

In the screw channel, the granules are soon compacted into a solid plug, which is conveyed forward by the frictional forces developed at the inner barrel wall, whereas the friction on the screw is the retarding force. It is important to ensure that the friction coefficient at the barrel wall is sufficiently greater than that at the screw surfaces.

1.4 Objectives of the work

The solids conveying zone has received less attention by extruder analysts than the melt-conveying zone. Friction forces between the solid polymers to barrel or screw surfaces play a decisive role in the solids conveying mechanism. Our understanding of solid-solid interfacial phenomena is extremely limited. The reliability of the solids conveying theories greatly depends on the proper selection of the coefficients of frictions. This, however, is not an easy task considering the changing conditions along the solids conveying section.

Solids conveying is also the least understood process for single-screw extruders. This lack of understanding is partly due to the unavailability of solids conveying rate data as a function of barrel and screw temperatures, screw speed, and discharged pressure.

Generally, the importance of the solids conveying zone depends mostly on the operating conditions selected. When the operation is controlled by the melt conveying capacity, solids conveying is limited to the first few turns of the screw. This results in a small pressure rise. In such a case, improvement of the mathematical model for this zone,

which should lead to a more accurate prediction of the pressure rise versus flow rate relationship, is not justified. In many cases, however, it is the solids conveying zone that controls the operation. If the barrel is cooled efficiently, a long solid conveying zone will develop relatively large pressures, increasing the delivery capacity of the extruder. In plasticating extruders, the metering section of the screw must be the rate limiting section if the extruder is to operate properly. Thus, the solid conveying and melting sections must be capable of rates that are at least equivalent to that of the metering section. If the screw geometry, process conditions, and/or resin are not properly matched, then solids conveying can become the rate limiting step, creating void regions in the transition and metering sections. These void regions can cause high extruder temperatures, which can possibly cause decomposed or cross-linked material to form and exit with the extruder, reducing the output, and leading to severe flow surging at the die. That is why developing a satisfactory theoretical model of the solids conveying zone has been one of the principal problems in accurate theoretical prediction of the performance of the whole extruder.

Solids conveying zone has proven to be considerably more complex than the theory originally presented by Darnell-Mol (1956). For Darnell-Mol model (1956) and Tadmor-Broyer model (1972) (the first generation model), the gap between the practice and theory of extrusion is unreasonably large. That means their models are far from the real situation. For Fang-Chen model (1991) (the second generation model), the predicted results are closer to the experimental values. However their theory based on elastic mechanism and finite element method, and the three-dimensional system is difficult to implement.

In this work, we will introduce a new model, which treats the polymer as a non-plug flow. This model is based on the internal stress analysis and allows the calculation of the

pressure profile for a given flow rate. The results obtained will be compared with experimental data to verify the validity of the model.

Since the coefficient of dynamic friction is the controlling factor for solids conveying, friction coefficient between polymer and barrel surface, screw surface, as well the friction coefficient between polymers are measured. A new device has been designed and fabricated to measure the friction force. This unit is capable of studying the forces resulting frictional and viscous drag on a small polymer specimen under typical conditions of extrusion.

To verify the new non-plug model, a mini-extruder has been introduced to measure solids conveying rate as a function of barrel temperature, screw speed, and discharge pressure.

CHAPTER 2: LITERATURE REVIEW

2.1 Solids conveying modeling

2.1.1 Conveying mechanism

In the solids conveying zone, the polymer particles are packed closely together to form a solid bed or plug, which slides down the helical channel. It is easier to understand the conveying mechanism if it is assumed that the screw is stationary and the barrel rotates.

The simplest model assumes a solid plug in motion, confined between two infinite parallel plates moving relative to each other (Figure 2.1). The upper plate moves with a velocity v and the plug moves in the same direction with a velocity u.

The driving force of the movement of the plug is the friction force between the barrel surface and the solid plug:

$$F_b = P.A_b.f_b \qquad 2\text{- }1$$

The friction forces between the screw and the plug, on the other hand, retard the motion of the plug and are given by:

$$F_s = P.A_s.f_s \qquad 2\text{- }2$$

There are three alternative end results to such a model:

- If $F_s > F_b$: the plug will decelerate to a complete stop.
- If $F_s < F_b$: the plug will accelerate until it reaches the velocity of the upper plate.

➢ If $F_s = F_b$: the plug may move with any velocity u, with $0 < u < V_b$.

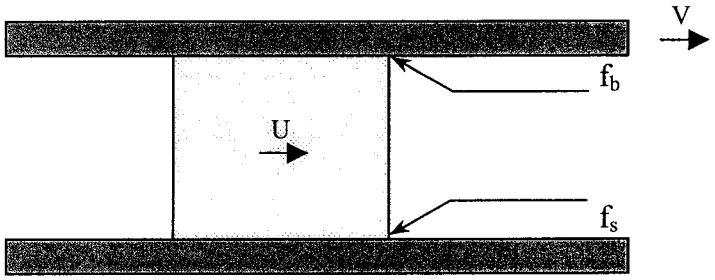

Figure 2.1: Solid plug placed between two infinite parallel plates (Tadmor, Z., Klein, I., 1970).

Of course, this model cannot explain the conveying mechanism in extrusion. A somewhat more elaborate model would be a moving solid plug confined in a rectangular channel (Figure 2.2). The upper plate moves with a constant velocity V_b at an angle θ to the down channel direction, while the plug slides with velocity u down the channel.

The force exerted by the upper plate representing the barrel on the plug is still given by equation 2-1, but it acts in a direction θ to the down channel direction. If the plug has a particular velocity u in the down channel direction, F_b in direction z will be:

$$F_{bz} = A_b f_b P \cos(\theta + \phi) \qquad 2\text{-}3$$

The retarding force in the channel (neglecting the flights) remains is given by equation 2-2.

The normal force is:

$$F^* = F_b \sin(\theta + \phi) \qquad 2\text{-}4$$

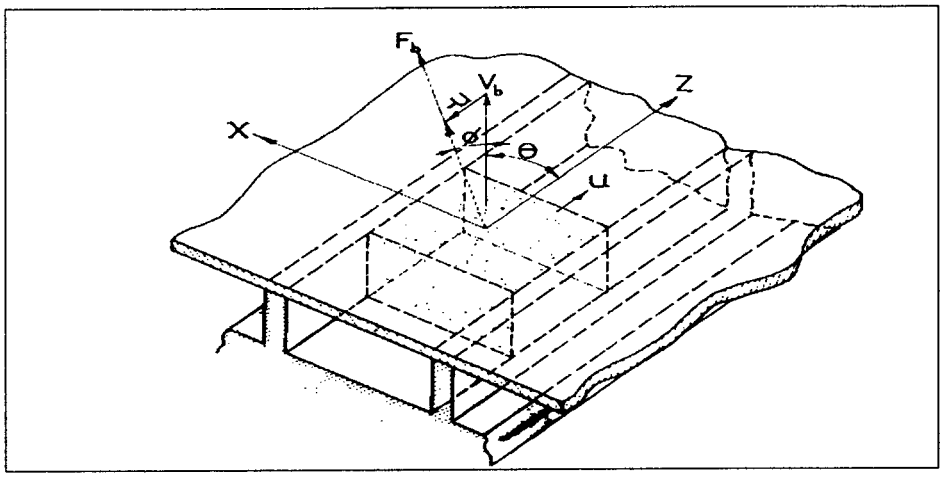

Figure 2.2: Idealized model for the solids conveying mechanism (Tadmor, Z., Klein, I., 1970).

2.1.2 Solid plug flow models

2.1.2.1 Darnell-Mol model (1956)

Darnell and Mol (1956) are the pioneers of the solids conveying theory. Despite its simplicity, their model provides a convenient tool for understanding and optimizing the process. This model assumes that the polymer particles in the solids conveying zone are packed closely together and form a solid bed, or plug, which slides along the down channel. The driving force for the movement of the plug is the friction force between the barrel surface and the solid plug. The friction forces between the screw and the plug, on the other hand, retard the motion of the plug.

The velocity of the plug in the down channel direction at the barrel surface is:

$$V_{pz} = \frac{V_{pl}}{\sin \theta_b} \qquad 2\text{-}5$$

The velocity of the plug at the barrel surface in the tangential direction is:

$$V_{p\theta} = \frac{V_{pl}}{\tan\theta_b} \qquad 2\text{-}6$$

The velocity components in down channel and tangential directions are shown in Figure 2.3.

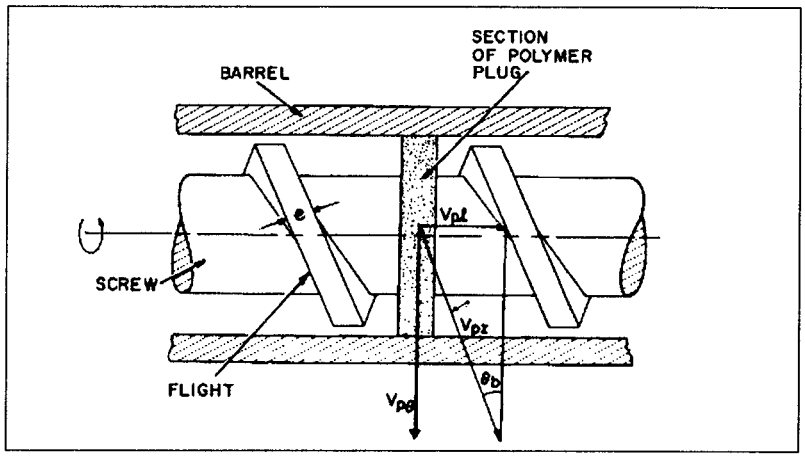

Figure 2.3: Section of the solid plug (Tadmor, Z., Klein, I., 1970).

The flow rate can be expressed in term of the velocity of the plug in the axial direction V_{pl}:

$$Q_s = V_{pl} * \left[\frac{\pi}{4} * (D_b^2 - D_s^2) - \frac{peH}{\sin\bar{\theta}} \right] \qquad 2\text{-}7$$

Where D_b and D_s are the diameters at the root of the screw and at the channel surface, e is the flight width, $\bar{\theta}$ is the average helix angle, and p is the number of flights in parallel.

The friction forces acting between the plug and the barrel depend on the angle Φ, at which the plug moves relative to the barrel (Figure 2.4).

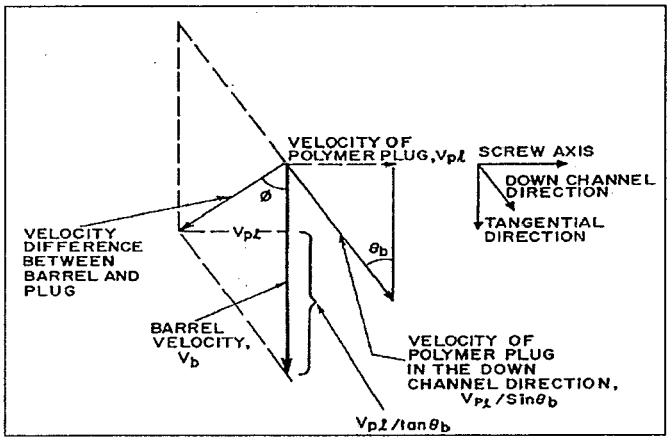

Figure 2.4: Velocity vector diagram for calculating the velocity difference between barrel and solid plug (Tadmor, Z., Klein, I., 1970).

From Figure 2.4, it is easy to get the following relationship for angle Φ:

$$\tan\phi = \frac{V_{pl}}{V_b - V_{pl}/\tan\theta_b} \qquad 2\text{-}8$$

With:

$$V_b = \pi.N.D_b \qquad 2\text{-}9$$

Rearranging equation 2-8 gives:

$$V_{pl} = V_b \frac{\tan\phi * \tan\theta_b}{\tan\phi + \tan\theta_b} \qquad 2\text{-}10$$

Substituting Eq. 2-.10 into Eq. 2-7:

$$Q_s = \pi.N.D_b.\frac{\tan\phi * \tan\theta_b}{\tan\phi + \tan\theta_b}.\left[\frac{\pi}{4}(D_b^2 - D_s^2) - \frac{peH}{\sin\bar{\theta}}\right] \qquad 2\text{-}11$$

With:

$$D_b^2 - D_s^2 \approx 4H(D_b - H) \qquad 2\text{-}12$$

And:

$$\overline{W} = \frac{\pi}{p}(D_b - H)\sin\overline{\theta} - e \qquad 2\text{-}13$$

Using Eq. 2-12 and Eq. 2-13, Eq. 2-11 can also be written as below:

$$Q_s = \pi^2 NHD_b(D_b - H)\frac{\tan\phi * \tan\theta_b}{\tan\phi + \tan\theta_b}\left(\frac{\overline{W}}{\overline{W} + e}\right) \qquad 2\text{-}14$$

Angle Φ can be obtained from the force and torque balance on a solid plug. Before discussing the forces acting on the solid, the assumptions used in Darnell-Mol model will be listed:

- General assumptions:

  The solid polymer in the screw channel behaves like a continuum. The plug contacts all sides of the channel, i.e., barrel surface, root of the screw, and both flights.

- Geometrical assumptions:

  The channel depth is constant. The flight clearance can be neglected.

- Cinematic assumptions: the velocity of the polymer is constant in time and uniform in space. This is sometimes referred to as plug flow.

- Physical assumptions:

  Gravitational forces are neglected. Density changes in the plug are neglected. The coefficient of friction is independent of pressure but may be a function of temperature.

- Pressure assumptions:

  The pressure is a function of the down channel direction only (P=P(z)).

Figure 2.5 shows the forces acting on the plug for a stationary screw and a rotating barrel.

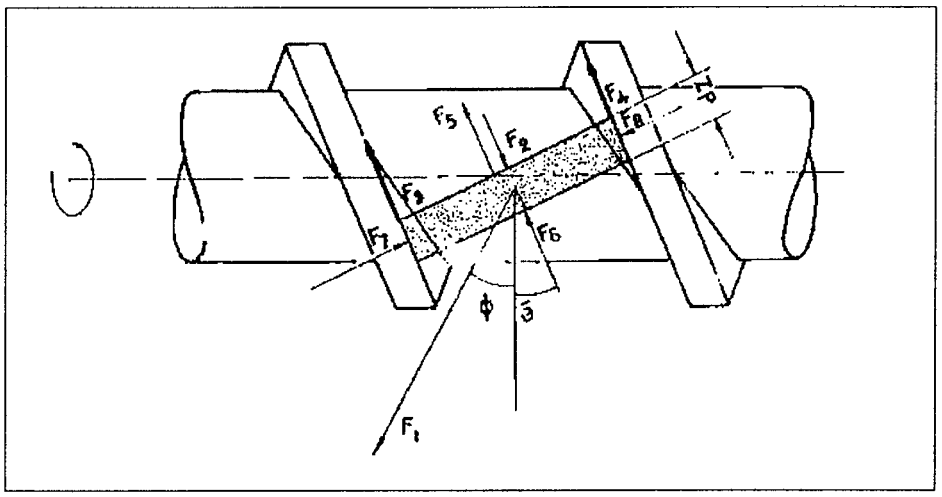

Figure 2.5: Forces acting on the solid plug (Tadmor, Z., Klein, I., 1970).

On Figure 2.5:

- F_1 represents the friction between the barrel surface and the plug.
- F_6 and F_2 are forces due to the pressure drop in the down channel direction.
- F_3, F_4, and F_5 are respectively the friction forces on the two flights and on the root of the screw.
- F_7 and F_8 are the normal forces exerted by the flights on the plug.

Angle Φ can be obtained from a force and torque balance analysis (Appendix 1):

$$\cos\phi = K\sin\phi + 2\frac{H}{W_b}\frac{f_s}{f_b}K\sin\theta_b + \frac{f_s}{f_b}\frac{W_s}{W_b}K\sin\theta_b + 2\frac{H}{W}\frac{f_s}{f_b}\frac{\overline{D}}{D_b}\sin\theta_b\cot an\overline{\theta}$$
$$+\frac{W_s}{W_b}\frac{f_s}{f_b}\frac{D_s}{D_b}\sin\theta_b\cot an\theta_s + \frac{\overline{W}}{W_b}\frac{H}{z_b}\frac{1}{f_b}\left(K\sin\overline{\theta} + \frac{\overline{D}}{D_b}\cos\overline{\theta}\right)\ln\frac{P_2}{P_1} \qquad 2\text{- }15$$

With:

$$K \equiv \frac{\overline{D}}{D_b}\left(\frac{\sin\overline{\theta} + f_s\cos\overline{\theta}}{\cos\overline{\theta} - f_s\sin\overline{\theta}}\right) \qquad 2\text{-}16$$

For a down channel distance z_b, the pressure profile can also be obtained from the force and torque balance:

$$P = P_1 \exp\left[\left(\frac{B_1 - A_1K}{B_2 + A_2K}\right)z_b\right] \qquad 2\text{-}17$$

With:

$$A_1 = f_bW_b\sin\phi + 2Hf_s\sin\theta_b + W_sf_s\sin\theta_b \qquad 2\text{-}18$$

$$A_2 = H\overline{W}\sin\overline{\theta} \qquad 2\text{-}19$$

$$B_1 = f_bW_b\cos\phi - 2Hf_s\sin\theta_b\cot an\overline{\theta}\frac{\overline{D}}{D_b} - W_sf_s\sin\theta_b\cot an\theta_s\frac{D_s}{D_b} \qquad 2\text{-}20$$

$$B_2 = H\overline{W}\cos\overline{\theta}\frac{\overline{D}}{D_b} \qquad 2\text{-}21$$

The pressure rises exponentially from an initial value P_1 to a final value P at z_b. Eq. 2-17 indicates that the pressure at the end of the zone depends on the pressure P_1 at the beginning of the screw. With this model, the calculation of the pressure profile or pressure rise is possible only if the value P_1 is known (P_1 being positive).

The results computed using the Darnell-Mol model are far from the real situation, especially for pressure build-up, as shown in Table 2.1.

Table 2- 1 Comparison of experimental and numerical results for Darnell-Mol model (Fang, Chen and Zhu, 1991).

N (rpm)	Q_s (kg/min)		P (MPa)	
	Experimental	Darnell-Mol	Experimental	Darnell-Mol
31	9.45	20.79	13.8	$2.13*10^5$

Darnell-Mol model is based on the static equilibrium of the solid-to-solid friction forces, and assumes that the flow of the polymer solid in the screw channel is controlled by the frictional forces between the solid plug and surrounding screw and barrel surface. The assumption of solid-to-solid friction implies that the solid polymer does not melt for a substantial period of time. This assumption is far from the real situation.

2.1.2.2 Broyer-Tadmor isothermal model (1972)

Broyer-Tadmor model (1972) presented a modified Darnell-Mol model (1956). While the original model describes the solid flow in a constant depth channel assuming a homogeneous and isotropic plug, Broyer-Tadmor model takes into account the degree of taper of the channel, the non-isotropic nature of the pressure distribution, and the changing density of the solid plug. The model is based on the following assumptions:

- General assumptions:

  The solid plug, formed by the compacted pellets or powder, behaves like a continuous elastic plug. The plug contacts all parts of the channel, i.e. barrel surface, root of the screw and both flights. Gravitational forces in the channel are neglected.

- Geometrical assumptions:

  The flight clearance is neglected. Taper is constant.

- Pressure assumptions:

Following Schneider's work (1969), the compacted pressure (or stress) is anisotropic in the plane perpendicular to the flight, and a certain ratio (K) of normal stresses is assumed. According to this assumption, the pressure on barrel, flights and root of the screw have different values but are proportional to the pressure in the down channel direction, P:

$$\begin{cases} P_b = K_b.P \\ P_f = K_f.P \\ P_s = K_s.P \end{cases} \qquad 2\text{-}22$$

Where K_b, K_f and K_s are respectively the lateral stress ratio on barrel, flights and root of the screw.

- Physical assumptions:

  The frictions coefficients are constant but may have different values on the screw and barrel surface. Density is assumed to be constant in small down channel increments. Any change in the density could be calculated as a function of the temperature and pressure values in the down-channel direction.

The geometry used by Broyer and Tadmor is shown on Figure 2.6.

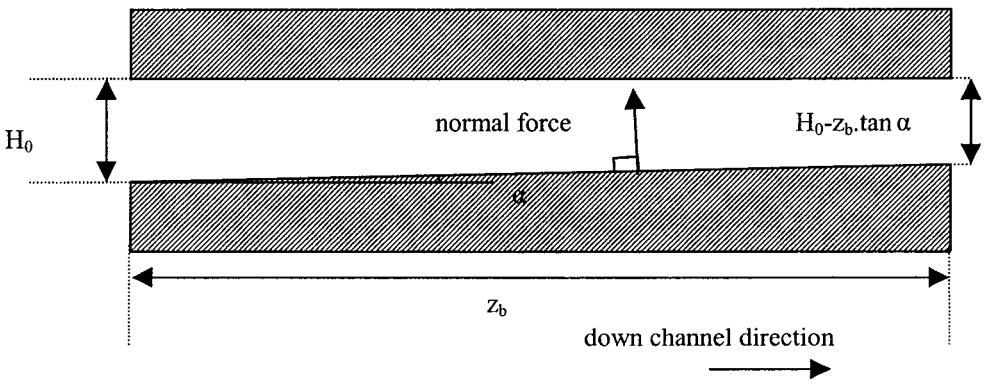

Figure 2.6: Geometry used by Broyer and Tadmor.

The forces and torques balance lead to the following expression:

$$P_2 = P_1 \exp\left[\int_{Z_{b1}}^{Z_{b2}} \frac{B_1 - A_1 K}{A_2 K + B_2} dZ_b\right] \qquad 2\text{-}23$$

With:

$$A_1 = W_b f_b K_b \sin\phi - W \tan\alpha * \sin\theta + 2\overline{H} K_f f_s \sin\theta_b + W_s f_s K_s \sin\theta_b \left(\cos\alpha + \frac{\sin\alpha}{f_s}\right)$$

2- 24

$$A_2 = H\overline{W} \sin\overline{\theta} \qquad 2\text{-}25$$

$$B_1 = W_b f_b K_b \cos\phi + \overline{W} \tan\alpha * \cos\overline{\theta} \frac{\overline{D}}{D_b} - W_s K_s f_s (\cos\alpha + \frac{\sin\alpha}{f_s}) \sin\theta_b * \cot an\theta_s \frac{D_s}{D_b}$$

2- 26

$$B_2 = \overline{W} H \cos\overline{\theta} \frac{\overline{D}}{D_b} \qquad 2\text{-}27$$

And:

$$K = \frac{\overline{D}}{D_b} * \frac{\sin\overline{\theta} + f_s \cos\overline{\theta}}{\cos\overline{\theta} - f_s \sin\overline{\theta}} \qquad 2\text{-}28$$

If the channel has constant depth (α=0) and if bulk density is assumed to be constant, Eq. 2-23, can be integrated and we obtain the Darnell-Mol model for K_b=K_s=K_f=1.

The main contributions of this model are:

- Calculations in variable channel depth section. It can be noticed that pressure rise in a tapered channel is higher than in a parallel channel, and the pressure profile increases with increasing values of taper angle.
- The effect of the non-isotropic pressure distribution on the pressure profile is investigated.

2.1.2.3 Lovegrove and Williams (1974): effect of gravitational forces

From Darnell-Mol model, we know that pressure build-up results from frictional forces acting on the material. These forces depend directly upon the existing pressure. Therefore:

$$\frac{dP}{dz} = \frac{A}{D} P \qquad 2\text{-}29$$

Where A is a dimensionless function of screw geometry, coefficients of friction and flow rate, D is the screw diameter and z is the distance along the channel. Thus, if P_0 is the initial pressure at z=0, one obtains:

$$P = P_0 * e^{Az/D} \qquad 2\text{-}30$$

Lovegrove and Williams (1974) analyzed the pressure generation in the feed section of an extruder. They analyzed the effects of both gravitational and centrifugal forces that can become significant at high screw speed.

When centrifugal forces are included, the basic differential Eq. 2-29 becomes:

$$\frac{dP}{dz} = \frac{AP}{D} + Gw\left(\frac{D\omega^2}{g}\right) \qquad 2\text{-}31$$

With:

$$G = h_1 A_3 - h_2 A_1 \qquad 2\text{-}32$$

And:

$$h_1 = \frac{C^{1/k-1}\left(\frac{1-C^3}{1-C^{1/k}}\right) - 3kC^2}{12(3k-1)} \qquad 2\text{-}33$$

$$h_2 = \frac{C^{1/k-1}\left(\frac{1-C^3}{1-C^{1/k}}\right) - 3k}{12(3k-1)} \qquad 2\text{-}34$$

Where w is the specific weight of the polymer, and parameters A_1, A_3, and C are given in the complete development in Appendix I.

When gravity forces are included for a vertical screw, the influence of gravity forces is obviously independent of z and the basic differential Eq.2.29 becomes

$$\frac{dP}{dz} = \frac{AP}{D} + Bw \qquad 2\text{-}35$$

B is another function of screw geometry and coefficients of friction. The form of pressure change produced is found from the integration of Eq.2-35:

$$P = P_0 * e^{Az/D} + \frac{B}{A}(e^{Az/D} - 1)wD \qquad 2\text{-}36$$

Lovegrove and Williams (1974) concluded that gravitational forces must be taken into account, since they provide the necessary conditions for pressure initiation. They showed that gravitational forces in the channel are significant compared with pressure from the hopper, and may even be a dominant factor in starting off a pressure build-up along the screw.

Considering that changes in density and temperature become significant only when fairly high pressures are produced, Broyer-Tadmor (1970) model may be applied as the pressure has built up such that P>>*w*D. Gravity forces in the channel rather than pressure from the hopper should be looked upon as starting off the process.

2.1.2.4 Tadmor-Broyer model (1972): non-isothermal model

Based on Broyer-Tadmor modified isothermal model (1970), Broyer and Tadmor (1972) developed a non-isothermal model. They pointed out that the surface temperature of the solid plug increases along the channel because of the friction. The friction coefficients, that are thermosensitive, can be strongly affected, leading to a modification of the pressure profile.

Broyer and Tadmor (1972) developed a mathematical model allowing the computation of the temperature profile in the solid plug and the interacting pressure profile. They showed that an exponentially increasing pressure led to an exponentially (or nearly exponentially) increasing surface temperature. The surface temperature increases only until the melting point of the polymer. At this point, no more solid-solid friction exists on the barrel surface.

The rate of heat generation per unit barrel surface, $q_{b,,}$ is calculated as:

$$q_b = P_b . f_b .. \pi . N . D_b . \frac{\sin \theta_b}{\sin(\theta_b + \phi)} \qquad 2\text{-}37$$

Where N is the screw speed, D_b is the inner diameter of the barrel and θ_b is the helix angle on the barrel surface. This equation indicates that the rate of heat generation is directly proportional to the local pressure. Neglecting heat fluxes on the flights and on the root of the screw, the heat transfer problem becomes a one-dimensional heat conduction problem. Assuming a coordinate system located at the interface polymer/barrel (with the y direction pointing to the solid plug), the heat transfer problem is governed by the following equation:

$$\frac{\partial T_p}{\partial t} = \alpha_p \frac{\partial^2 T_p}{\partial y^2} \qquad 2\text{-}38$$

In this equation, T_p is the temperature of the plug and α_p is the thermal diffusivity.

The heat generation on the barrel surface, given in Eq. 2-37 is dissipated into two fluxes: the first flux conducts heat into the solid plug while the second conducts heat away through the barrel walls. Thus:

$$q_b(n) = -k_p(\frac{\partial T_p}{\partial y})_{y=0} + k_b(\frac{\partial T_b}{\partial y})_{y=0} \qquad 2\text{-}39$$

Where k_p and k_b are the thermal conductivities of polymer plug and barrel metal, respectively. The latter being between one to two orders of magnitude larger than the former, it can be safely assumed that temperature gradients in the barrel metal are linear, i.e., barrel temperature changes linearly from the interface temperature T_p (0,n) to the barrel outside temperature.

To compute the temperature profile of the plug surface, a heat balance is made on a thin slice of the plug cut perpendicular to the flights. Changes in the temperature in this slice are calculated as a function of time. Since the down-channel velocity of the plug is known, changes of temperature with time can be converted as a function of down-channel distance. With the time evaluation of P_b, f_b, angle Φ, and bulk density, using a slab method, the temperature for the plug surface can be calculated numerically.

2.1.2.5 Chung (1970): viscous drag model

Instead of the solid-to-solid friction mechanism, which is the basic assumption of Darnell-Mol model (1956), Chung (1970) proposed the existence of a viscous drag mechanism and set up a new mathematical model for solids conveying. Figure 2.7 compares the two mechanisms. Figure 2.8 shows the solid plug within the screw channel, and the forces acting on it.

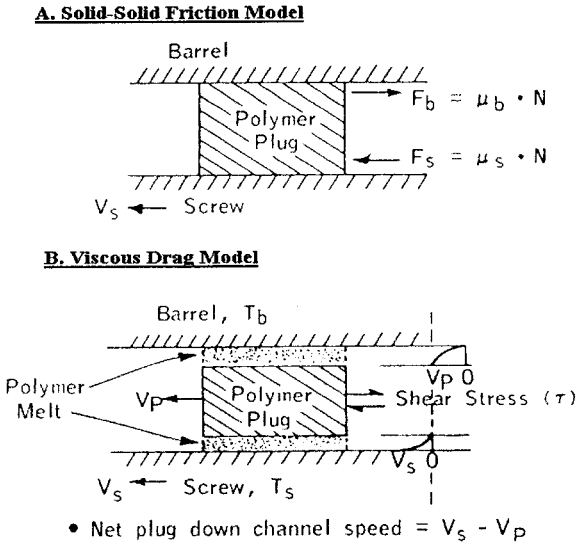

Figure 2.7: Schematic representation of (A) solid-solid friction and (B) viscous drag models (Chung, 1970).

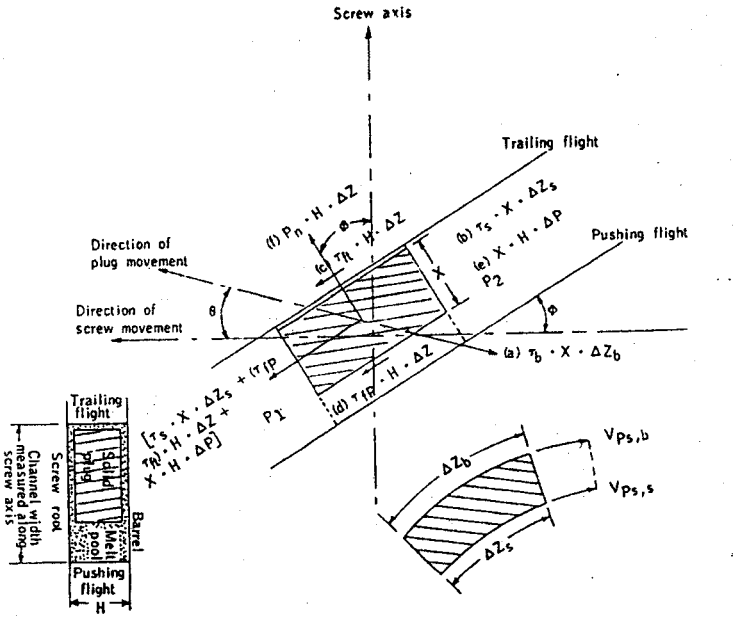

Figure 2.8: Solid plug in a screw channel (Chung, 1970).

Chung (1970) considers that the solid-to-solid model is correct for the first several turns of a screw whose surface temperatures remain below the polymer melting point. However, the barrel temperature is expected to be at a higher temperature, and there is polymer melt between screw flights and solid plug and barrel and solid plug. Referring to Figure 2.7 (B) and Figure 2.8, the four sides of solid plug are completely surrounded by polymer melt. Three of the plug sides, facing the barrel, the root of the screw, and the trailing side of the flight, are covered with a thin layer of polymer melt. The fourth side of the plug, facing the push side of the flight, is in contact with the melt pool collected between the plug and the pushing flight.

Based on the forces balance on the solid plug with a viscous drag model, Chung (1970) developed a mathematical model to predict pressure build-up of the solid conveying zone. This solids conveying model can be easily combined with existing melting and metering models, making a complete mathematical package for plasticating screw extrusion.

2.1.2.6 Campbell and Dontula model (1995)

Campbell and Dontula developed a theory, which is based on an assumption that the solids are pushed up the barrel by the flights on the screw. The physical diagram is similar to Darnell-Mol model (Figure 2.5). The following assumptions are the same as Darnell-Mol model:

- The solid plug is always in contact with all surfaces of the channel;
- The flight clearances are to be neglected;
- The coefficients of friction are constant but can be different for the barrel screw core, and screw helix;

- The density is assumed to be constant;
- The temperature is assumed to be constant.

The three assumptions that are different in Campbell-Dontula model are:

- The screw is being rotated instead of the barrel;
- The bed of compressed pellets or powder will be treated as an elastic fluid;
- The force on the plug due to the advancing flight is a combination of the pressure force F_7, which is the same force used in Darnell-Mol model, and a normal force F_N which is assumed to be proportional to the frictional force exerted by the pellets as they move relative to the barrel.

Thus, in Campbell and Dontula's analysis, there is not a torque balance since the bed is considered to be a fluid and due to the assumption of the origin of the normal force authors do not have determine the force F* as Darnell-Mol model. (See appendix I-1.)

The volumetric flow rate is the same as the Darnell-Mol mode. (Equation 2-14.) The angle Φ is obtained using a force balance on the plug as indicated in figure 2-9

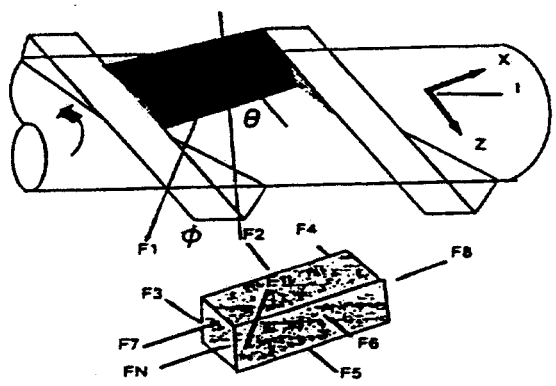

Figure 2.9. Solid plug force diagram (Campbell and Dontula, 1995).

F_1 is the force exerted on the barrel by the plug:

$$F_1 = f_b P W_b dz_b \qquad 2\text{-}40$$

The net down channel pressure force due to F_2 and F_6 will be:

$$F_P = (F_6 - F_2) = H\overline{W}dP \qquad 2\text{-}41$$

The pressure forces exerted at the flight-plug surface are thus:

$$F_7 = PHd\bar{z} \qquad 2\text{-}42$$

$$F_8 = PHd\bar{z} \qquad 2\text{-}43$$

The normal force will then be:

$$F_N = f_b P W_b dz_b \qquad 2\text{-}44$$

The total force on the advancing flight will be:

$$F_3 = (F_7 + F_N) f_H \qquad 2\text{-}45$$

and the total force on the receding flight:

$$F_4 = F_8 f_H \qquad 2\text{-}46$$

The force on the core is defined as:

$$F_5 = f_c P W_c dz_c \qquad 2\text{-}47$$

It should be pointed out that F_1 and F_N are represented by the same quantities. This is due to the nature of frictional forces, which are independent of direction and velocity for a given surface area and resultant normal force. Using these forces, a force balance in the axial direction or the "l" direction, see figure 2-9, will lead to the following equation:

$$-F_l \sin\phi - F_P \sin\overline{\theta} + F_N \cos\theta_b - (F_7 f_H \sin\overline{\theta} + F_N f_H \sin\theta_b) - F_4 \sin\overline{\theta} - F_5 \sin\theta_s = 0 \qquad 2\text{-}48$$

Substituting equation 4-40 to 4-47 into equation 2-48 and remembering that

$$\sin\theta_b = \frac{d\bar{z}}{dz_b}\sin\bar{\theta} \text{ and } \sin\theta_b = \frac{dz_c}{dz_b}\sin\theta_c \qquad 2\text{-}49$$

One obtains the following differential equation:

$$(-f_b W_b \sin\phi + f_b W_b \cos\theta_b - Hf_H \sin\theta_b - f_H f_b W_b \sin\theta_b - Hf_H \sin\theta_b - W_c f_c \sin\theta_b)dz_b - H\overline{W}\sin\bar{\theta}\frac{dP}{P} = 0 \qquad 2\text{-}50$$

One can integrate from z_b=0 to z_b=Z and from P_0 to P_z, and simplify to obtain:

$$\sin\phi = \cos\theta_b - (2\frac{Hf_H}{W_b f_b} + f_H + \frac{W_c f_c}{W_b f_b})\sin\theta_b - \frac{H\overline{W}\sin\bar{\theta}}{W_b f_b Z}\ln\frac{P_z}{P_0} \qquad 2\text{-}51$$

This model avoids the complexity introduced by the additional parameters.

2.1.2.7 Hyun and Spalding model (1997)

Hyun and Spalding described a model that treats the solid bed as a rigid body, applies a one dimensional force balance like Darnell and Mol model, and includes a two-dimensional torque balance and thermal effects, and applies realistic physical property data.

The volumetric conveying rate, Q, is the same as the Darnell-Mol model (Equation 2-14). The solids forwarding angle Φ is computed from a force and torque balance. The forces acting on a differential slab perpendicular to the flight edge are shown by figure 2.10.

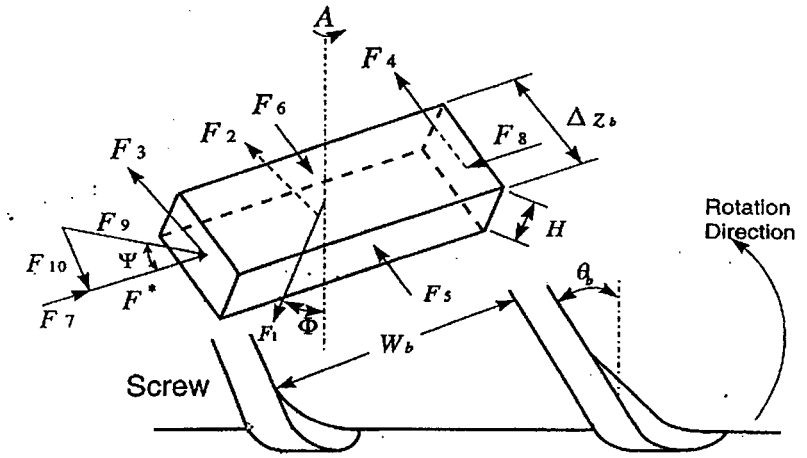

Figure 2.10: Forces on a differential slab.

The forces are identical to those used by Darnell-Mol model except that the force F_9 is acting at an angle Ψ to the flight edge; F_9 is resolved into F* and F_{10}. A force balance in the axial direction for the slab is as following:

$$-F_1 \sin\phi - F_2 \sin\theta_s - (F_3 + F_4 - F_{10})\sin\bar{\theta} - (F_5 - F_6)\sin\bar{\theta} + F^* \cos\bar{\theta} = 0 \qquad 2\text{-}52$$

From figure 2.10, one can easily obtain:

$$F_1 = Kf_b PW_b \Delta z_b \qquad 2\text{-}53$$

$$F_2 = Kf_s PW_s \Delta z_b \frac{\sin\theta_b}{\sin\theta_s} \qquad 2\text{-}54$$

$$F_3 = f_s(F_7 + F^*) \qquad 2\text{-}55$$

$$F_4 = f_s F_8 \qquad 2\text{-}56$$

$$F_5 - F_6 = \Delta PH\overline{W} \qquad 2\text{-}57$$

$$F_7 = KPH\Delta z_b \frac{\sin\theta_b}{\sin\theta} \qquad 2\text{-}58$$

Where K is the lateral stress. Substituting the equation 2-53 to 2-58 into equation 2-52, one obtains the following:

$$-Kf_b PW_b \Delta z \sin\phi - Kf_s PW_s \Delta z \frac{\sin\theta_b}{\sin\theta_s}\sin\theta_s - 2Kf_s PH\Delta z \frac{\sin\theta_b}{\sin\theta}\sin\bar{\theta} \\ -\Delta PH\overline{W}\sin\bar{\theta} + F^*\cos\theta = 0 \qquad 2\text{-}59$$

A balance of the torques about axis of the screw was performed as following:

$$\frac{D_b}{2}F_1\cos\phi - \frac{D_s}{2}F_2\cos\theta_s - \frac{\overline{D}}{2}(F_3 + F_4 - F_{10})\cos\bar{\theta} \\ -\frac{\overline{D}}{2}(F_5 - F_6)\cos\bar{\theta} - \frac{\overline{D}}{2}F^*\sin\bar{\theta} = 0 \qquad 2\text{-}60$$

where $\overline{D}$ is the average of the screw root and barrel diameters. Substituting the force component equations into equation 2-60, one obtains:

$$D_b Kf_b PW_b \Delta z\cos\phi - D_s Kf_s PW_s \Delta z\frac{\sin\theta_b}{\sin\theta_s}\cos\theta_s - 2\overline{D}f_s KPH\Delta z\frac{\sin\theta_b}{\sin\theta}\cos\bar{\theta} \\ -\overline{D}\Delta PH\overline{W}\cos\bar{\theta} - \overline{D}F^*\sin\bar{\theta} = 0 \qquad 2\text{-}61$$

Like Darnell-Mol model, F* was eliminated by combining equation 2-59 and 2-61:

$$\cos\phi = M\sin\phi + 2\frac{Hf_s}{W_b f_b}\sin\theta_b\left[M + \frac{\overline{D}}{D_b}\cot\theta\right] \\ +\frac{W_s f_s}{W_b f_b}\sin\theta_b\left[M + \frac{D_s}{D_b}\cot\theta_s\right] + \frac{\overline{W}H}{Kf_b PW_b}\sin\bar{\theta}\left[M + \frac{\overline{D}}{D_b}\cot\bar{\theta}\right]\frac{\partial P}{\partial z} \qquad 2\text{-}62$$

where

$$M = \frac{\overline{D}}{D_b}\tan\bar{\theta} \qquad 2\text{-}63$$

Equation 2-62 is identical to Darnell-Mol model's equation 2-15 except that the equation is in differential form, includes the lateral stress ratio K, and the M term. The term M here depends only on screw geometry.

2.1.3 Non plug flow models

The plug flow models presented previously suffer from several shortcomings:

- They do not predict the velocity variation.
- They need an initial non-zero pressure. However, the actual conditions are quite different.

Fang, Chen and Zhu (1991) designed an extruder with a barrel equipped with glass windows. Their experiments demonstrated the existence of relative movements between the pellets in the former part of the screw feed zone. This observation, which was not in agreement with the basic thinking of the solid plug theory, allowed them to propose a non solid plug flow model. In this model, Fang, Chen and Zhu (1991) consider the solid material in the screw channel as bulk pellets. This assumption is closer to the real conditions.

The basic assumptions proposed by Fang, Chen and Zhu (1991) are the following:

- General assumptions:

The solid conveying process is steady. The barrel is treated as rotating opposite to the stationary screw. Gravitational forces are neglected.

- Physical assumptions:

The pellets can be treated as a linear elastic system, since the stress-strain relationships satisfy the equations of linear elasticity. Bulk pellets may to compressive forces but not to tensile forces. Internal friction, which is dominant over the relative motion between the pellets, is taken into account

- Geometrical assumptions:

The screw curvature is neglected.

➢ Cinematic assumptions:

The pellets only flow in down channel direction (z). Transverse flows (x and y directions) are neglected. A multi-dimensional velocity profile is assumed.

➢ Pressure assumptions:

The pressure distribution is anisotropic.

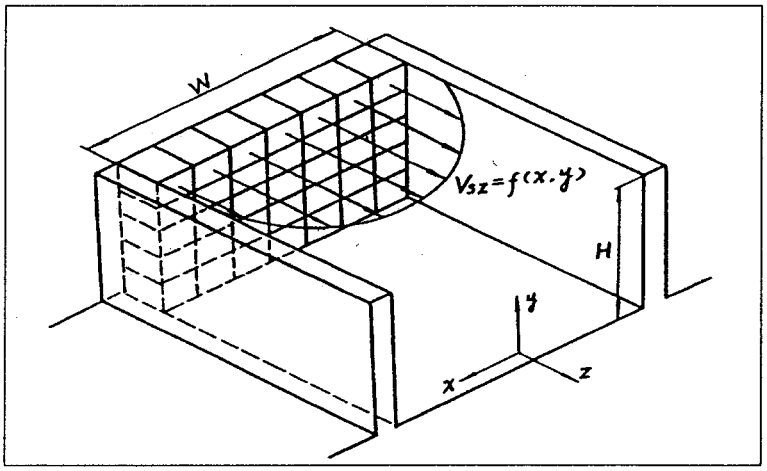

Figure 2.11: Physical model for non-plug solid conveying theory (Fang et al., 1991).

In this non-plug solids conveying model, the friction shear stress satisfy Coulomb's law of friction:

$$\tau = f.\sigma \qquad 2\text{-}64$$

Where τ is the frictional shear stress, σ is the compressive stress, and f is the friction coefficient. f can either be the internal coefficient between pellets (f_i), coefficient of friction between the polymer and the barrel (f_b) or the coefficient of friction between the polymer and the screw (f_s). The relationships between an arbitrary element and its adjacent elements are shown in Figure 2.12. The stress analysis is shown in Figure 2.13.

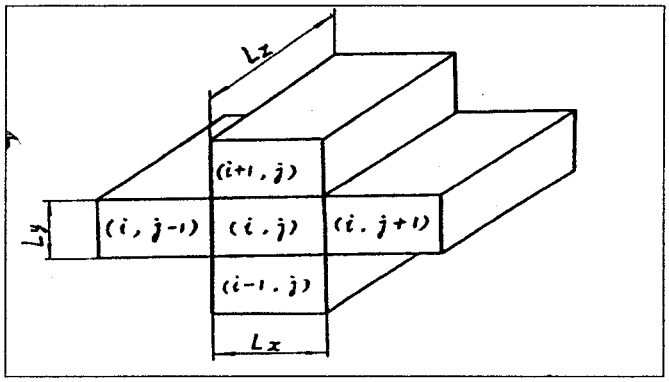

Figure 2.12: Relations between element (i, j) and its adjacent elements (Fang et al., 1991).

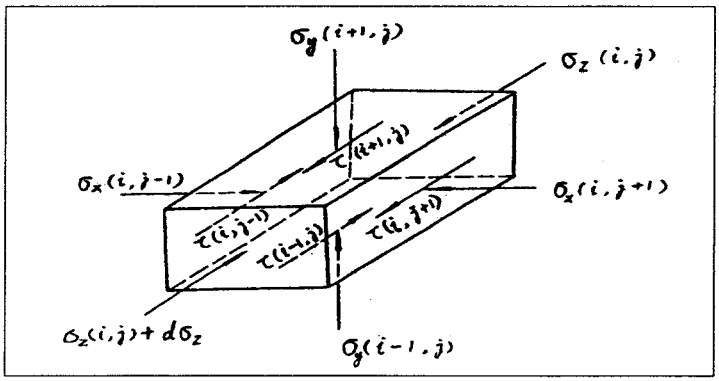

Figure 2.13: Stress balance on an arbitrary element (i,j) (Fang et al., 1991).

Combining finite element method to elastic mechanics theory, Fang, Chen and Zhu (1991) obtained the following equation:

$$\iint_A \left(X.u^* + Y.u^*\right)\delta z.dx.dy + \int_C \left(\overline{X}.u^* + \overline{Y}.u^*\right)\delta z.ds = \iint_A \left(\sigma_x \varepsilon_x^* + \sigma_y \varepsilon_y^* + \tau_{xy}\gamma_{xy}^*\right)\delta z.dx.dy$$

2- 65

Where:

- u^* and v^* are the virtual displacements at any point on channel cross section along x and y directions,
- $\varepsilon_x^*, \varepsilon_y^*$ and γ_{xy}^* are the virtual normal strains and shear strains,

- $\delta_z = L_z$ corresponds to the length of the element,
- A is the cross-section area,
- C is the boundary curve,
- ds is the differential of boundary curve C.

Eq. 2-65 is not suitable for the determination of the stress profile. It is necessary to introduce a relationship between the strain and the displacement:

$$\{\varepsilon\} = [B]^* \{\delta\} \qquad 2\text{-}66$$

With:

$$\{\varepsilon\} = \begin{Bmatrix} \varepsilon_x \\ \varepsilon_y \\ \gamma_{xy} \end{Bmatrix}$$

$$\{\delta\} = \begin{Bmatrix} u(x,y) \\ v(x,y) \end{Bmatrix}$$

$$[B] = \begin{bmatrix} \frac{\partial}{\partial x} & 0 \\ 0 & \frac{\partial}{\partial y} \\ \frac{\partial}{\partial y} & \frac{\partial}{\partial x} \end{bmatrix}$$

Where $\{\varepsilon\}$ is the strain matrix at an arbitrary point, $\{\delta\}$ is the displacement matrix at an arbitrary point, and $[B]$ is the geometric associated strain with displacement.

The constitutive equation of elastic mechanics is:

$$\{\sigma\} = [D]\{\varepsilon\} \qquad 2\text{-}67$$

With:

$$\{\sigma\} = \begin{Bmatrix} \sigma_x \\ \sigma_y \\ \tau_{xy} \end{Bmatrix}$$

$$[D] = \frac{E}{1-2\mu\xi(1+\mu)-\mu^2} * \begin{bmatrix} 1-\mu\xi & \mu(1+\xi) & 0 \\ \mu(1+\xi) & 1-\mu\xi & 0 \\ 0 & 0 & \dfrac{1-2\mu\xi(1+\mu)-\mu^2}{2(1+\mu)} \end{bmatrix}$$

Where $\{\sigma\}$ represents the stress matrix at any arbitrary point and $[D]$ is the elasticity matrix. E is the elastic modulus, μ is the Poisson ratio, and ξ is the lateral coefficient of granular material.

Using finite element method, the following equation can be derived:

$$\{P\}^e = [k]^e * \{\delta\}^e \qquad 2\text{-}68$$

Where $\{\delta\}^e$ is the nodal displacement, $\{P\}$ is the nodal force, and $\{k\}^e$ is the rigidity matrix of the arbitrary element e.

According to this analysis, Fang, Chen and Zhu (1991) established the relationships between the displacement vector and the nodal load vector of all node points in the system:

$$\{F\} = [K] * \{\delta\} \qquad 2\text{-}69$$

Where $\{F\}$ is the nodal load vector of all node points, $\{\delta\}$ is the nodal displacement and $[K]$ is the total rigidity matrix.

Using the boundary conditions for velocity field, displacement, and load, the velocity profile, authors were able to calculate velocity profile, flow rate, and pressure build-up. Table 2.2 shows that the results obtained using this model are in good agreement with experimental observations, compared to the results obtained using Darnell and Mol model (1956). However, the mathematic model of Fang, Chen and Zhu's model is difficult to combine with melt zone and pumping zone in numeric calculation and unable to predict the whole extrusion processing.

Table 2- 2 Comparison of flow rate and pressure between simulation and experiments (Fang, Chen and Zhu, 1991).

N (rpm)	Q_s (kg/h)			Pressure (kg/cm^2)		
	Experiment	Fang et al.	Darnell-Mol	Experiment	Fang et al.	Darnell-Mol
31	9.45	9.41	20.79	13.8	15.63	$2.13*10^5$
41	12.48	12.39	27.45	14.1	13.28	$1.92*10^5$
51	15.90	15.68	34.17	14.1	13.07	$1.83*10^5$

2.2 Measurement techniques

2.2.1 Friction coefficient measurements

Several types of coefficients of friction (COF) are commonly measured. They include dynamic, static, and storage COF. Each coefficient is used for different applications, and they must not be interchanged.

The static COF is the ratio of the maximum frictional force on a body and the load force perpendicular to the frictional surface at static equilibrium. If the frictional force is increased by a differential amount, then the body will start to move. If the body moves,

the ratio of the frictional force to the load force is called the dynamic COF. The dynamic COF is typically lower than the static COF. It is the type of coefficient of interest in the extrusion process. Storage describes how the pressure is transmitted or dissipated in a confined column of particles. It is a combination of friction between particles and friction between the particles and the chamber wall.

Leonardo da Vinci was the first to make some experimental observations for the COF about the year 1500. More recently Shooter and Friehe (1960) used an apparatus consisting of a melt plate mounted horizontally on bearings in an aluminum chamber. The polymer to be tested was inserted in the chamber. Using the required force to initiate a movement to the plate, they determined the static COF of polyethylene for a range of pressure comprised between 0 to 2.5MPa and temperatures from 22°C to 107°C. They showed that temperature, pressure, and surface roughness have an important effect on the static COF.

Schneider (1969) developed a special apparatus for measuring the COF between polymer particles and metallic surfaces. He observed that the state of the metal surface strongly affects the COF: the COF measured with a clean surface is lower than for a "dirty" surface. This phenomenon was attributed to the existence of a thin layer of polymer, deposited on the metal surface during the experiments.

Chung et al. (1977) and Kirkapatrick et al. (1993) used a "screw simulator" to determine the dynamic COF between polymer and metal surface under conditions similar to extrusion process. Their simulator, shown on Figure 2.14, consisted of a 30 cm diameter steel roll that could be heated to a temperature of up to 425°C and rotated at a maximum linear speed of 1 m/s. A sample of the polymer was then pressed against the roll by compressed air, creating a normal force of up to 5700 kg. Chung et al. (1977) tested 6

polymers: three amorphous glassy polymers (PS, PC, and PMMA) and three crystalline polymers (HDPE, LDPE, and PP). Their data indicated a very complex relationship between temperature, pressure, and speed as the polymers undergo distinct transitions of yielding and melting. They showed that the heat involved by friction could cause the polymers to melt at a temperature smaller than the thermodynamic melting temperature (T_p or T_g), when the pressure applied and the speeds of the roll were both high.

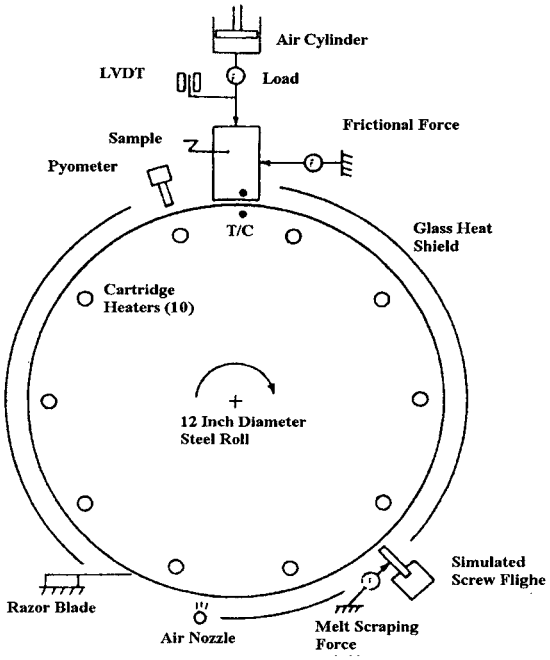

Figure 2.14: Schematic representation of the screw simulator (Chung et al., 1977).

Kirkpatrick et al. (1993) used the same equipment as Chung et al. (1977) to observe the modification of the frictional behavior as a function of the composition of a PVDC copolymer, either alone or blended with some polyolefins. They showed that both high and low density polyethylene are effective for lowering the dynamic COF and improving the extrusion performance of PVDC.

Spalding et al. (1995) used a similar instrument to determine the dynamic COF for several polyethylene (LDPE, ULDPE, LLDPE, and HDPE) and PVDC copolymers. Furthermore, they developed a numerical method to estimate the interface temperature between the polymer and the metal.

Gamache et al. (1999) investigated friction COF behaviors of HDPE, PP and PVC using a specific rotating device similar to an extruder (Figure 2.15). This instrument can be used to determine the shear stress caused by friction as a function of time, pressure, temperature, and speed. It consists of a 13.7 cm^2 annular cavity, containing the sample, with an annular disk placed on the top. The cover is made of steel and the part that is in contact with the polymer pellets is polished. It can be heated using an annular heater. The sample chamber is linked to a motor by a shaft. The speed of the sample chamber can be adjusted. A thermocouple is located 6 mm away from the interface of the metal and the polymer can monitor the evolution of temperature as a function of time. Gamache and al. observed that the rotation speed and particles shape had little influence on the friction coefficient. For HDPE and PVC, the friction coefficient decreased slightly with interfacial temperature, whereas it remained constant for PP.

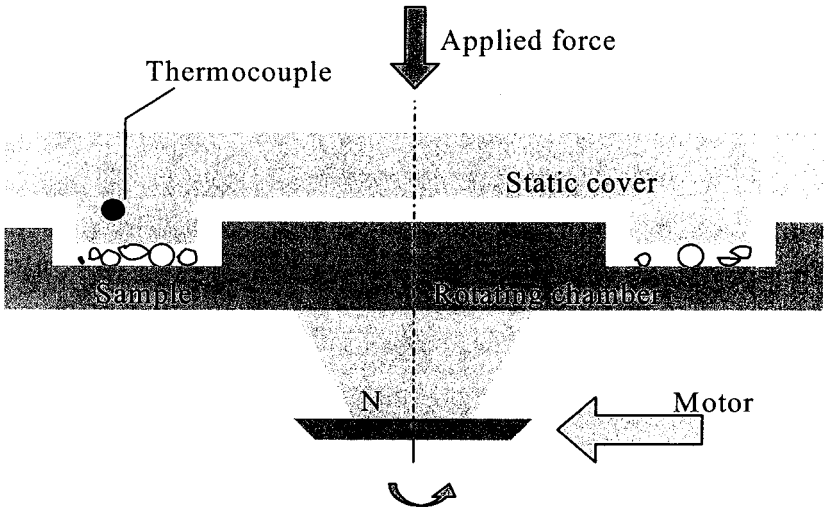

Figure 2.15: Experimental setup for COF measurement (Gamache and al., 1999).

The dynamic COF is often the controlling factor for solids conveying, pressure generation, and thermal decomposition of a resin in the feed section of a single-screw plasticating extruder. However, the COF is very poorly understood and very difficult to measure. Moreover, interpretations of experimental data are complicated by the dissipation of frictional energy at the sliding interface. This energy flux at the interface makes it extremely difficult to determine the COF as a function of temperature, pressure, and velocity at extrusion conditions.

For all COF measuring devices, the thermocouple used is located away from the interface where the friction is occurs. At the sliding interface, friction dissipation of energy will result in a higher temperature than the measured temperature. This effect can be quite large at typical extrusion conditions. Since the thermal conductivity of the metal surface is about 500 times greater than that of polymers, most of the generated heat will be conducted into the metal. Moreover, since the metal surface is moving, the temperature distribution will be a function of the normal distance to the metal surface and of the movement of the polymer slider. So, frictional heat generation at the interface depends on the pressure, friction coefficient, and tangential velocity.

2.2.2 Solid bulk density measurements

The bulk density of a polymer at ambient conditions depends on the particles size and shape, and on the solid density of the material. As pressure is applied to the polymer, the particles deform and the void volume between the particles decreases, resulting in an increase in the bulk density. Under high-pressure conditions, the void volume will be very small and the bulk density will approach the solid density. Bulk density also strongly depends on the temperature. As the temperature of the solid is increased, the modulus will decrease and the particles will deform more easily at a given pressure,

resulting in an increase in the bulk density. Particle fracture is not expected to occur in the typical pressure range of extrusion.

In a plasticating extruder, solid polymers are heated and are subjected to high pressures before they are melted and delivered to the die. In both solids conveying and melting sections, temperature and pressure increases will compact the solid polymer bed as it moves down the screw channel. The current and widely accepted understanding of the solid conveying mechanism for the feed section is based on the Darnell-Mol model theory, which assumes constant density for the solid bed. Furthermore, the constant bulk density assumption for the feed section is valid only for some of the high glass transition temperature (T_g) polymers. However, for the extrusion of semi-crystalline polymers with low T_g, like polyethylene, poly(ethylene-acrylic acid) copolymer (EAA), and poly(vinylidene chloride) copolymer (PVDC), the bulk density changes greatly in the screw channel before the resins start to melt. Since the temperatures are above T_g, these resins compact easily.

Hyun et al. (1990) studied the bulk density for many semi-crystalline polymers. Spalding et al. (1997) developed a device shown in Figure 2.16 to study the compacted phenomenon for the solids conveying zone. This device consists of a cylinder with a 2.540 cm diameter and a piston with a slip fit. A load cell (top load cell), positioned between the piston and the loading mechanism, is used to measure the applied force. Polymer samples are placed between the piston and a bottom plug inserted into the cylinder. The force, transmitted from the piston through the sample, is measured by another load cell (bottom load cell). The piston position and sample volume are measured using a linear variable differential transducer (LVDT). The device is heated with two band heaters.

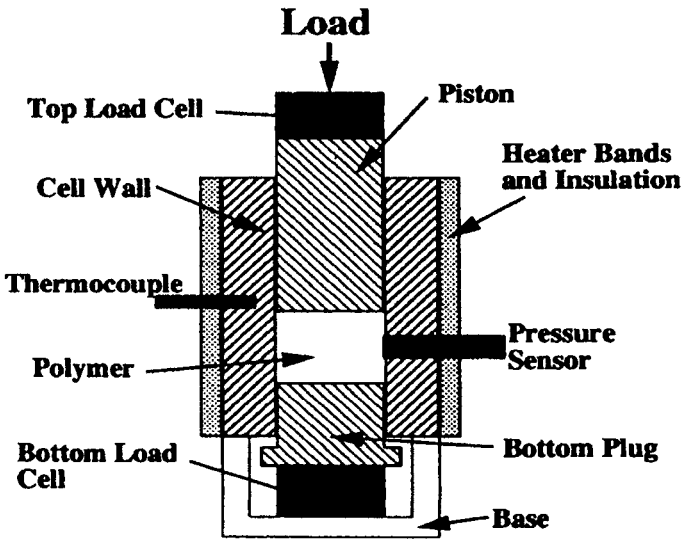

Figure 2.16: Compaction testing cell (Hyun and Spalding, 1990).

The force applied to the top of the solid bed is transmitted through the bed to the bottom plug. The bottom load cell detects the resulting force on the plug. The bulk density is calculated as follows:

$$\rho = \frac{4W}{\pi D^2 H} \qquad 2\text{-}70$$

Where W is the weight of the sample, H is the height of the cylinder volume measured by the LVDT and D is the diameter of the cylinder.

The pressure drop occurs because of the friction at the wall and the friction between the particles. The average pressure is an algebraic mean of the top (P_t) and bottom pressures (P_b):

$$P_{av} = P = \frac{(P_t + P_b)}{2} \qquad 2\text{-}71$$

Hyun and Spalding (1990) observed that the bulk density of the polymer is a function of temperature and pressure. Powders show higher levels of compaction than pellets. Amorphous polymers compact very little with pressure for temperatures between ambient and about 20 C below T_g. Compaction occurs readily at temperatures just below T_g. Semi-crystalline polymers compact readily at all temperatures between ambient and the melting temperature. Bulk density data were in good agreement with a semi-empirical model proposed by the authors. This model can be used in solids conveying and melting zone extrusion simulators.

2.2.3 Lateral stress ratio measurements

Almost all the existing models suppose that the pressure in the plane perpendicular to the flight is isotropic. Forces at both the screw and barrel surfaces are assumed to be directly proportional to this pressure at a given axial distance. The force is defined as the pressure multiplied by the differential contact area. This assumption is not only used to simplify the mathematics, but also because of the lack of stress distribution data for solid compacts beds.

Schneider (1969) showed that the stresses in solid compacts are not isotropic. He proposed a method to account for the non-isotropic pressure distribution existing in the solid bed. Based on this method, Broyer and Tadmor (1972) assumed a certain ratio of normal stresses giving: $P_b=K_b*P$, $P_f=K_f*P$, and $P_s=K_s*P$.

Umeya and Hara (1978) studied the compaction for polystyrene powder. The compaction was found to be a function of temperature, compaction speed and void fraction of the powder bed. The stress reduction behavior of an axial stress σ_1 and a radial stress σ_2 was observed at constant void fraction after compaction. Crawford and

Paul (1981) performed a similar work, measuring the lateral stress for selected polymers. However, generally speaking the ratio is unavailable. They also indicated that the stress distribution in the compacted solids was a function of the vertical height and of the radial position for cylindrical test cells. However the two-dimensional analysis of this cell was not practical. Measurement of the lateral stress ratios can be done at a predetermined stress plane perpendicular to the vertical axis. The measurement becomes simpler when the vertical height of the compact becomes small, thus minimizing vertical stress gradients.

Recently, Spalding et al (1997) proposed that anisotropic stresses in the solid bed would affect the solids conveying forces at the metal surfaces of the extruder, and hence affect the accuracy of the models assuming an isotropic stress distribution. A new compaction cell was developed to measure the bulk density, storage COF, static COF at the wall and lateral stress ratio (Figure 2.16). The force balance over a differential bed height for this cell is similar to that for a cell having a circular cross section. Solving the balance equation gives:

$$P_t = P_b \exp\left[\frac{K\mu_s CH}{A}\right] \qquad 2\text{-}72$$

Where P_t is the top pressure, P_b is the bottom pressure, K is the lateral stress ratio, μ_s is the static COF at the cell wall, C is the circumference of the cell, and H is the height of the compact.

The lateral stress ratio is the ratio of the compressive stress in the horizontal direction to the compressive stress in the axial direction:

$$K = \frac{P_s}{P_{ax}} \qquad 2\text{-}73$$

Where P_s is the pressure measured at the side of the cell by the transducer and P_{ax} is the pressure in the axial direction at the height of the pressure transducer.

The static COF at the wall is computed as follows:

$$\mu_s = \left[\frac{A}{KCH}\right] \ln(P_t / P_b) \qquad 2\text{-}74$$

The storage COF is computed as follows:

$$f = \left[\frac{4A}{CH}\right] \ln(P_t / P_b) \qquad 2\text{-}75$$

The experimental results indicated that the stresses in the compacted bed were anisotropic, and lateral stress ratios were measured in the range of 0.3 to 0.9. Thus, the stresses in the secondary direction were about 30 to 90% that of the stresses in the primary direction. The ratio depends on the temperature but is independent of pressure in the tested range.

CHAPTER 3: FRICTION COEFFICIENT MEASUREMENT

3.1 Experimental method

3.1.1 Materials

For the determination of COF, we used a PVC resin whose physical properties are shown in Table 3.1. The PVC resin was supplied in a powder form and was extruded in a single-screw extruder before being granulated. The solid granules were then molded to obtain thin cylindrical samples with diameters and lengths of about 11 mm and 20-30 mm respectively.

Table 3-1 Physical properties of the PVC.

Material	Heat Capacity (Cp) J/kg	Density kg/m^3	Emissivity	Heat conductivity (k) W/mK
PVC	850	1400	0.6	=0.3173-0.0252*ln (T)
Steel	477	7900	0.07-0.17	=(T+273)/50+12.6

3.1.2 Equipment

To analyze the frictional behavior of polymers on a metal or plastic surface, a special apparatus was designed and built at École Polytechnique de Montréal (Figure 3.1). This device is a second-generation instrument based on the screw simulator developed by Chung et al. (1977). This equipment was designed to control independently three primary variables: temperature, pressure and speed. It was used to determine the shear stress caused by friction as a function of these parameters.

The device uses the concept of a stationary screw within a rotating barrel. An annular disk (inner diameter: 300 mm; outer diameter: 450 mm) rotated by a motor was used to model the rotating barrel. This disk was covered by an insulated layer to prevent heat losses. A plate was located on the annular disk. This plate could be heated with a heat band from room temperature up to 70°C or more, depending on the thermal conductivity and emissivity of the plate. The speed of the plate could be adjusted by the motor. The polymer sample was held in a cylindrical sample cavity (diameter=11 mm) and pressed against the plate by a 4.54 cm diameter air cylinder. Using a air pressure of 0.62, a normal force up to 460 kg could be applied to the polymer sample. While the plate was rotating at a fixed speed, the torque caused by the friction tended to move the sample holder in the tangential direction. A force sensor connected to the sample allowed the measurement of the friction force.

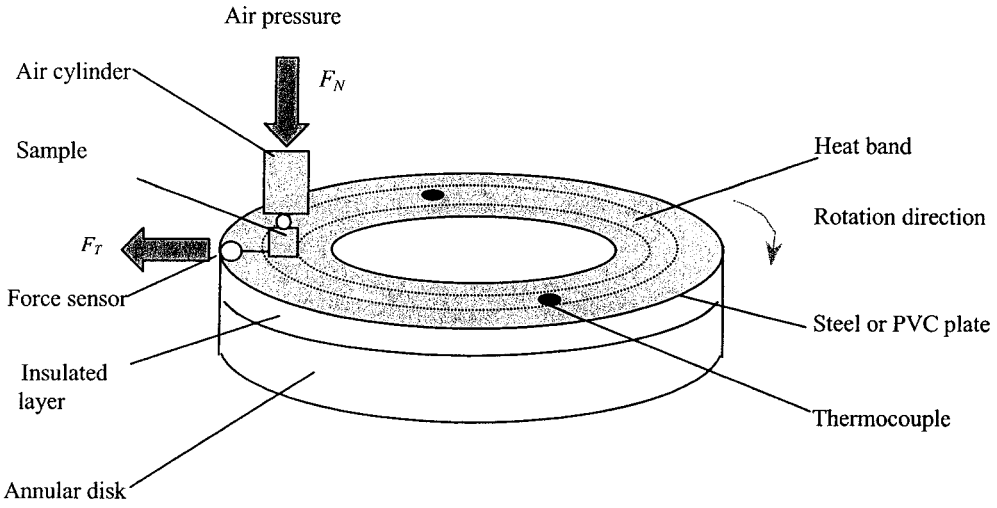

Figure 3.1: Schematic representation of friction measurement device.

The dynamic COF was defined as the ratio of the tangential friction force F_T (obtained from the force measurement) to the normal force F_N:

$$COF = \frac{F_T}{F_N} \qquad 3\text{-}1$$

The values of f_b (COF between screw and polymer), f_s (COF between barrel and polymer) and f_i (internal COF) were determined using respectively polished steel plate, a rough steel plate and polymer plate.

Therefore, the apparatus shows some similarity with a single screw extruder. As a matter of fact, the shape of the annular channel is similar to the helical channel of an extrusion screw. The polished steel plate and rough steel plate represent respectively the screw surface and barrel surface. The rotation of the plate corresponds to the rotation of the screw and the barrel.

Since there is no practical method to measure the interface temperature underneath the polymer sample, the temperature was measured by means of two thermocouples located 1.5 mm away from the sample/plate interface. We will see later how it is possible to estimate the interface temperature.

All instrument sensors were controlled and monitored using a computer. For a sample having an area A, the pressure was calculated with the following equation:

$$P = \frac{F_N}{A} \qquad 3\text{-}2$$

The speed of the steel plate was measured and controlled using a frequency signal linked to the motor, which provided mechanical power to the plate.

In order to increase the accuracy, before each experiment, the position of the sample holder was adjusted to make sure that the air pressure was applied at the center of the polymer sample.

3.1.3 Procedure

Previous investigations have shown that the metal surface condition, whether it is clean or rubbed-in by the polymer, can have a strong influence on the friction between the polymer and the metal (Chung et al., 1977). It is noted that the dynamic friction of a polymer on a rubbed-in metal surface represents the actual condition in extruder. In our experiments, the steel plate was not purposely rubbed-in. Therefore, for each set of operating conditions, we used the following procedure:

- The steel plate surface was first cleaned to a shiny finish.
- The polymer specimen was inserted in the sample holder and numerous trials were performed. During these experiments, the dynamic COF measured value decreased slightly.
- Trials were continued until dynamic COF had reached a constant value for the tested set of operating conditions.

These experiments were used to condition the steel plate surface only. Thus the friction data were discarded. Once this procedure was done, the sample was removed and replaced with a new one. This procedure was repeated for each data point reported.

The procedure for the experiment start-up was the following:

- Once the interfacial temperature had reached the desired level (checked by means of the thermocouples) and the temperature of the polymer was uniform, the air cylinder was lowered onto the sample and a low pressure (0.07MPa) was applied

- The plate was rotated at the set speed.
- The pressure was increased smoothly to the set value.
- After a stabilization period ranging from 5 minutes to 15 minutes, the pressure, frictional force, and temperature were considered to have reached their steady state values. The frictional force was then recorded.

After an experiment was completed, the frictional force was plotted as a function of time. The dynamic COF was deduced from the slope of the plots calculated using Eq. 3-1.

3.2 Interface temperature calculation

3.2.1 Numerical calculations

As we explained previously, the plate temperature underneath the polymer sample is not easy to measure. However, because of the strong rise of temperature occurring during the experiments and the associated variation of COF value, it seemed important to determine the exact interface temperature. This temperature can be calculated using the energy equation and the boundary conditions provided by the experimental values measured with the thermocouples. Therefore, for the geometry described in Figure 3.2, we solved the heat transfer equations using an implicit finite difference technique.

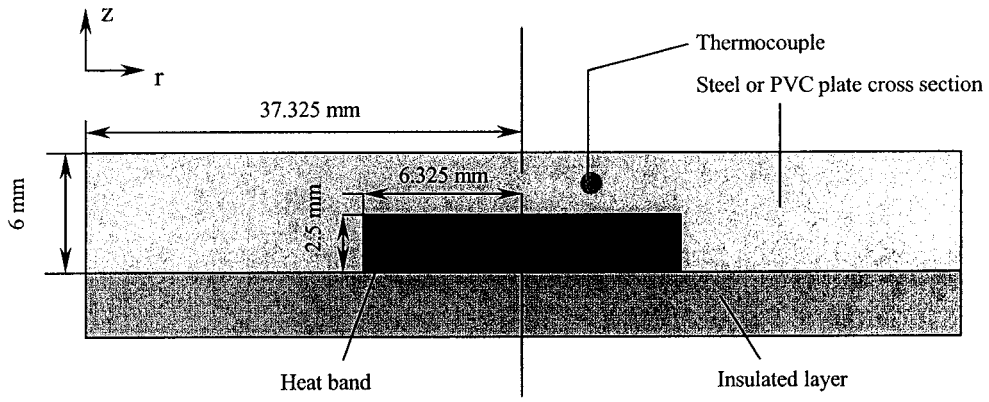

Figure 3.2 Geometry used for the thermal computation.

The calculation assumptions were the following:

- The conduction is two-dimensional.
- All the sides exposed to air are subjected to natural convection.
- Heat generation is exclusively located at the polymer-metal or polymer-polymer interface.
- The contact resistance was neglected.

Using cylindrical coordinates, and considering that the temperature does not vary with angle θ, the can be written as following:

$$\frac{1}{r}\frac{\partial}{\partial r}(kr\frac{\partial T}{\partial r})+\frac{\partial}{\partial z}(k\frac{\partial T}{\partial z})+q_{gen}=\rho C_p\frac{\partial T}{\partial t} \qquad 3\text{-}3$$

Where T is the temperature at plate radius position r, and vertical position z at time t. C_p, ρ, and k are the heat capacity, density, and thermal conductivity of the plate. The heat generation term q_{gen} is a function of pressure (P), rotational speed (N in turn/sec), diameter of the annular ring (D), area of contact (A) and the dynamic friction coefficient. It can be written as following:

$$q_{gen} = \mu PND\pi A \qquad 3\text{-}4$$

The values used in the calculations are listed in Table 3-1.

A constant ambient temperature of 25 °C was used as a boundary condition.

To solve the heat transfer equation, a finite difference technique using a nodal mesh of 1mm by 1mm was adopted. Because of the symmetrical geometry and in order to reduce the calculation time, only one half of the calculation zone was simulated (Fig.3.2). This gave us more than 200 points to calculate for iteration. An implicit method of resolution was chosen to solve these equations. In comparison with the explicit method, the implicit method has the important advantage of being unconditionally stable. That is, the solution remains stable for all space and time intervals, which gave us the opportunity to use larger time steps Δt.

The calculation algorithm is shown at Fig.3.3. First, we should compute the steady-state temperature profile for the calculation zone without heat generation at set heat band temperature; second we need to compute the temperature for the calculation zone with heat generation with an assumed dynamic friction coefficient μ_d. The interface temperature for the sample is the average temperature of the five nodes underneath the sample chamber. If the difference between experimental value of μ_d and assumed value is out of a set tolerance, we should change the assumed friction coefficient, and compute the temperature profile again until assumed μ_d is within a specifically tolerance from the experimental value. Interface temperature was computed for all measurements as we changed pressure value or rotation velocity. In order to keep the interface temperature constant for different pressure and rotation velocity during the experiment procedure, the temperature of the heat band was adjusted. It was found that the rotation velocity of steel (or PVC) plate does not affect the interface temperature greatly.

Since the plate was moving at relatively low rotation velocity, the steel surface had time to cool to the temperature measured by the thermocouple before re-entering the sample impingement area. For those cases when the steel plate rotation velocity is high, or for the PVC plate (because of the poor thermal conductivity of PVC,) the plate surface temperature was always higher than the thermocouple read value.

In the implicit finite-difference method, the temperature of any node at t+ t may be calculated from knowledge of temperatures at the neighboring nodes for the same time and the same node for the previous time t. It allows an unlimited time increment t in the calculation. The nodal temperature at each time are computed, t = t, 2 t... until the desired final time was reached. To maximize accuracy, t should be sufficiently small to ensure that the results are independent of further reductions in its value. In our case, the selection of t depends on the thermal conductivity of steel and PVC. For good heat conductor, t need to be small enough to ensure the deviation between $T_{t+\ t}$ and T_t for one node is small; for poor heat conductor PVC, t can be relative large. For example, at rotation speed 5 rpm, t is 0.06s for steel, and it is 1.2 s for PVC in simulations.

3.2.2 Algorithm

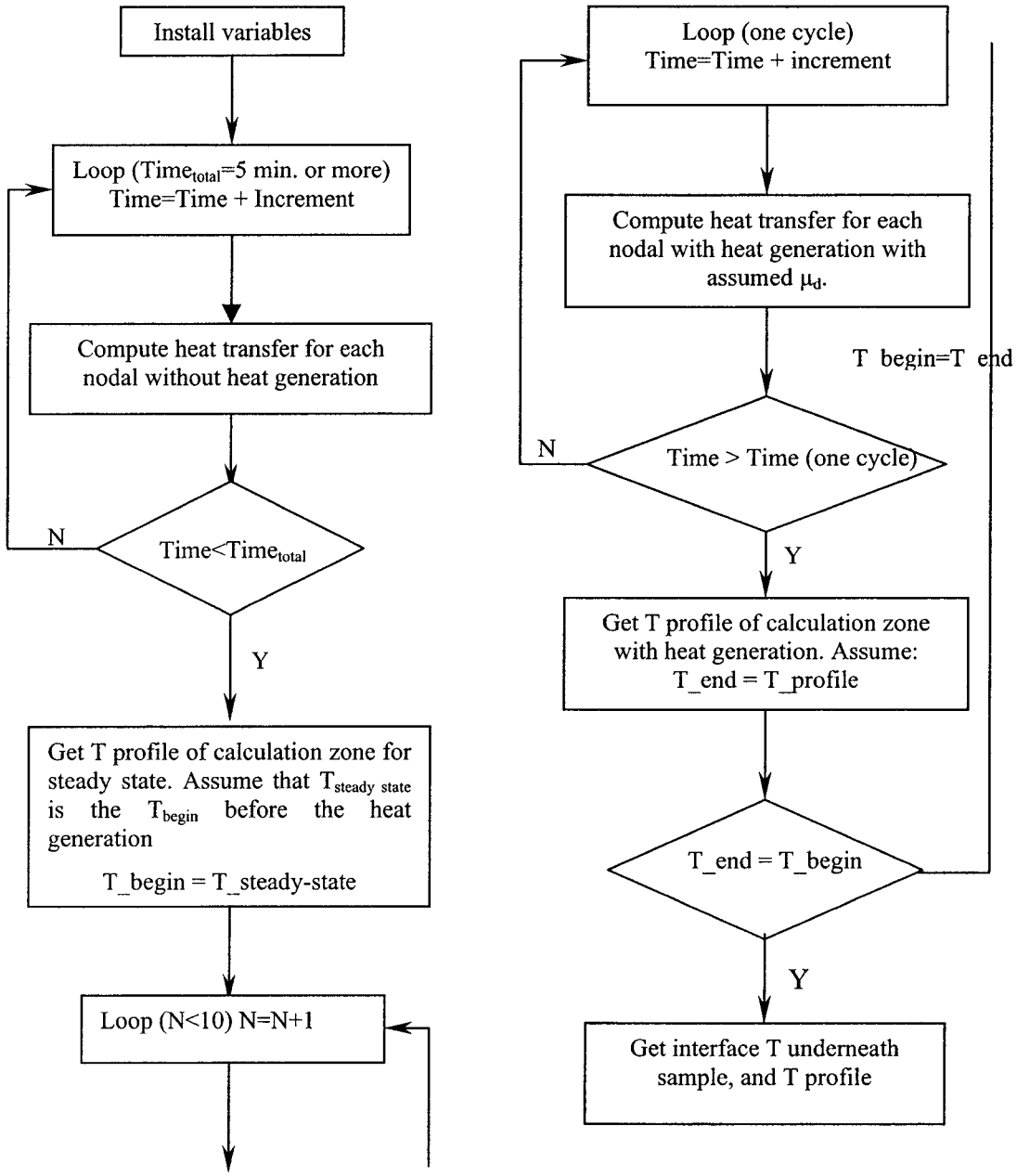

Figure 3.3: Calculation algorithm for interface temperature.

3.2.3 Simulation results for the surface temperatures

Fig.3.4 to Fig.3.6 show simulation results of the polished steel, rough steel and PVC plate temperature distribution for the cross section of the calculation zone underneath the sample. As indicated by this figures, the highest temperatures located at the surface of the plates just underneath the sample. The estimated interface temperature as a function of time (one cycle) for three plates are shown in Fig.3.7 to Fig.3.9. The peak point of the interface temperatures was exactly the same point as the highest temperature in calculation zone temperature profile.

Comparing peak point temperature at same operation condition for polished and rough steel plates, the polished steel is little lower than rough steel. That is due to the lower COF of polished steel. Since PVC plate has poor heat conduction, the operation conditions have to change. (Explain in chapter 3.1.1) It is clear that PVC plate has the highest temperature even though heat band temperature and applied pressure is lower than that for steel plate. That is because the large COF and poor heat conduction ability.

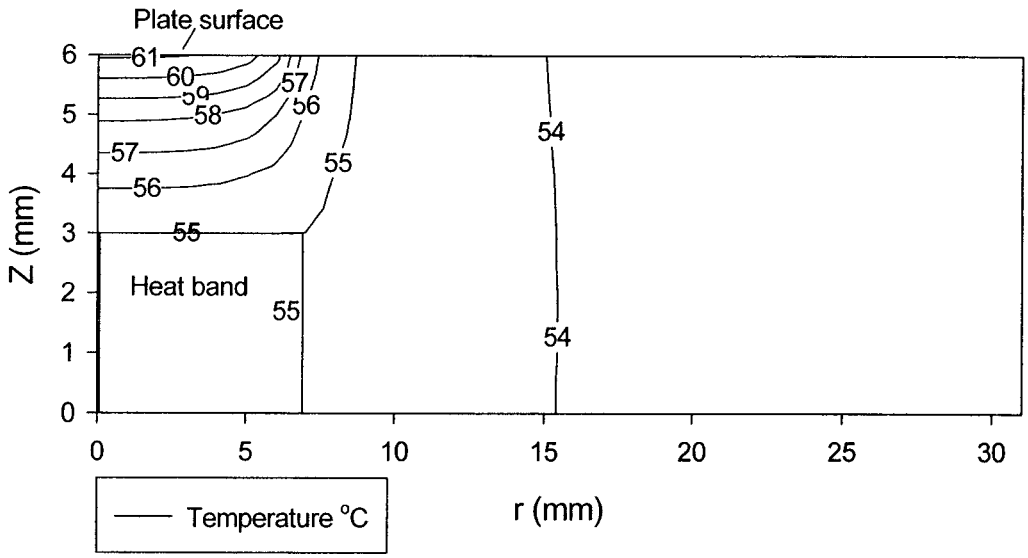

Figure 3.4: Polished steel plate calculation zone temperature profile underneath the sample, T_heat=55°C the interface temperature underneath the sample is: T_average = 61°C.

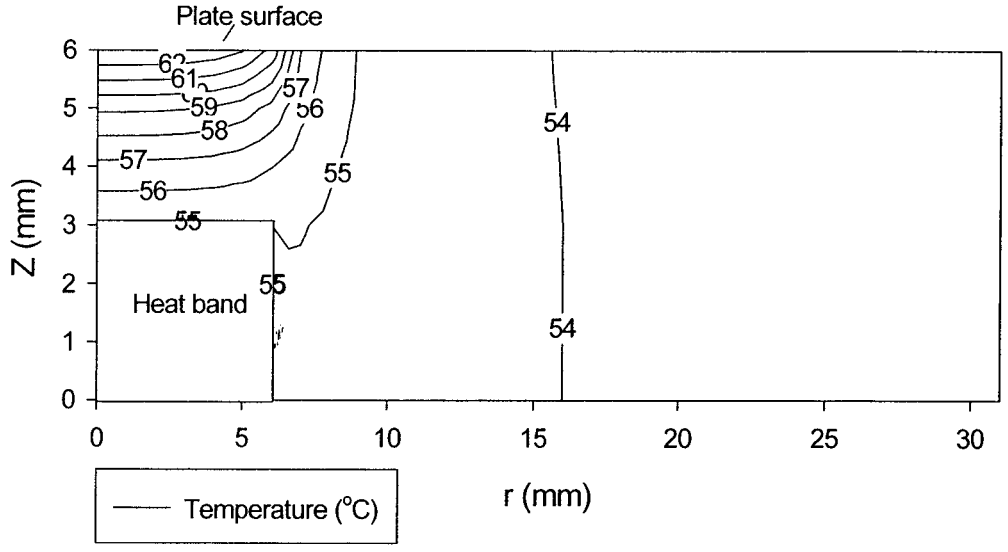

Figure 3.5: Rough steel plate calculation zone temperature profile underneath the sample, T_heat=55°C the interface temperature underneath the sample is: T_average = 63°C.

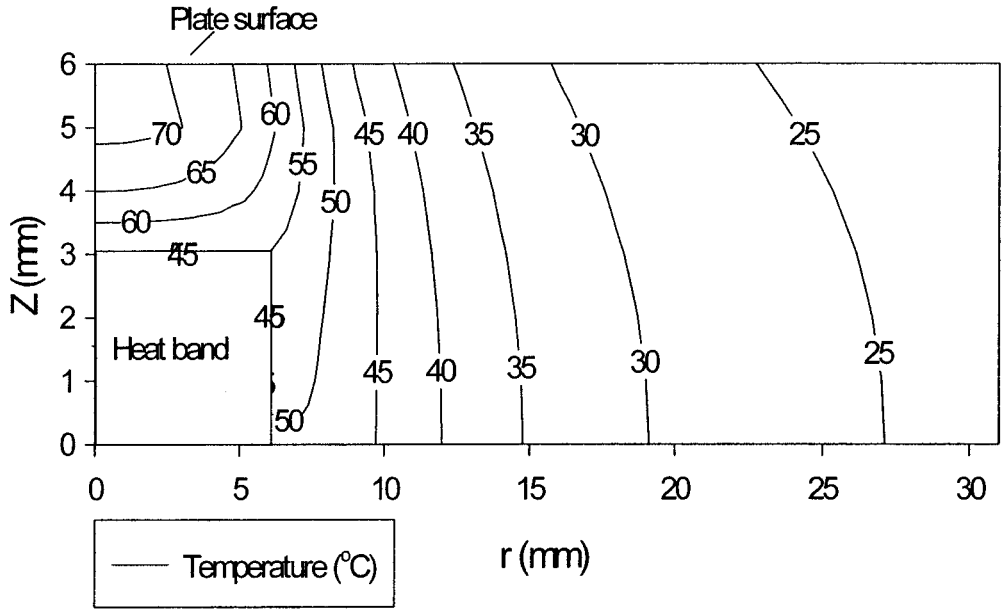

Figure 3.6: PVC plate calculation zone temperature profile underneath the sample, T_heat=45°C the interface temperature underneath the sample is: T_average = 70°C.

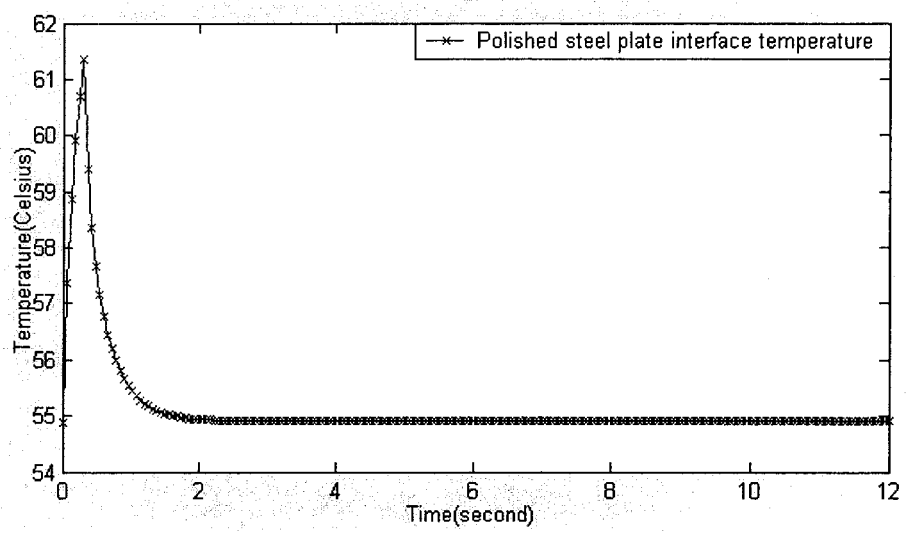

Figure 3.7: Polished steel plate interface temperature as a function of time (one cycle), k=43, E_m=0.17, μ=0.37, T_{heat}=55°C, N=5rpm, P=4.03 MPa, Δt=0.06s, one cycle time=12s.

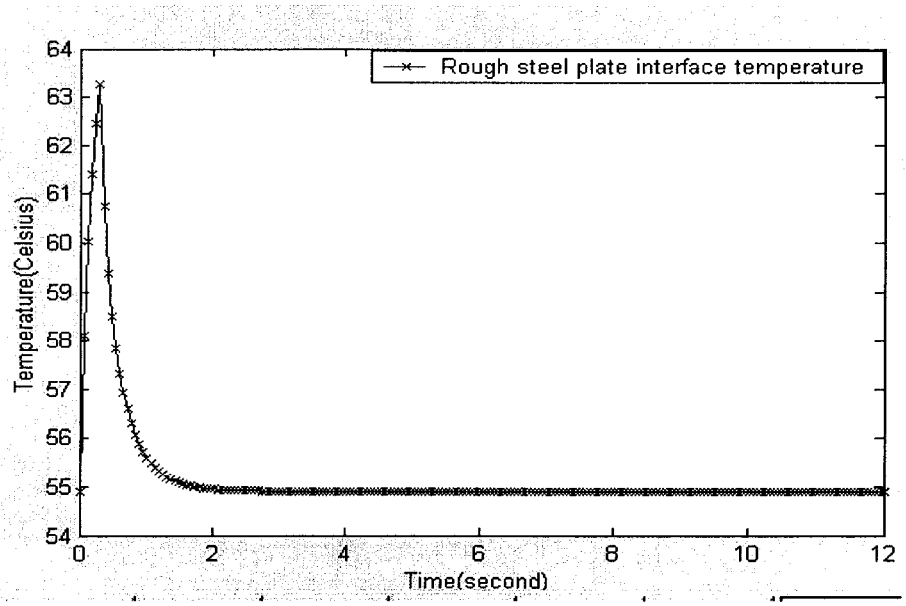

Figure 3.8: Rough steel plate interface temperature as a function of time (one cycle), k=43, E_m=0.07, μ=0.48, T_{heat}=55°C, N=5rpm, P=4.03 MPa, Δt=0.06s, one cycle time=12s.

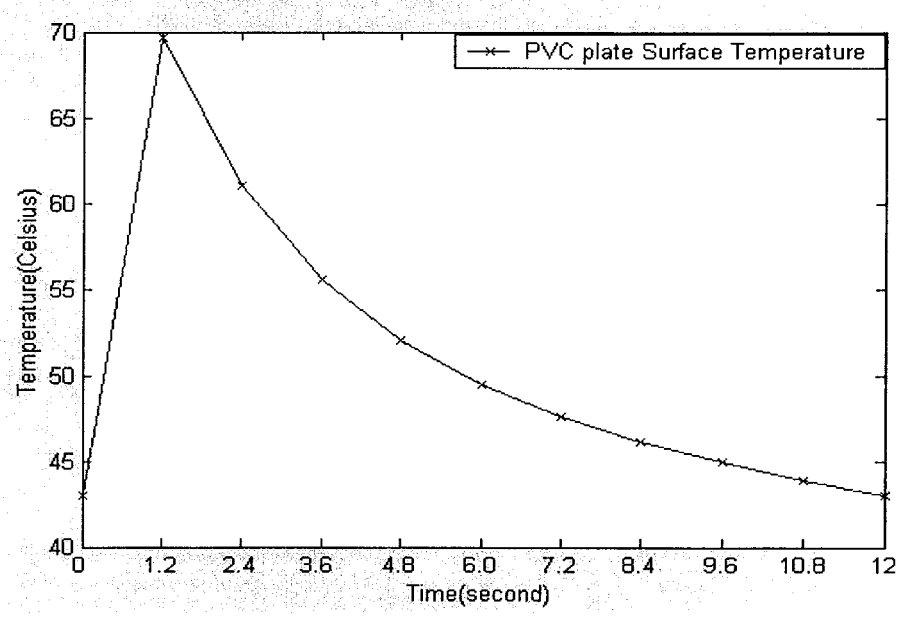

Figure 3.9: PVC plate interface temperature as a function of time (one cycle), k=0.02, E_m=0.6, μ=0.54, T_{heat}=45°C, N=5rpm, P=1.95 MPa Δt=1.2s, one cycle time=12s.

3.3 Experimental results and discussion

3.3.1 Experimental plan

Measurements of COF were started a little above the ambient temperature, and consecutive measurements were made with increasing temperatures for given velocity and pressure. To observe the individual variable effect on the COF, we need to make sure the two other variables remain unchanged as one variable changes. The main difficult point consists in keeping the interface temperature constant since the interface temperature cannot be measured directly. However, it is possible to change the interface temperature by controlling the temperature of the heater band. This implies different steps:

Step 1: Once the steel plate interface temperature has reached a steady state at a pre-set temperature of the heater band, the speed rotation was started. The steel plate immediately achieved the pre-set speed. Then, the normal force was applied on the sample holder. At the same time, the steel interface temperature at this operation condition was obtained using simulations, after steady state, the outputs from the force sensor were recorded. COF at particular pressure, temperature, and speed was computed.

Step 2: The interface temperature has to be kept constant for the next experiment. Pressure and/or speed were changed according to an experimental plan. This time, we had to do the simulation again, to decrease (or increase) the temperature of the heater band, to ensure the computed interface temperature was the same as in step 1.

For example, the steel interface temperature was found to be 41°C, when the temperature of heat band was 35°C, the pressure was 4.03 MPa, and the steel plate speed 5 rpm. If the pressure was to be increased to 8.8 MPa, (the steel plate speed remaining unchanged), the temperature of the heat band has to be decreased to 32°C to keep the interface temperature constant. This procedure was repeated for each data point. The

calculation of interface temperature allows the pressure, speed and temperature effects to be decoupled.

During the experiments, a very interesting phenomenon was observed. Although the polished steel plate was highly polished, the PVC samples were actually ground off by the steel plate as if the samples had been pressed against a grinding wheel, producing small white fragments of the polymer at high pressure, high rotation speed, and causing a wear of the sample. This effect was even more pronounced with rough steel plate and PVC plate because of the high COF. The samples were ground off at all experimental conditions and caused a rapid wear of the sample. The grooved surfaces of these samples after testing clearly indicate the grinding phenomenon. For rough steel and PVC plate, PVC sample was worn off even before steady state was reached at some operation conditions. For these cases, we had to record the closest data to steady state therefore measuring.

In our experiments, we chose the rotational speed, the interfacial temperature, and the pressure as the three factors affecting the friction coefficient. From a statistic experiment design view, we used three levels, and full factorial experiment design. We had 27 runs for each plate. The general experimental plan for polished steel plate is shown in appendix II. After analyzing the experiments results (figure 3-10), we found that the rotation speed is not a significant factor. In order to save experimental time, we neglected this factor for the rough steel plate and PVC plate experimental designs. Then, it became a full factorial experimental design with two factors, and three levels. There are only 9 runs for each plate. Because of the poor heat conductivity of PVC, the surface temperature was increased to extremely high level under the same experimental conditions as that of steel plates, this temperature may be close to the melt temperature of PVC. Therefore, we had to use a diffferent experiment plan for PVC plate. In comparison with the steel plate, we chose a lower pressure and heat temperature in our

experiments for PVC. Since the heat power was not strong enough, the highest temperature of heater band for rough steel plate was 70°C, about 10°C lower than that for polished steel plate. This result is due to the difference in emissivity between rough and polished steel plate. The experimental plan for rough steel plate and PVC plate are shown in appendix II.

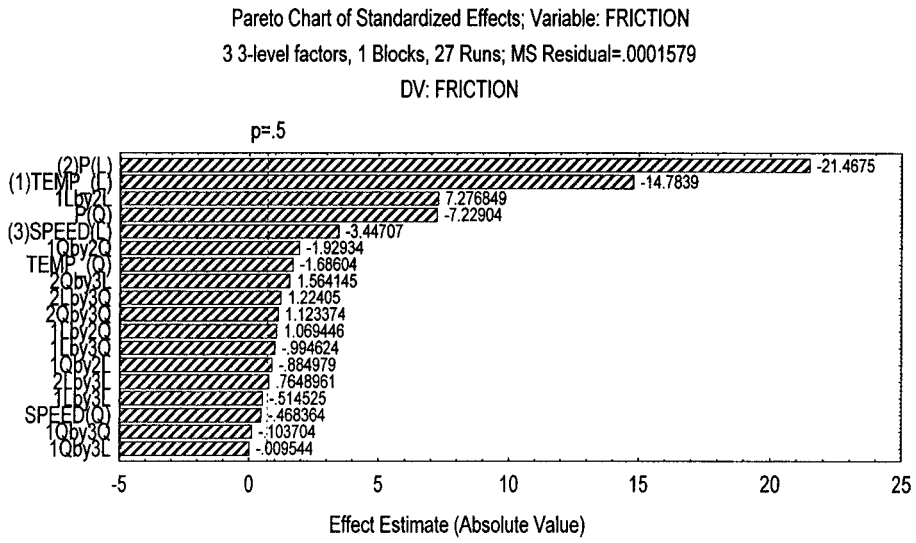

Figure 3.10: Statistic Experimental Result Analysis.

3.3.1 Speed effect for polished steel plate

COF of PVC resin on polished steel plate was measured as a function of speed at temperature range of: 40°C~80°C, at pressure of 4.03 MPa, 8.8MPa, and 13.47MPa. The COF experimental data are shown at Fig.3.11.

Fig.3.11 shows the COF as a function of speed, and pressure for temperatures of 41°C, 60°C, and 81°C. The COF was about 0.55 at 41°C under a pressure of 4.03 MPa. At that

temperature the COF is not sensitive to variation of rotation velocities. At a pressure of 8.8 MPa, the trend of the coefficient with velocity was similar to that at 4.03 MPa with a lower absolute value. At 13.47 MPa, the coefficients decreased with the increasing velocity. At 60°C, and 81°C, the trend was the same for pressure at 8.8 and 13.47 MPa as shown in Fig. 3.11 B and C. At 4.03 MPa, coefficients decreased with increasing velocity. These figures show that the coefficient does not seem to depend significantly on the velocity. The statistical analyses of the experimental data lead to the same result. From the Pareto Chart graph, we knew that pressure and temperature are the most significant factors affecting the COF. Therefore, in order to save experimental time, we eliminated the less significant factor in the rest of the experiments (i.e. for rough steel and PVC), which is rotational speed in this case. The design of experiments became a full factorial design with two factors and three levels.

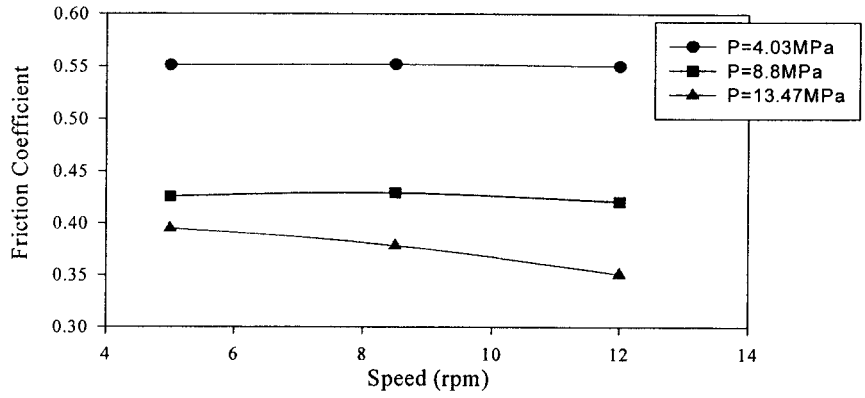

(A) Interface Temperature = 41°C, μ_d as a function of plate velocity at P=4.03 MPa, 8.8 MPa, and 13.47 MPa.

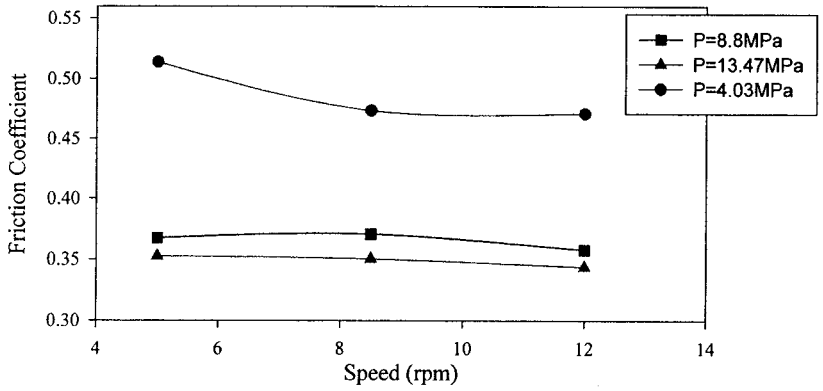

(B) Interface Temperature=60°C, μ_d as a function of plate velocity at P=4.03 MPa, 8.8 MPa, and 13.47 MPa.

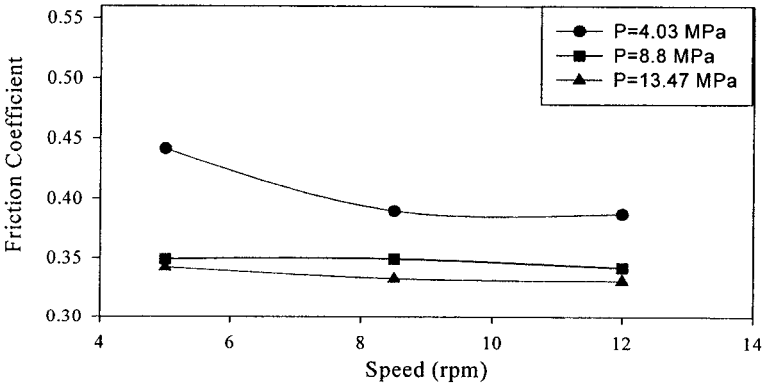

(C) Interface Temperature = 81°C, μ_d as a function of plate velocity at P=4.03 MPa, 8.8 MPa, and 13.47 MPa.

Figure 3.11: COF as a function of screw speed for polished steel plate.

3.3.2 Temperature effect for polished and rough steel plates

Figure 3.12 shows the dependence of frictional behavior for PVC with temperature at constant plate speed of 8.5 rpm. For polished steel plate, at a pressure of 4.03 MPa, the COF value was ~ 0.52 at 41°C. It decreased almost linearly with increasing temperature. However, at pressures of 8.8 MPa, it decreased slightly with increasing temperatures and seemed to keep constant at temperatures above 90°C. At 13.47 MPa, it decreased slightly at range 41°C ~ 80°C, after 80°C, COF decreased rapidly and reached the lowest value of 0.27.

To estimate the friction coefficient between barrel surface and PVC during extrusion processing, we replaced the polished steel plate by a rough steel one, whose roughness is the same as the barrel surface. As figure 3.12 indicates, at pressure 4.03 MPa, COF for rough steel kept constant from interface temperature 41°C to 60°C but dropped rapidly at 70°C. We noticed that at 70°C COF for rough steel plate was lower than that of polished steel plate. That might cause serious solids conveying problems. At 8.8 MPa and 13.47 MPa, the COF curves were similar as that at 4.03 MPa. We know that the bigger the difference between the COF of barrel and screw, the higher the output. All the COF curves for rough steel showed that the roughness was not high enough for an efficient extrusion, especially at relative high interface temperatures.

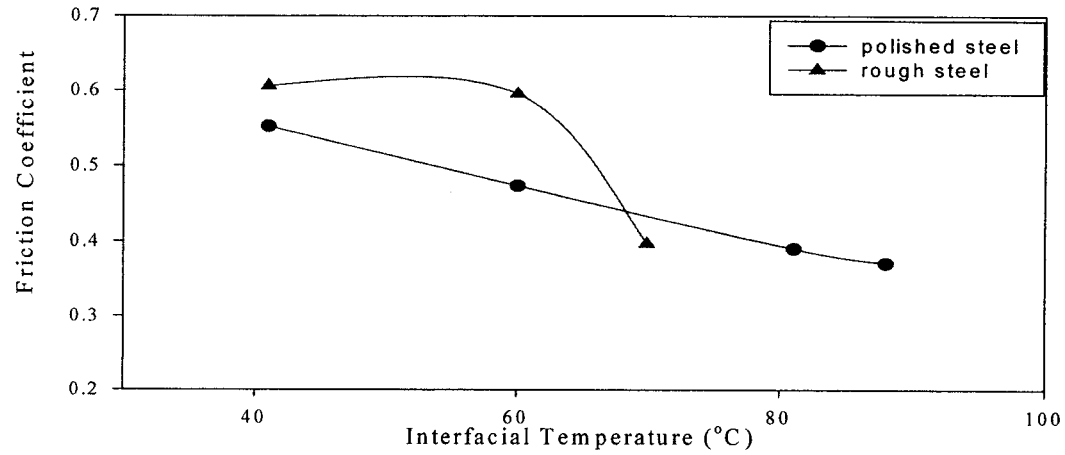

(A) P=4.03 MPa

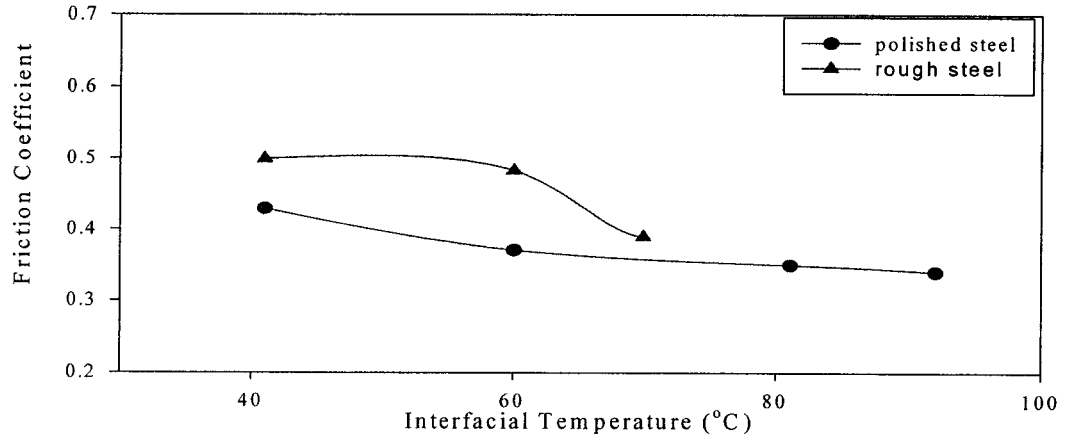

(B) P=8.8 MPa

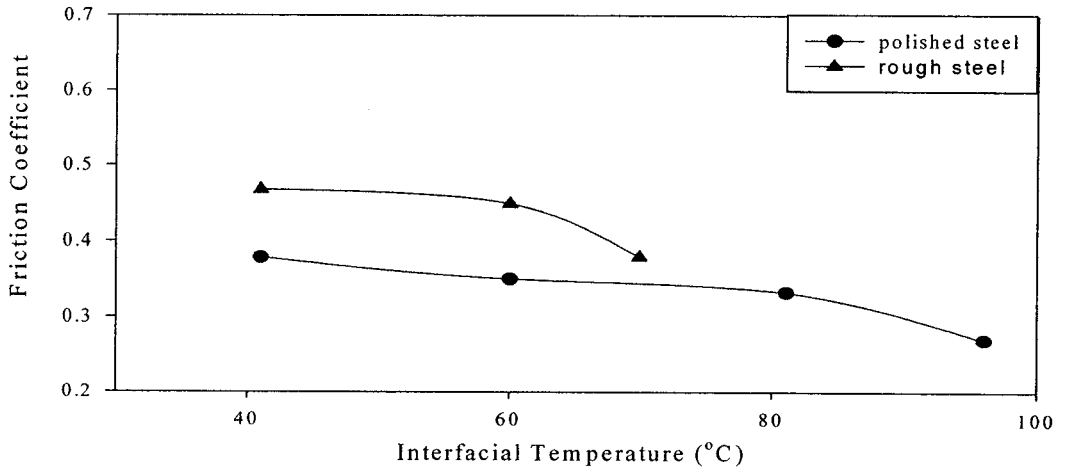

(C) P=13.47 MPa

Figure 3.12: COF as a function of interface temperature for polished steel plate and rough steel plate at N=8.5 rpm.

3.3.3 Pressure effect for polished and rough steel plates

For polished steel plate, the COF decreased with increasing pressure for all temperatures (Figure 3.13). At 41°C, coefficient decreased sharply with the increasing pressure, at 60°C, the COF curve had a similar trend as that of 41°C, with lower absolute values of COF. For COF at 80°C, it decreased slightly with the increasing pressure.

As Figure 3.13 indicates, at a temperature of 41°C, COF decreased sharply with the increasing pressure for both polished steel and rough steel plate. At a temperature of 60°C, the COF shows similar trend as the one at 40 °C with lower values. Because the great emissive ability of the rough steel plate and power limitation of heater band, the temperature of the band could be raised up to only 66°C, which made interface temperature for rough steel plate 10°C lower than that of polished steel plate. This introduced a certain degree of inaccuracy in the curve at high temperature. Figure 3.13 indicated that COF decreased slightly with increasing pressure for both polished steel plate and rough steel plate at relative high temperature.

Similar trends for the effect of temperature and pressure on functional behavior of PVC were measured at velocities of 5 and 12 rpm.

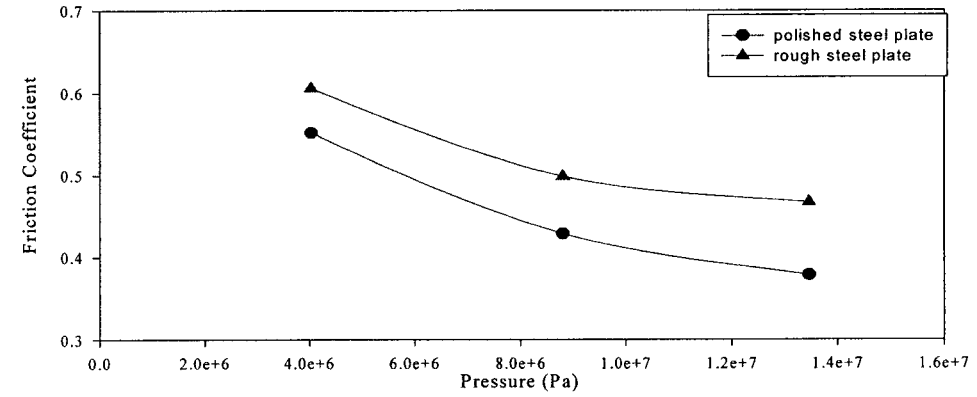

(A) T=41°C

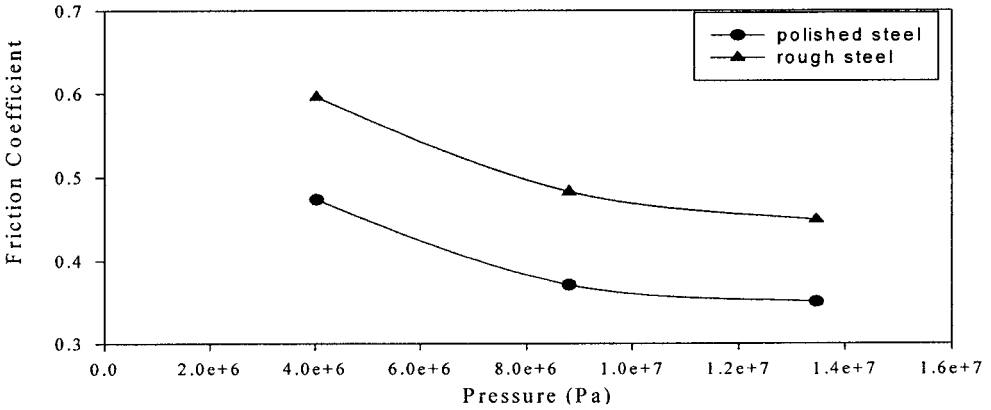

(B) T=60°C

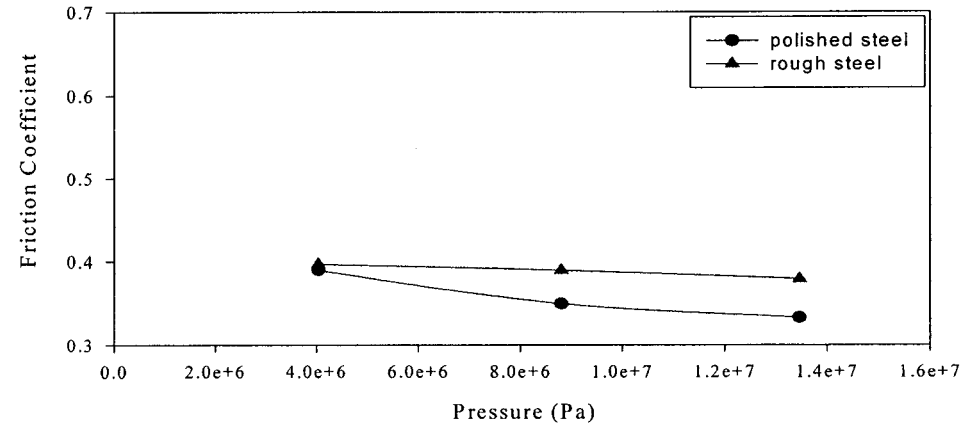

(C) Polished steel T=81°C, rough steel T=70°C

Figure 3.13: COF as a function of pressure for polished steel plate and rough steel plate. N=8.5 rpm.

3.3.4 Mechanical melting phenomena

Previous researches indicated the existence of a melting behavior of a polymer due to friction-generated heat on a metal surface, which is at a temperature lower than the melting or glass transition point of the polymer. Chung called this phenomenon "mechanical melting". Mechanical melting occurs at a progressively lower steel plate surface temperature as pressure or speed was increased, even at room temperature as pressure or speeds were sufficiently high. Some scientists considered that the polymer adhered to the metal surface causing the frictional force to fracture the interior of the sample away from the metal-polymer adhesion interface. The mechanical energy dissipated during the fracture is sufficient to cause the polymer to melt. Mechanical melting did happen in our experiment for PVC plate at a pressure of 4 MPa with an interface temperature of 60°C and a speed of 8.5 rpm. Since the thermal conductivity is very low for PVC resin, the heat cannot be conducted out quickly, and thus the local temperature increased dramatically resulting in a partially melted sample which will adhere to the PVC plate. In order to avoid the mechanical melting, we chose relatively low interface temperature and low pressure in all the experiments for PVC plate.

3.3.5 Experiment results for PVC plate

In our experiments, we replaced the steel plate with a PVC plate to estimate the coefficient of friction between PVC and PVC. As mentioned previously, because of the poor heat conductivity of PVC, the interface temperature underneath the sample reached high values as the pressure was increased. The calculated interface temperature was even higher than PVC melting temperature (~150°C). We know that mechanical melting occurs before that melting temperature. To avoid mechanical melting, we had to do our experiments at relatively low pressure (0.94 MPa to 2.95 MPa) and temperature (52°C to

67°C). Figure 3.14 and 3.15 show that the COF decreases with an increase of temperature and pressure. At pressure 0.94 MPa and 1.94 MPa, COF decrease almost linearyly with increasing temperature. At 2.95 MPa, COF does not change with increasing temperature. At temperatures of 53°C and 60°C, the COF dropped rapidly with increasing pressure. At 66°C, the COF decreased slightly with increasing pressure. Although the operation conditions were not exactly the same as that of polished and rough steel plate, it was found that COF of PVC was higher than those of polished steel and rough steel for most of the operating conditions.

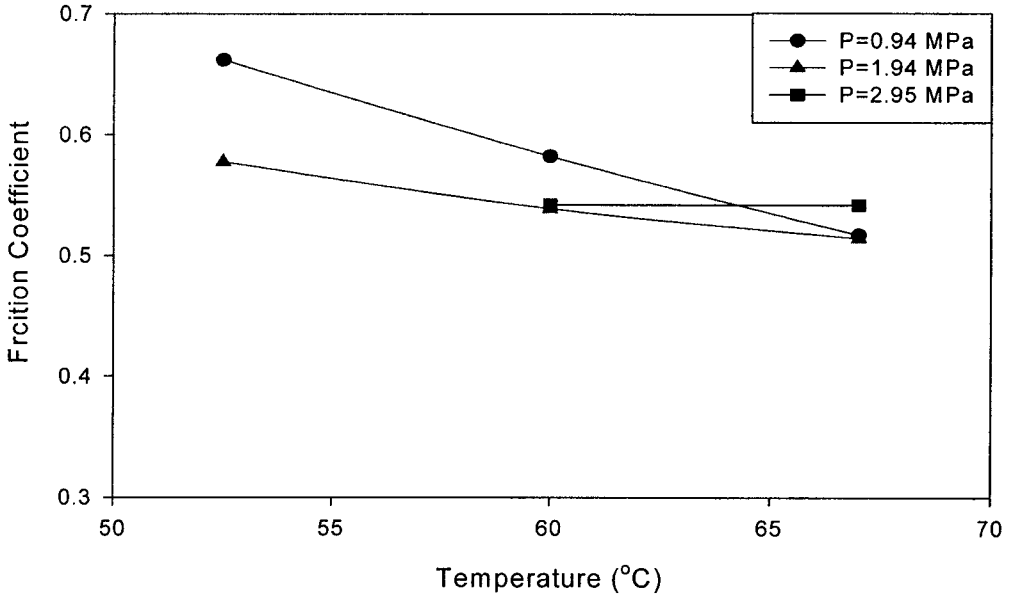

Figure 3.14: COF as a function of interface temperature for PVC plate at N=8.5 rpm

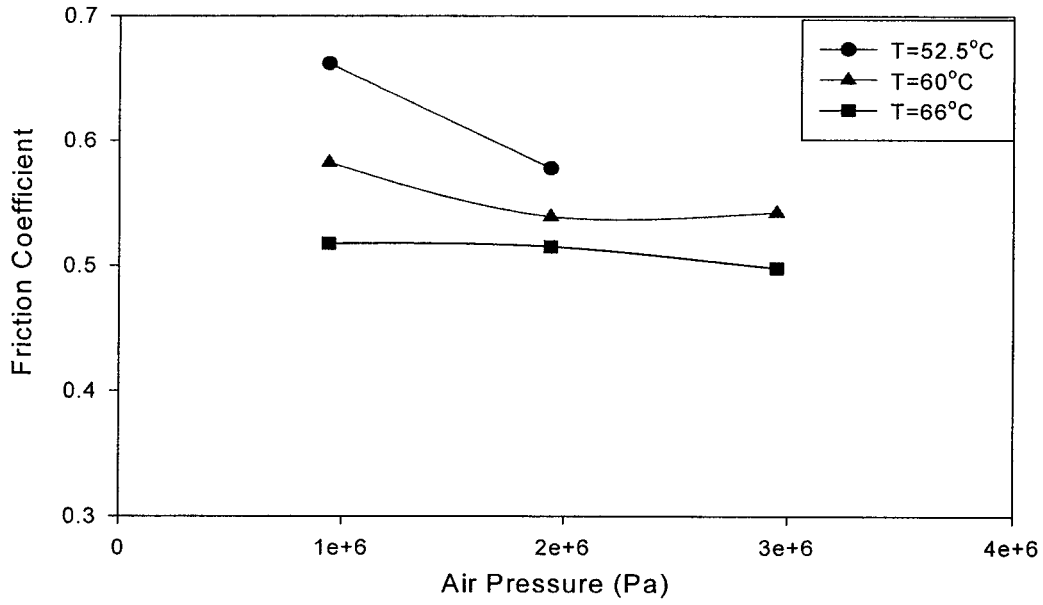

Figure 3.15: COF as a function of pressure for PVC plate, N=8.5 rpm.

3.4 COF modeling

3.4.1 Relations to solids conveying

The COF data will be used as friction factors in a new non-plug flow model to simulate the solids conveying. It is very important to know if the friction data of PVC are consistent with the true COF value of solids conveying during extrusion. Frictional forces are the driving force for a polymer slab that moves in the screw channel of the solids conveying. Generally, polymer-barrel friction forces (F_b) must be greater than polymer-screw root friction force (F_s). For this condition, pressure will increase in the down-channel direction. If F_s is greater than F_b, the pressure will decrease in the down-channel. However, this negative pressure gradient cannot be sustained since the pressure in the channel quickly drops to zero and solids will no longer convey. The frictional forces are directly related to dynamic COF, contact areas, and pressure ($F_b = \mu_b \frac{P}{A}, F_s = \mu_s \frac{P}{A}$). Thus if COF of rough steel plate (forward force) were always greater than that of polished steel plate (drag force), then steady conveying of the solids will always occur.

Previous researches (Spalding et al., 1993) indicated that if COF for polished steel does not show minimum and /maximum value as a function of temperature, and if the COF for polished steel increases with increasing speed, then the above condition will be easily satisfied via processing conditions and thus solids conveying occur. But if the COF decreases with increasing speed, then solids conveying will be difficult because there is a possibility for the drag force exceed the forward force.

In our case, COF for polished steel was relatively independent of speed, and did not show minimum or maximum value as a function of temperature. For this reason, it can be said that the COF data were consistent with the solids conveying during extrusion.

3.4.2 Mathematic models for COF

In order to use the COF in our solids conveying model, we need a mathematic representation of the coefficients. COF were estimated by using regression curve fit (see Appendix III) with both temperature and pressure. Because of the limitation of the friction coefficient measurement device, the experimental temperature range (as shown in Table 3-2) is lower than those of extrusion processing. As the temperature or pressure exceeds the measurement data range, a constant value will be assumed according to the curves trend. Instead of using constant COF values of barrel and screw for all the parts of the extruder, this experimental results make it possible to estimate instantly change COF for barrel and screw surface, as well as internal COF between PVC and PVC. That makes our simulation much closer to the real conditions. The equations used in simulation of COF for barrel, screw, as well as internal friction coefficient, are shown in table 3-3. Figure 3-16 indicates the comparison of experimental and fitted values of COF.

Table 3- 2: Comparison of operation conditions ranges between three types plate and practical extrusion.

	Polished steel plate	Rough steel plate	PVC plate	Practical extrusion
T (°C)	40°C-81°C	40°C-70°C	53°C-67°C	80°C–130°C
P (MPa)	4.03-13.47	4.03-13.47	0.94-2.94	0-14
N (rpm)	5-12	--	--	12-36

Table 3- 3: Equations used to calculate friction coefficients

Coefficient	Equation
f_b	$f_b = -0.2577+3.927*10^{-2}*T-3.009*10^{-8}*P-3.962*10^{-4}*T^2+1.108*10^{-15}*P^2$
f_s	$f_s = 0.8187-5.249*10^{-3}*T-3.53*10^{-8}*P+2.342*10^{-5}*T^2+1.304*10^{-15}*P^2$
f_i	$f_i = 1.478-1.99*10^{-2}*T-1.127*10^{-7}*P+1.073*10^{-4}*T^2+2.385*10^{-14}*P^2$

(Temperature: °C; Pressure: Pa.)

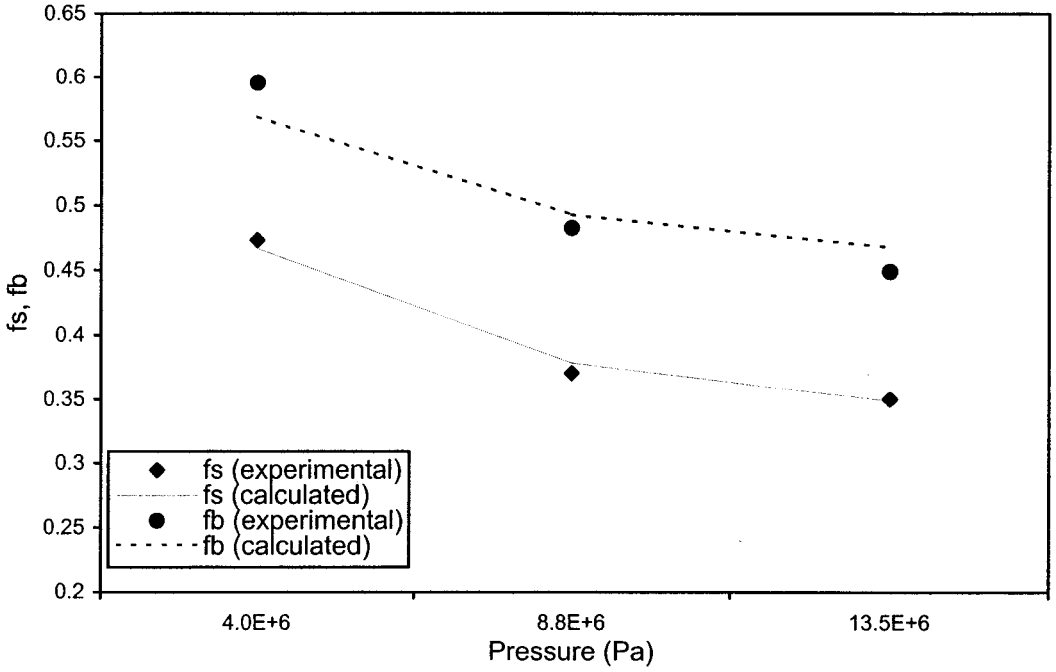

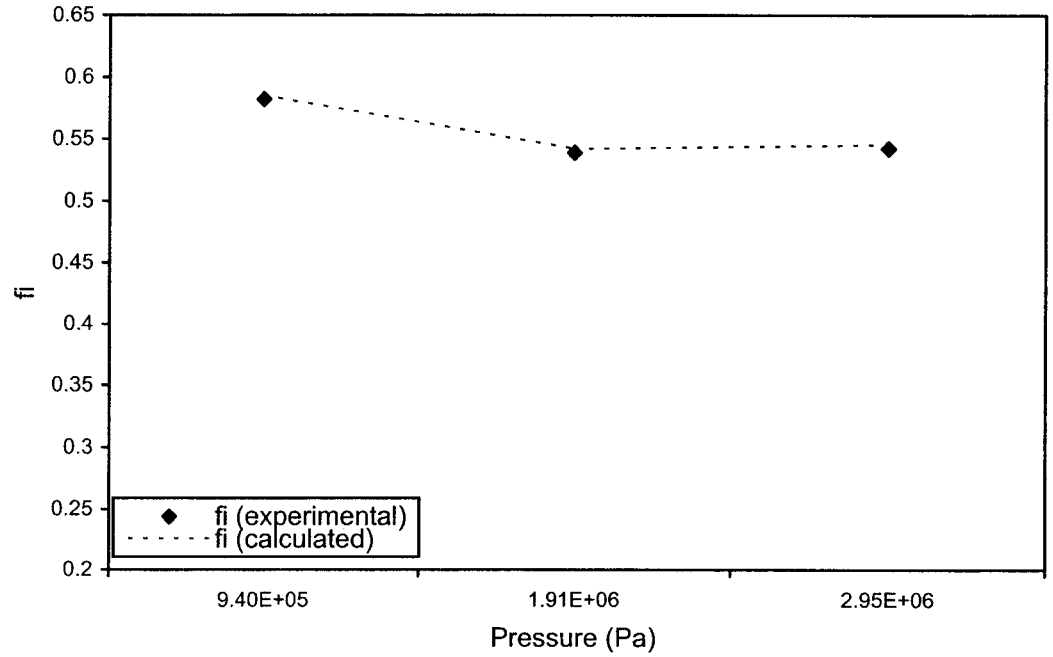

Figure 3.16: Comparison of experimental and calculated values for f_s, f_b, and f_i at interface temperature is 60 °C.

3.5 Conclusion

A new friction measurement device was designed for data collection under typical extrusion conditions for three types of plate, which represented barrel, screw, and internal interface of the extruder. The experimental results showed that COF for the three plates decreased with increasing pressure and interface temperature. Rotation speed slightly affects COF. It was clear that the frictional behavior of a polymer depends on temperature, pressure and speed in a complicated manner. Furthermore, the dependence of the frictional behavior on temperature, pressure and speed can be quite different from one polymer to another. Therefore, a simple extrapolation of the frictional coefficients in terms of temperature, pressure and speed cannot be trusted.

From the literatures, we know the dynamic COF for PVC in a range from 0.2 to 0.7. The experimental COF values show a good correlation to the reference values.

CHAPTER 4: A SOLIDS CONVEYING MODEL ALLOWING MATERIAL DEFORMATION

4.1 Advantage of this model

Since little attention has been paid to solids conveying in comparison with the other functional zones, solids conveying is usually considered as a minor part of the plasticating process. Most analyses still follow the main assumption of the first generation model proposed by Darnell and Mol (1956), pioneers of the solids conveying theory, who assumed that the solid pellets are compacted into a solid plug subjected to frictional forces at the barrel and screw surface. After Darnell-Mol's work, Schneider (1969) proposed a method to account for the non-isotropic pressure distribution; Tadmor and Broyer (1972) corrected this model with non-isothermal analysis and changed bulk density; Lovegrove (1974) added gravity force in force balance; Cambpell et al. (1995) analyzed the push force exerted by the flights on the screw; Spalding et al. (1992) used changed dynamic friction and lateral stress ratio in their model. Although the initial model has been progressively improved by different analyses, making it more realistic, its framework remains virtually unchanged. The first generation model provides a convenient tool for understanding and optimizing the solid conveying process. Because of the simple assumption of "solid plug" is far from the real condition, especially during first few turns of the screw, in which the plastic granules slip, one relative to another. That makes the computed results of pressure profile and energy consumption unreasonably high. Experimental observations show a non-plug flow zone at the beginning of the feed section.

About ten years ago, Fang et al. (1991) proposed a second-generation model. In their non-plug flow model, the authors considered the solid material in the screw channel as

bulk granules, with relative movement between granules. They supposed this bulk pellets system is a linear elastic system, and do not satisfy the assumption of pressure isotropy. According to these assumptions, they computed three-dimensional velocity and stress profiles of the pellets in the first few turns, before the generation of the solid plug. The loose pellets have little shear resistance and flow under the influence of small applied forces. Since a multi-dimensional velocity is used instead of a constant speed motion for the solid plug, internal friction is dominant over the relative motion between pellets and pellets. The internal friction is an important factor that decides the length of the non-plug flow zone, and it depends on the pellets shape, hardness, size, and surface characteristics. In Fang et al.'s model (1991), authors used elastic mechanics and finite element method to build a mathematical model. Based on their basic assumptions, we try to develop a two-dimensional model by the element stress analysis, which introduces internal friction force in the force balance and can predict the pressure profile and flow rate accurately. To verify our assumptions, we used different shapes of PVC plastic in the experiments; the experimental results show a good correlation between the model and simulation results.

4.2 A new non-plug solid flow model

4.2.1 Physical model

The basic theory is similar to Fang and Chen's model (1991). We consider the solid material in the screw channel as bulk pellets. The main difference between "solid plug" and "bulk pellets" is that the former does not satisfy the assumption of isotropic pressure and velocity, and there if relative motions between pellets. It seems clear that during the extrusion there is a non-plug flow zone in the screw feed section.

The physical model is shown in Figure 4-1. To simplify the geometry of the flow domain, the helical channel of a screw extruder is unwound into a straight channel and the barrel is treated as an infinite plate moving on top of the straight channel. The analysis is simplified by using a two-dimensional channel. Polymer flows in x direction, V_b represents the barrel velocity. In our simulation, the screw channel is divided into 135 thin slices with the same length and height H. We suppose each slice has the same physical property and velocity, and the polymer slices move to the down channel direction in a non-constant velocity V=f (x,y).

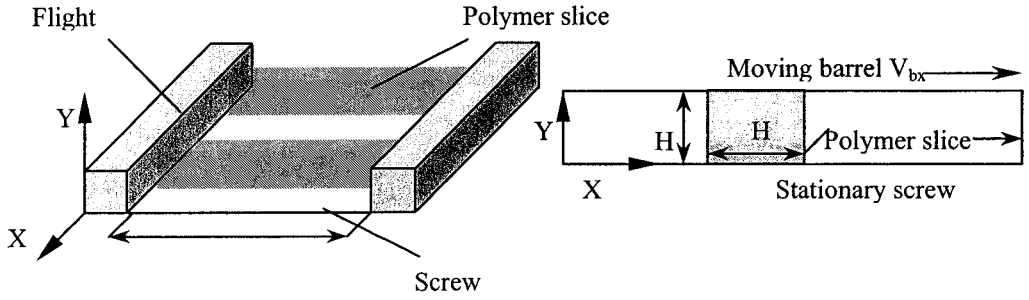

Figure 4.1 Physical model for non-plug solid conveying theory

The basic assumptions are as below:

1. The solid conveying process is steady: the barrel is treated as rotating opposite to the stationary screw.
2. The flight clearances can be neglected.
3. Gravitation force of the material is neglected.
4. The polymer slices only flow in the X direction.
5. The internal, barrel, and screw friction coefficients vary with the temperature, pressure, and velocity.

6. The friction coefficient of the flight can be neglected.
7. The density of the bulk polymer varies with the temperature and pressure.
8. The solids conveying movements were non-isothermal.
9. The pressure and velocity of the polymer are considered anisotropic.

Since we assumed no friction on the flight surface, this is a two dimensional problem.

4.2.2 Two-dimensional stress analysis for polymer slices:

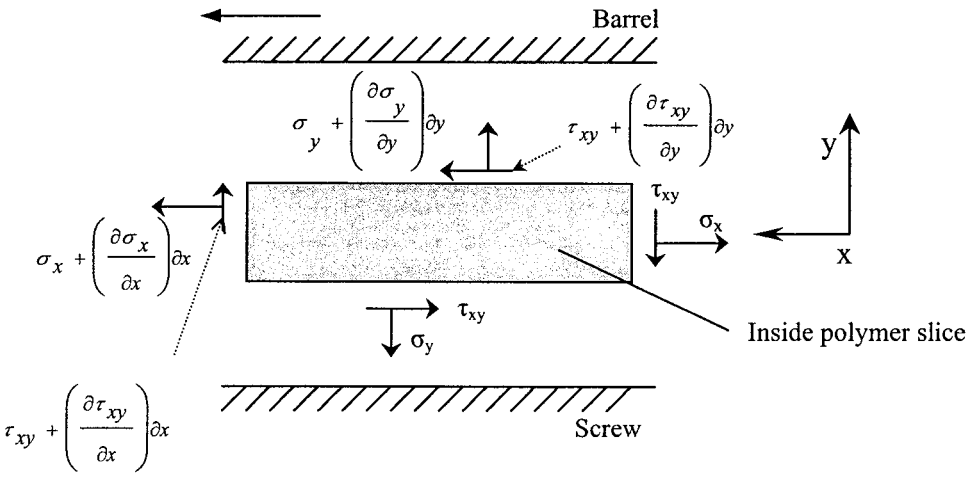

Figure 4.2 Two-dimensional stress analysis

From solid continuum mechanics, we have:

$$\begin{cases} \dfrac{\partial \sigma_x}{\partial x} + \dfrac{\partial \tau_{xy}}{\partial y} = 0 \\ \dfrac{\partial \tau_{xy}}{\partial x} + \dfrac{\partial \sigma_y}{\partial y} = 0 \end{cases} \qquad 4\text{-}1$$

With Coulomb's law of friction:

$$\tau_{xy} = -f_i \sigma_y \qquad 4\text{-}2$$

Where σ is the normal stress, and τ is the shear stress.

If $\partial\sigma_x / \partial x$ (pressure drop or rise) is known, from equations 4-1 and 4-2 one obtains:

$$f_i * \left(\frac{\partial \sigma y}{\partial x}\right) = \left(\frac{\partial \sigma y}{\partial y}\right); \qquad 4\text{-}3$$

and

$$f_i * \left(\frac{\partial \sigma y}{\partial y}\right) = \left(\frac{\partial \sigma x}{\partial x}\right) \qquad 4\text{-}4$$

From equations 4-3 and 4-4, one gets:

$$\left(\frac{\partial \sigma y}{\partial y}\right) = \frac{1}{f_i} * \left(\frac{\partial \sigma_x}{\partial x}\right) \qquad 4\text{-}5$$

$$\left(\frac{\partial \sigma y}{\partial x}\right) = \left(\frac{1}{f_i}\right)^2 * \left(\frac{\partial \sigma_x}{\partial x}\right) \qquad 4\text{-}6$$

with boundary conditions:at y=0, $\sigma_y=\sigma_s$; at y=H, $\sigma_y=\sigma_B$.

after integration of Eq.4-5, one obtains this important equation for inner polymer slice:

$$\sigma_B - \sigma_s = \left(\frac{H}{f_i}\right)\left(\frac{\partial \sigma_x}{\partial x}\right) \qquad \text{Equation I}$$

4.2.3 Stress balance on a solid conveying element:

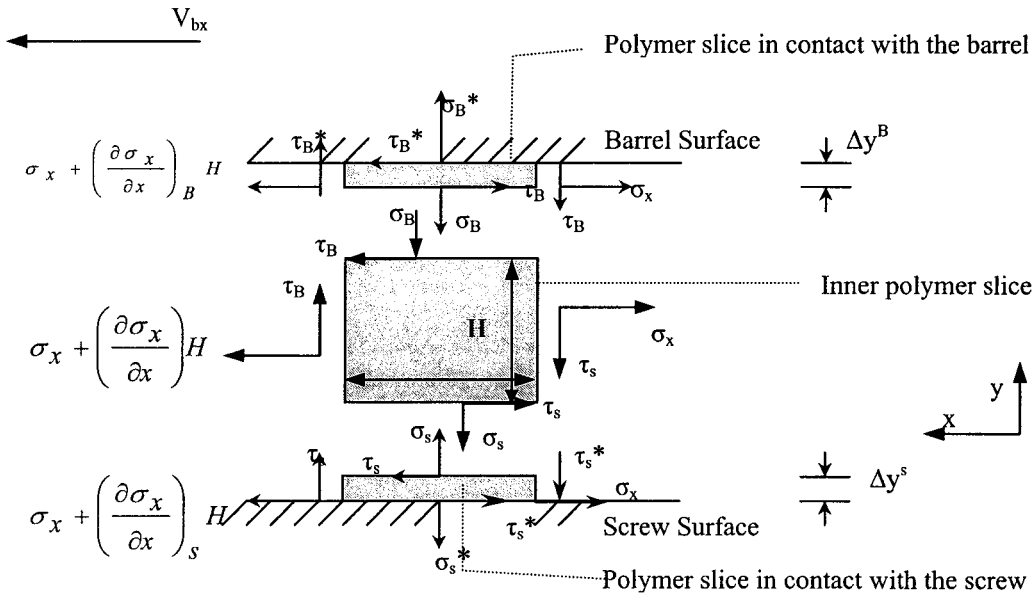

Figure 4.3 Stress analysis of an element for the polymer in the screw channel.

From above stress analysis for inner polymer slice, we get the stress balance along the y-direction (Appendix I):

$$\sigma_B - \sigma_s = \tau_s - \tau_B$$

$$= -f_s\sigma_s + f_b\cos(\theta+\phi)\sigma_B \qquad \text{Equation II}$$

Similar, we can obtain stress balance for the polymer slices in contact with the barrel and screw surface

$$\sigma_B^* - \sigma_s^* = \tau_s^* - \tau_B^* = H\left(\frac{\partial\sigma_x}{\partial x}\right) \qquad \text{Equation I*}$$

σ_s^* and σ_B^* are the normal stresses at the barrel and screw surfaces, they are different from σ_s and σ_B.

$$\sigma_B^* - \sigma_s^* = \tau_s^* - \tau_B^* = -f_s\sigma_s - (-f_b\sigma_s^*\cos(\theta+\phi)) \qquad \text{Equation II*}$$

4.2.4 Φ angle calculation:

Eq.I and Eq.II could be arranged as follows:

$$\frac{H}{f_i}\left(\frac{\partial \sigma_x}{\partial x}\right) = -f_S \sigma_S + f_b \cos(\theta + \phi)\sigma_B \qquad 4\text{-}7$$

To calculate Φ, we need to know ($\sigma_B - \sigma_S$). Since ΔP ($\partial\sigma_x / \partial x$) is known, σ_s is known from the boundary condition, then only σ_B and Φ are two unknown variables.

Substituting Eq.I ($\sigma_B = \left(\frac{H}{f_i}\right)\left(\frac{\partial \sigma_x}{\partial x}\right) + \sigma_s$) into Eq.4-7, and rearrange it, one obtains:

$$\cos(\theta + \phi) = \frac{\frac{H}{f_i}\left(\frac{\partial \sigma_x}{\partial x}\right) + f_s \sigma_s}{\frac{f_b H}{f_i}\left(\frac{\partial \sigma_x}{\partial x}\right) + f_b \sigma_s} \qquad 4\text{-}8$$

Angle Φ is obtained as below:

$$\boxed{\phi = \cos^{-1}\left[\frac{(H/f_i)\frac{\partial \sigma x}{\partial x} + f_S \sigma_S}{(f_b H/f_i)\frac{\partial \sigma x}{\partial x} + f_b \sigma_S}\right] - \theta} \qquad 4\text{-}9$$

And the boundary condition is known as:

$$\sigma_S = \sigma_0 + \sum \frac{\partial \sigma x}{\partial x} * \frac{H}{2} * \frac{1}{fi^2} \qquad 4\text{-}10$$

σ_0 is the initial pressure of the extruder, and it is supposed to be zero. For barrel and screw surfaces touched by polymer slices, the boundary condition changes as follows:

$$\sigma_s^* = \sigma_o^* + \sum \frac{\partial \sigma x}{\partial x} * \frac{H}{2} * \frac{1}{fi^2} \qquad 4\text{-}11$$

Similar as inner polymer slice, with Eq.I* and Eq.II*, one obtains:

$$H\left(\frac{\partial \sigma_x}{\partial x}\right) = -f_s\sigma_s - (-f_b\sigma_s^* \cos(\theta+\phi)) \qquad 4\text{- }12$$

Substituting Eq.I* ($\sigma_B^* = H\left(\frac{\partial \sigma_x}{\partial x}\right) + \sigma_s^*$) into Eq.4-12, one obtains:

$$\cos(\theta+\phi) = \frac{H\left(\frac{\partial \sigma_x}{\partial x}\right) + f_s\sigma_s^*}{Hf_b\left(\frac{\partial \sigma_x}{\partial x}\right) + f_b\sigma_s^*} \qquad 4\text{- }13$$

$$\boxed{\phi^* = \cos^{-1}\left[\frac{H\frac{\partial \sigma_x}{\partial x} + f_S\sigma_S^*}{f_bH\frac{\partial \sigma_x}{\partial x} + f_b\sigma_S^*}\right] - \theta} \qquad 4\text{- }14$$

Φ is involved in f_i, f_s, f_b, σ_s, and $\partial\sigma_x/\partial x$. Since these five variables are function of operation conditions during the extrusion, solution for Φ involves numerical iteration.

4.2.5 Velocity profile calculation:

Since the goal of this model is to provide a relationship that will predict extruder output, the down-channel velocity V is required. We know that:

$$\dot{\gamma} = \frac{dV_x}{dy} = \frac{d\gamma}{dt} = \frac{d\gamma}{dx} * \frac{dx}{dt}, \text{with}$$
$$V = \frac{dx}{dt} \qquad 4\text{- }15$$

$$\boxed{\frac{dV}{dy} = V * \frac{d\gamma}{dx}} \qquad 4\text{- }16$$

and $\frac{d\gamma}{dx}$ can be obtained from the stress profile:

$$\frac{d\gamma}{dx}=\frac{1}{G}*\frac{d\tau_{xy}}{dx}=\frac{-f_i}{G}*\frac{\partial\sigma_x}{\partial x}=\frac{-1}{Gf_i}*\frac{\partial\sigma_x}{\partial x},\ with \qquad 4\text{-}17$$

$$\tau=G*\gamma$$

We obtain:

$$\frac{dV}{dy}=\frac{-1}{Gf_i}*\frac{\partial\sigma_x}{\partial x}*V \qquad 4\text{-}18$$

With boundary condition: y=0, V=V_s

$$\boxed{V=Vs*\exp\left\{\frac{-\partial\sigma_x}{\partial x}*\frac{y}{Gf_i}\right\}} \qquad 4\text{-}19$$

4.2.6 Flow rate calculation:

$$Q_v=W\int_0^H V(y)*dy \qquad 4\text{-}20$$

Substituting Eq.4-17 in, and got:

$$Q_v=W*\int_0^H V_s*\exp\{(-\partial\sigma_x/\partial x)*[y/(G*f_i)]\}*dy$$

$$=\frac{Gf_iWV_s}{-\frac{\partial\sigma_x}{\partial x}}*\left\{\exp\left[\left(\frac{\partial\sigma_x}{\partial x}\right)*\left(\frac{H}{Gf_i}\right)\right]-1\right\} \qquad 4\text{-}21$$

If we express the flow rate as a function of the velocity near the barrel (V_{NB}), the equation 4-21 becomes:

$$Q_v=\frac{Gf_iWV_{NB}}{-\partial\sigma_x/\partial x}*\left\{1-\exp\left[\left(\frac{\partial\sigma_x}{\partial x}\right)*\left(\frac{H}{Gf_i}\right)\right]\right\} \qquad 4\text{-}22$$

Velocity near the barrel (V_{NB}) is the same as Tadmor and Klein's model (1972):

$$V_{NB} = \frac{V_B \tan\phi}{\cos\theta * \tan\phi + \sin\theta} \qquad 4\text{-}23$$

Then, the flow rate becomes:

$$Q_v = \frac{Gf_i W}{-\partial\sigma_x / \partial x} * \frac{V_B \tan\phi}{\cos\theta * \tan\phi + \sin\theta} * \left\{1 - \exp\left[\left(\frac{\partial\sigma_x}{\partial x}\right) * \left(\frac{H}{Gf_i}\right)\right]\right\} \qquad 4\text{-}24$$

This expression is a function of the angle Φ, which is the angle of the barrel friction force measured from the barrel cross-section. This angle is obtained from the force analysis on the polymer element.

4.2.7 Pressure drops calculation:

An easy way to obtain pressure drops (or rises) is to calculate the axial stress profile (σ_x). However, since we neglect the friction effect of the flight, a more accurate way to calculate the pressure drops (or rise) for the inner polymer slice is to use the following equation:

$$P = \sigma_0 + \sum\left[\left(\frac{\partial\sigma_x}{\partial x}\right)H - \underbrace{\frac{f_i f_B \sigma_B \sin(\phi+\theta) * W}{H}}_{Friction\_on\_Flight}\right] \qquad 4\text{-}25$$

$$\sigma_B = \sigma_s + \left(\frac{H}{f_i}\right)\left(\frac{\partial\sigma_x}{\partial x}\right) \qquad 4\text{-}26$$

4.2.8 Thermal effect:

Like Tadmor and Broyer's model (1972), our model is non-isothermal. We considered the heat generated by friction on the barrel, the flights and the root of the screw. Most of the heat is generated on the barrel surface. Consequently, the surface temperature of the plug gradually increases as it slides down the channel. Because of the heat conduction into the solid plug, this increasing surface temperature leads to a gradual rise of the solid bed temperature. Although we consider a non-plug flow in the former part of screw feed zone, the polymer is compressed from bulk to something like a plug only at the end of the solid conveying zone, but the temperature profile is non-isothermal just like Tadmor and Broyer's model. As the bulk material slides down the channel, the polymer pellets are compacted; a temperature profile develops. This profiles change with down-channel distance and reach a maximum value at the barrel surface.

The general problem of heat transfer to a solid slab, initially at uniform temperature T_0, with a time varying heat flux at the surface, was treated by Carslaw and Jaeger (1959), who provided the following solution for the temperature distribution in the slab:

$$T_p(y,t) = T_0 + \frac{\alpha_p^{1/2}}{k_p \pi^{1/2}} \int f(t-\tau) e^{\left[-y^2/4\alpha_p t\right]} \frac{d\tau}{\tau^{1/2}} \qquad 4\text{-}27$$

where f (t) is the heat flux at the surface of the slab of the plug at y=0. From Eq.2-28 it follows that the heat flux into the plug equals the heat generation at the interface minus the heat lost through the cooled barrel (in which a linear profiles is assumed), thus:

$$f(t) = P_b f_b \pi N D_b \frac{\sin\theta_b}{\sin(\theta_b + \phi)} - \frac{k_b}{b}\left[T_p(0,t) - T_b(b,t)\right] \qquad 4\text{-}28$$

Substituting Eq.4-28 into Eq.4-27, and with all variables that are functions of time taken at t-τ. These include P_b, f_b, and T_p. Eq.4-27 can be solved numerically.

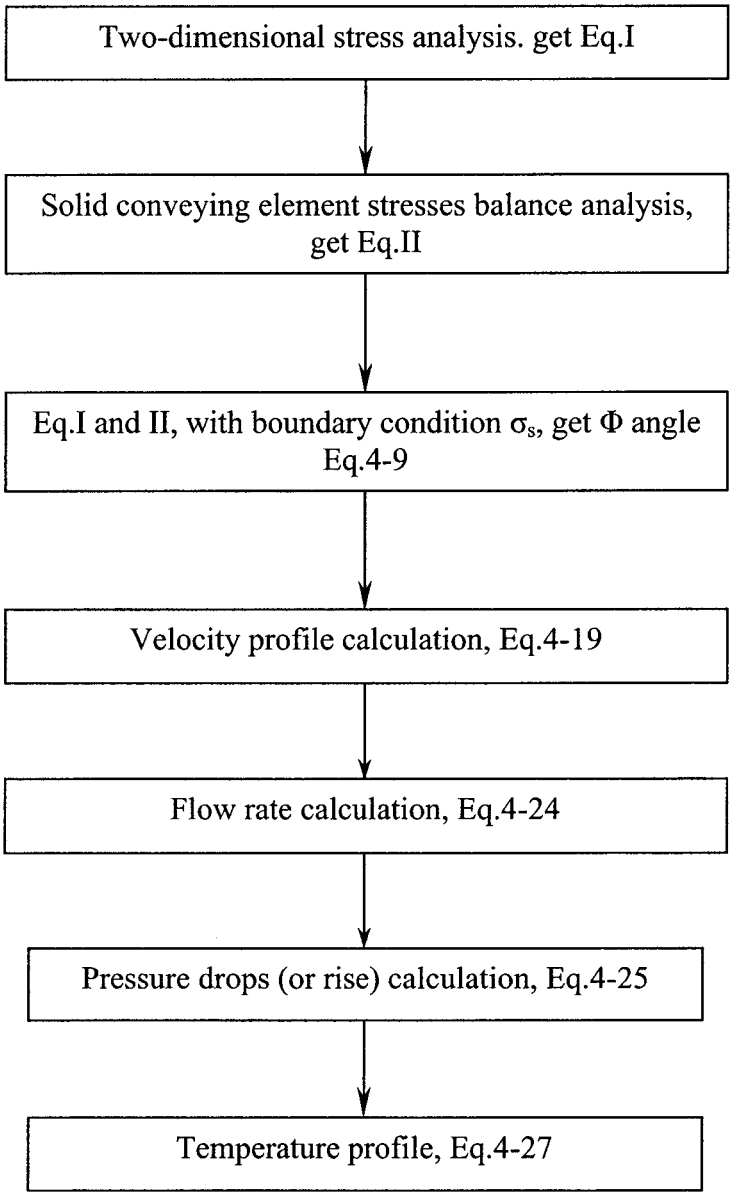

Figure 4.4 Algorithm for A new non-plug solid flow model

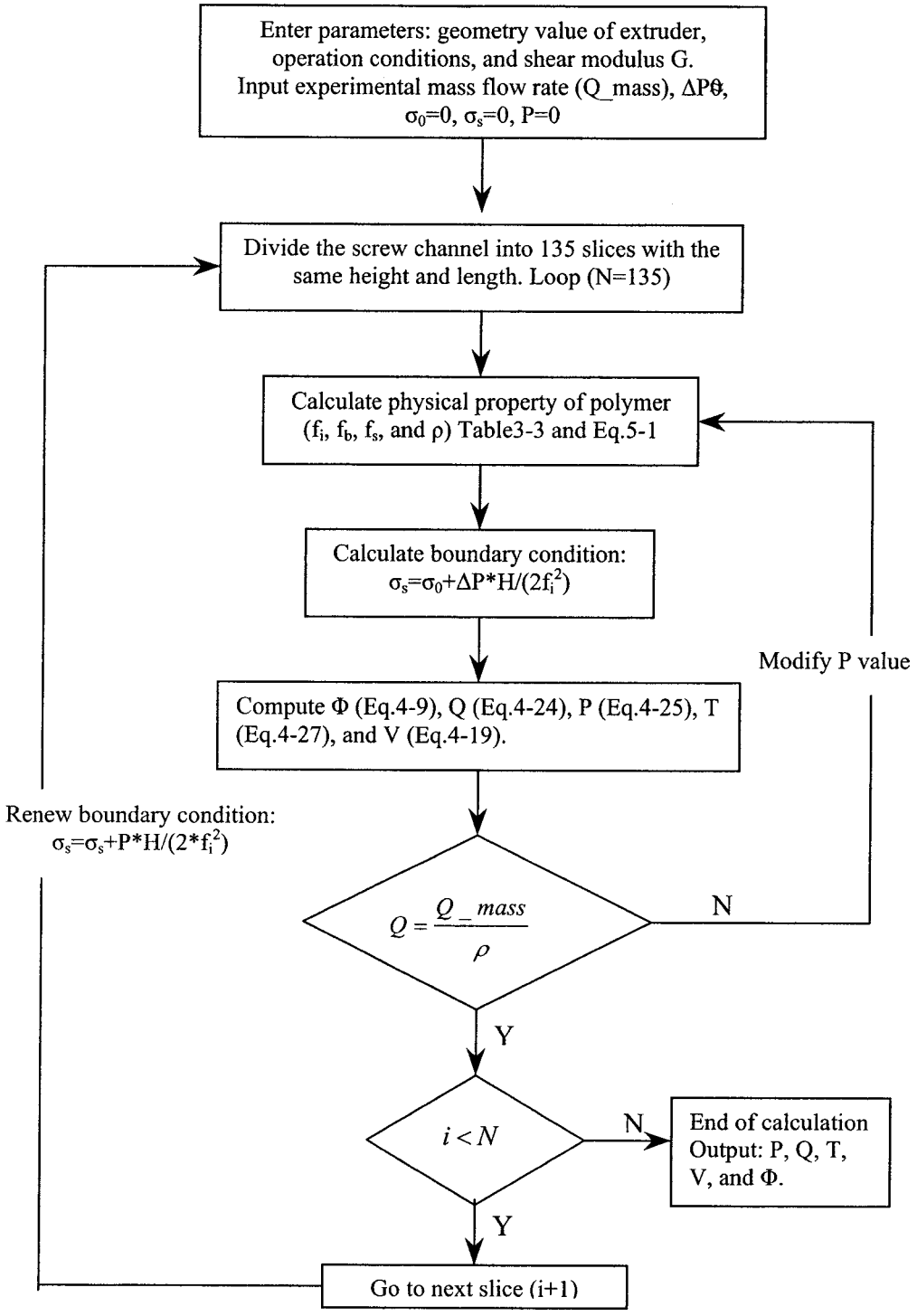

Figure 4.5 Numeric calculation algorithm

CHAPTER 5: EXPERIMENTAL VERIFICATION

5.1 Introduction

The goals of our experiments were to:

- Describe the solids conveying phenomena;
- Determine flow rate and pressure build-up of solids conveying as a function of material properties (i.e. pellet size, shape, and bulk properties);
- Use the experimental results in the non-plug solid flow model (new non-plug flow model) and modified Tadmor-Broyer model to help us predict the output of the solids conveying more accurately.

All of this work will help to develop a comprehensive model for the entire extrusion process.

5.2 Experimental method

5.2.1 Material

The PVC resin used in the study was the same than for COF measurements. Three different shapes of PVC resin were studied. The PVC resin, initially in a powder state, was extruded in a single-screw extruder and granulated to obtain pellets and flakes. After this process, the physical properties of the three shapes of PVC remained unchanged. Table 3-1 lists all the physical properties.

5.2.2 Experimental equipment

The solids conveying zone is the least understood process for single screw extrusion. This lack of understanding is due to:

- Unavailability of solids conveying rate data.
- There is no clear demarcation when the pellets or powder in contact with the barrel begin to melt, thus changing the nature of the frictional forces from dry friction to viscous drag.
- The compaction is anisotropic and changes according to the properties of the material.
- Friction coefficients are difficult to measure under dynamic conditions

Because of these difficulties and considering the lack of characterization of the phenomena involved, we need to build a new single-screw device, which enables to study solids conveying in a realistic and isolated situation. This new device can be used to measure the solids conveying rates as a function of barrel and screw temperatures, screw speed, and discharged pressure. Using the bulk density of PVC reported in literature and the dynamic friction coefficient measured previously (Chapter 3), we will be able to build a new non-plug flow model to predict the behavior in the solids conveying zone.

The solids conveying device was constructed from a normal extruder. The standard barrel was removed from the extruder and it was replaced with a short barrel, providing for a total length-to-diameter ratio L/D of 8.3 (L=370 mm, D=45.5 mm). Pictures of the device are shown in Fig.5-1 and Fig.5-2. Heater bands are wrapped around the outer surface of the barrel for temperature control. To observe and record the solids conveying process, a transparent glass window replaces part of the barrel. A video camera, located

along the side of the glass window, is connected to a research quality VCR so that the resulting tapes can provide the necessary detail for the post processing. The camera is also connected to a TV monitor, so that the event can be simultaneously observed.

A short screw was fabricated for the device. This screw was square-pitched, had a flight width perpendicular to the flight of 4.5 mm. The depth of the single channel was constant and equal to 9 mm. The flight radius was 22 mm (see appendix V).

Pressure was applied to the end of the device using supported arms as shown by Fig.5-2. A piston is located at the end of the screw. The gap between the supported arm and matched plated that attached to the barrel can be adjusted by a bolt located at the top of the piston (see Fig.5-3). The piston was designed as a hollow cylinder and its edge was made something like a balustrade. To measure the applied force, a load cell is positioned at the end of supported arms. As the extruder is running, the piston moves because of the pressure build-up in solids conveying zone. This continues until the bold head of the piston contacts the load cell. At this time, we have to adjust the bolt to change the position of the piston in order to reach the balance of the two forces respectively exerted by air pressure and by pressure build-up in the solids conveying zone.

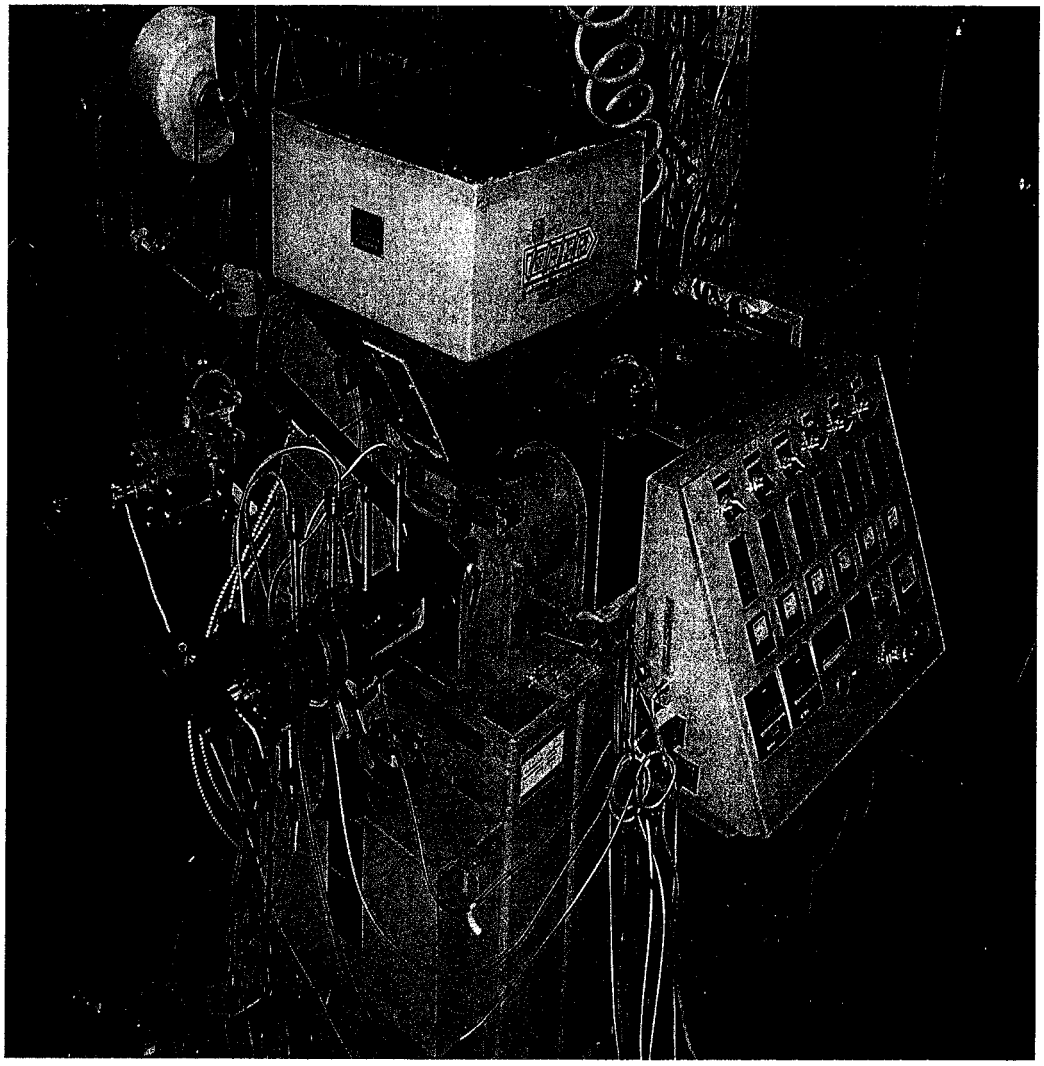

Figure 5.1 Over-all view of the solids conveying device

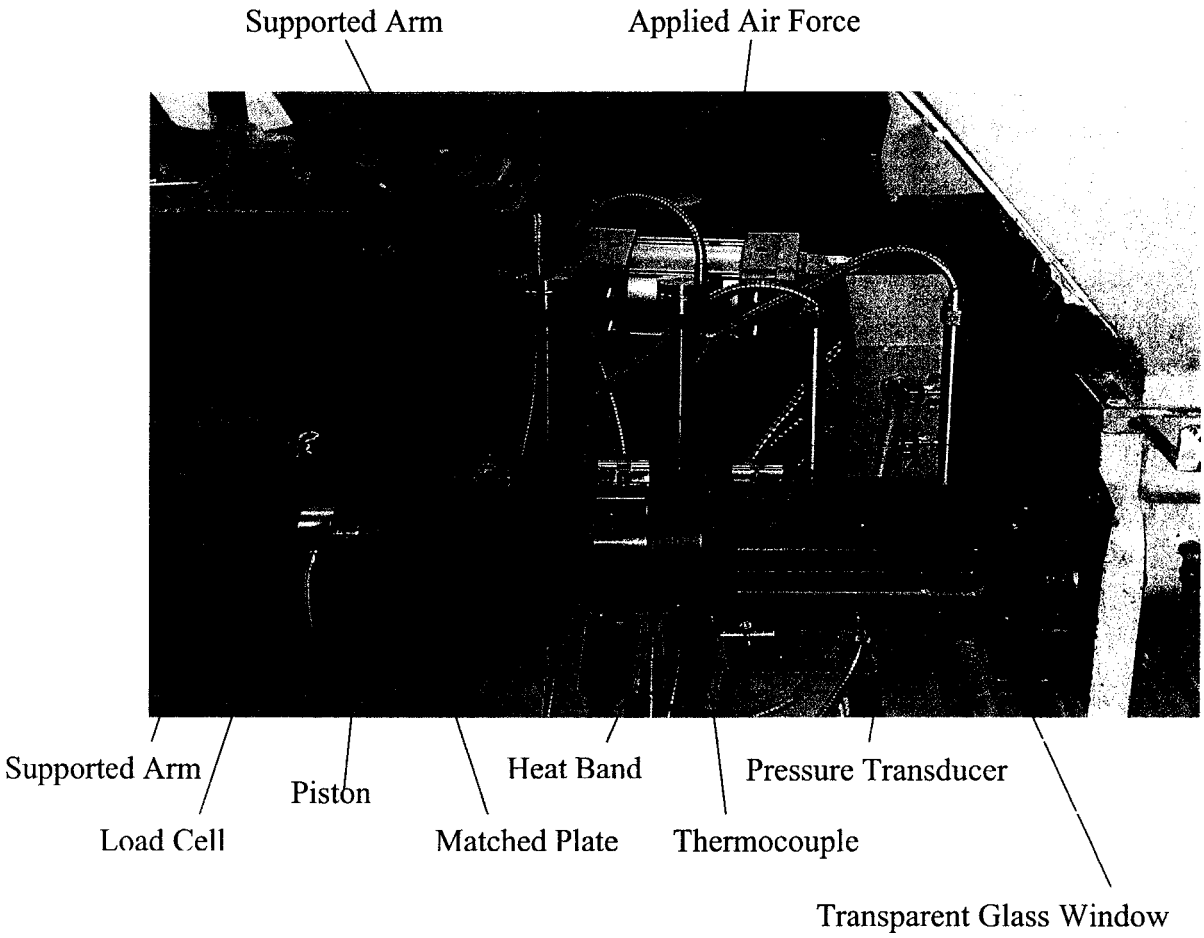

Figure 5.2 Schematic of the solids conveying device

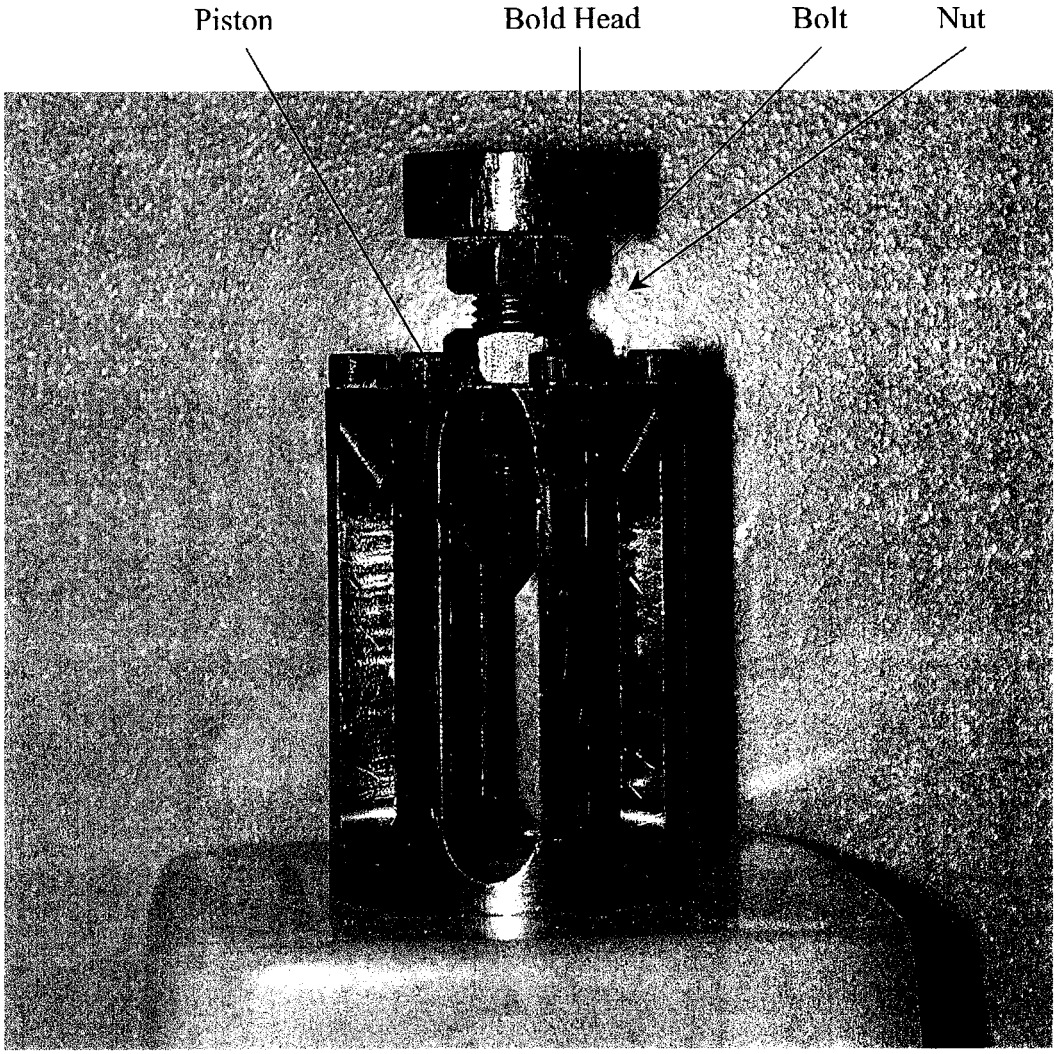

Figure 5.3 Piston located at the end of the screw

The mini-extruder that is described above was designed to study the following phenomena:

1. Solids conveying flow rate under various end pressures, rotational speeds, and barrel temperatures;
2. Solid bed compaction situations.

Besides, the device can also be used to measure or evaluate:

1. Pressures at the barrel wall with the help of pressure transducers;
2. Polymer element velocity angle (Φ) with respect to barrel;
3. Barrel surface temperature controlled by heat bands;
4. Bulk temperature of the exiting mass flow rate by a thermocouple;
5. Bulk density, ρ.

5.2.3 Experimental plan

Experiments were conducted on the three different shapes of PVC (powder, pellets, and flakes). In order to make on-line observation of solids conveying, a window located at the beginning of the extrusion process replaced one part of the barrel of the mini-extruder. This window was covered with thick optical glass. A camera and a video recorder were used to record the process.

To observe the compressive situation of the different shapes of polymer granules with different screws, the barrel without the window was placed on the mini-extruder and three types of screw were used. The characteristics of these three screws were: $pitch_1$=33.3 mm; $pitch_2$=44.5 mm; $pitch_3$=72.0 mm. The experiments were done under ambient temperature, zero discharged pressure and different screw speeds.

To observe the output of the three shapes of PVC during solids conveying as a function of the processing conditions (i.e. exit pressure, screw speed, and temperatures), we worked under two different applied pressures and two different screw speeds.

Since PVC flakes and pellets present large dynamic friction coefficient at low temperature, the friction force was very large and the extruder could not run properly. Therefore a temperature of 130 °C was used for PVC flakes. For powder and pellets, temperature greater than 60 °C and 110 °C were used respectively. The experimental results were recorded after the extruder had reached a steady state at the operating conditions imposed.

5.3 Experimental results

5.3.1 Experimental observation of the solids conveying

Most of the previous studies on the motion of the solid granules in a single-screw extruder are based on a "solid plug" assumption. According to this assumption, there are no relative movements between the granules. All the granules are packed like a plug and move down the screw channel with the same velocity and in the same direction during the extrusion process. Therefore, the solid plug is treated as a rigid body, which never experiences any deformation.

Our experiments indicated that the "solid plug" assumption is far from the real condition. We demonstrated that there exist not only relative movements between the solids granules, but also clearances among them. Sometimes, especially at the beginning of the extruder, we observed that the screw channel was not even completely filled with granules (Figure 5.4 through 5.6). It was only at the end of the solids conveying zone

that the solid granules were gradually compressed to something like a plug. But in most of the solids conveying zone, the relative motion between the granules is unavoidable.

The bulk system has less resistance to tensions, its shear resistance is small and the solid particles can flow if small external forces are applied. It satisfies the assumption of pressure anisotropy. As pointed out by Fang et al. (1991), the plug assumption is the main reason that leads to discrepancy between experimental and predicted results in Darnell-Mol's theory (1956).

Figure 5.4 to Figure 5.6 show pictures of the movement of solid granules in the extruder for PVC pellets, powder, and flakes. It was found that the powder moved in the screw channel much like liquid, and was easy to pack. That is due to the small granule size and to the large contact area between the granules and the barrel. Flakes were also compacted easily, due to large contact area between the granules and barrel. Finally, pellets were difficult to pack because of the relative large aspect ratio and small contact surface. According to the above analysis, we can conclude that the smaller or the larger the contact area of the granules, the earlier the plug is formed.

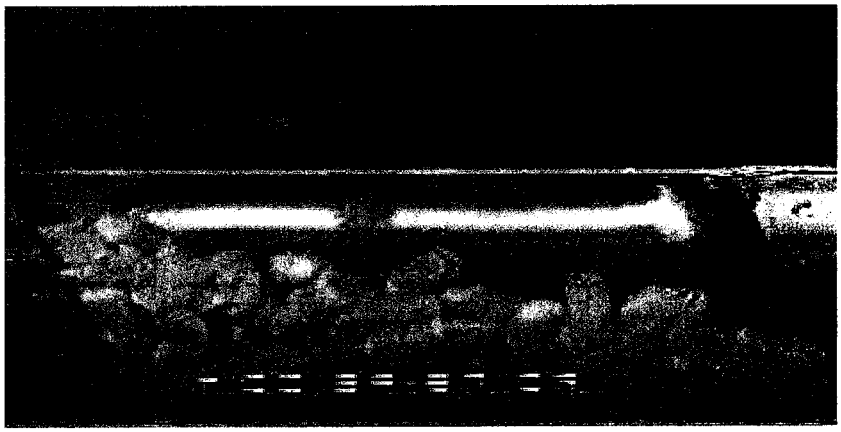

Figure 5.4 Photo for solid conveying zone. Material, PVC pellets.

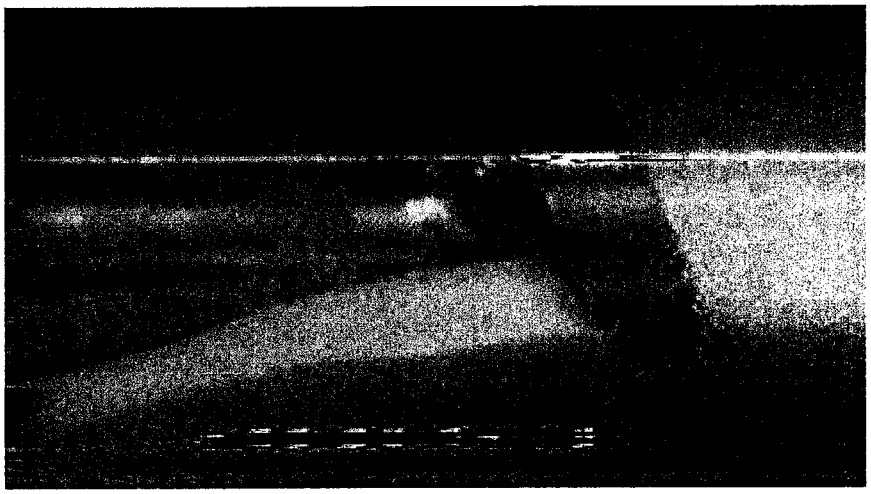

Figure 5.5 Photo for solid conveying zone. Material, PVC powder.

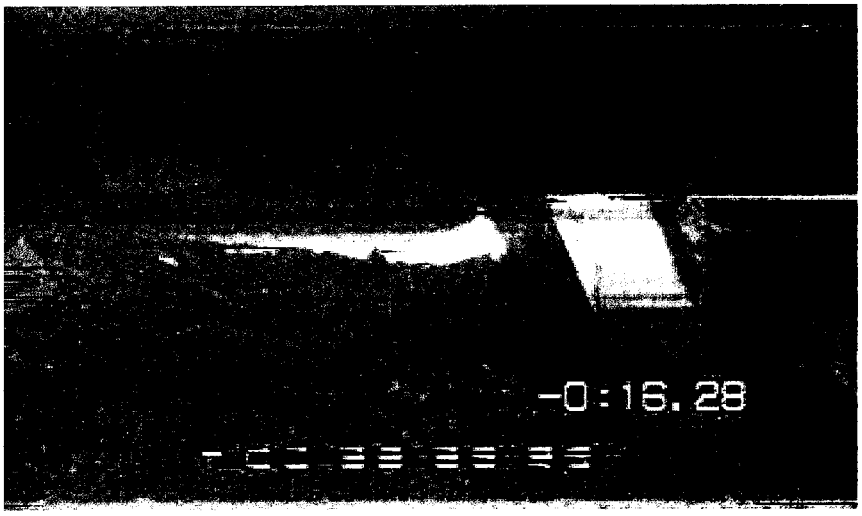

Figure 5.6 Photo for solid conveying zone. Material, PVC flakes.

5.3.2 Pressure measurement at the end of screw

To model the solids conveying, we need to know the exit pressure at down channel direction, P_z. The pressure transducer of the mini-extruder can measure the pressure at

the barrel wall at the end of the screw ($P_{x,z}$) (Figure 5.7). A load cell is able to read the force at the end of the solids conveying section. The pressure at the end of the device was calculated by dividing the measured force by the load cell by the cross-sectional area of the annulus created by the screw root and the inside barrel diameter. None of these two pressures can represent the down channel exit pressure. It is the major inconvenient of this device. According to the anisotropic stress distribution theory, the exit pressure at down channel is slightly higher than the pressure at the barrel surface. Therefore we have to approximate the exit pressure in the simulation by the one measured by the transducer.

The curve representing the pressure trace of P (x,z), measured by a transducer on the barrel, was unstable. It indicated that compaction or conveying was unstable. The time average pressure values were taken as the exit pressure of the solids conveying. In extrusion, the measured pressure is caused by the barrel drag, which acts in the (θ-Φ) direction (θ being the helical angle and Φ being the solids conveying angle calculated from the mass flow rate and bulk density) (figure 5.7). The force acting in the θ direction can be decomposed into two components in x (cross-channel) and z (down channel) directions. It is clear that F_x compacts the solids in the cross channel direction only, while F_z both conveys and compacts the bed in z-direction. F_z was responsible for the fluctuation in the pressure reading. We could conclude that the compaction load was triaxial, making the phenomenon more complex. This may explain "slip" or instability during conveying and compaction in extrusion.

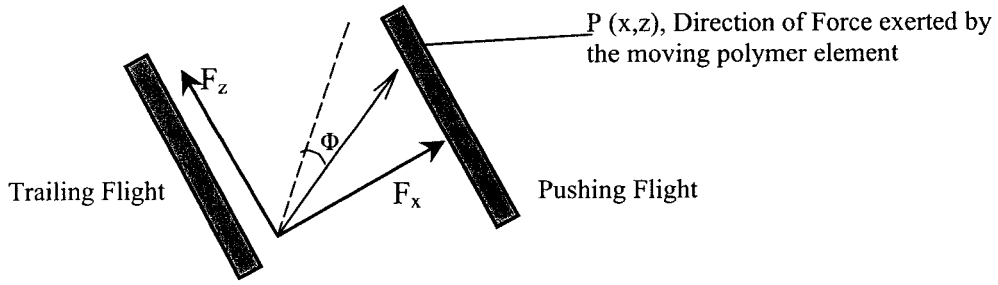

Figure 5.7 Section of an unwound channel: Measured pressure P(x,z); Calculated force Fx, and Fz

5.3.3 Determination of solids conveying rate

5.3.3.1 Solids conveying rate for different types of screws at zero pressure

Solids conveying rates were measured at a zero discharge pressure for three types of screws at ambient temperature. For these data, the piston and supported arm were removed, providing zero applied force from the air pressure. Since pressure build-up in solids conveying is very small and the polymer granules discharged were almost identical to those of the feed, we considered a zero pressure rise under these conditions.

Table 5- 1 Flow rate for different types of screws

Run	Shape	Screw pitch (mm)	Screw speed (rpm)	Flow rate
1	Powder	33.3	12	175.1
2		33.3	24	Neglected
3		44.5	12	188.9
4		44.5	24	378.9
5		72.0	12	270.8
6		72.0	24	540.4
7	Flakes	33.3	12	145.3
8		33.3	24	285.1
9		44.5	12	148.5
10		44.5	24	296.9
11		72.0	12	219.4
12		72.0	24	426.1
13	Pellets	33.3	12	165.6
14		33.3	24	315.6
15		44.5	12	196.3
16		44.5	24	381.4
17		72.0	12	344.9
18		72.0	24	683.3

As indicated by table 5-1, the solids conveying rates increased with increasing screw pitch. It seemed that the PVC pellets had the largest flow rate except for the smallest screw pith (33.3mm). An important point to notice is that the compressive situations were different for the three shapes of PVC plastic at the same operating conditions.

For the smallest screw pitch (33.3 mm), powder, flakes, and pellets all blocked inside the extruder because of the large frictional force. In this condition, the extruder could not run properly. To decrease the frictional force, the barrel temperature was increased to 60°C. Comparing the compressive situations of the three shapes, we found that powder compacted a little bit tighter than flakes, while pellets is the less compacted material among the three shapes. At zero applied pressure and ambient temperature, for the intermediate screw pitch (44.5 mm), powder was slightly compacted and flakes and pellets were uncompressed. For the largest screw pitch (72.0 mm), the three shapes of PVC were uncompressed.

5.3.3.2 Solids conveying rate at different barrel T and discharged P

Table 5- 2 Operation conditions

Operation conditions \ No.	Low	High
Temperature (°C)	70-80	130
Applied pressure (MPa)	0.21	0.48
Screw speed (rpm)	12	24

The solids conveying rates were measured as a function of barrel temperature for the three shapes of PVC plastic. A pressure transducer recorded the exit pressure, and the pressure data from the experiments were time-averaged.

Since PVC flakes could not be processed at low temperature, PVC pellets only at high applied pressure and at low temperature, we only compared the solids conveying rate of powder and pellets. The operating conditions were as following: applied pressure: 0.48 MPa; barrel temperature: 70°C and 130 °C.

As indicated by Fig. 5.8 (A), the solids conveying rates increased with increasing barrel temperature for all the shapes of PVC. The flow rate increased 10.8% (average value of PVC powder and pellets) while the temperature was increased from 70°C-80°C to 130°C.

The solids conveying rates were measured as a function of discharge pressure for three shapes of PVC at a barrel temperature of 130°C, as shown in Fig. 5.8 (B). The flow rate increased by an average value of 2.5% while the pressure was increased from 0.21 MPa to 0.84 MPa. It seems that the rates do not significantly depend on the discharge pressure. However, the conveying rate decreased 15.5% for flakes at 24 rpm with an increasing pressure from 0.21 MPa to 0.84 MPa. It seems that the flow rate does not have a simple relationship with the discharged pressure. We know that friction force plays an important role during the extrusion process, and it is a complex function of the temperature and the pressure (Chapter 3). PVC flakes have the largest friction force among the three types of PVC considered. Friction force are sensitive to high pressure and will decrease as the pressure increases.

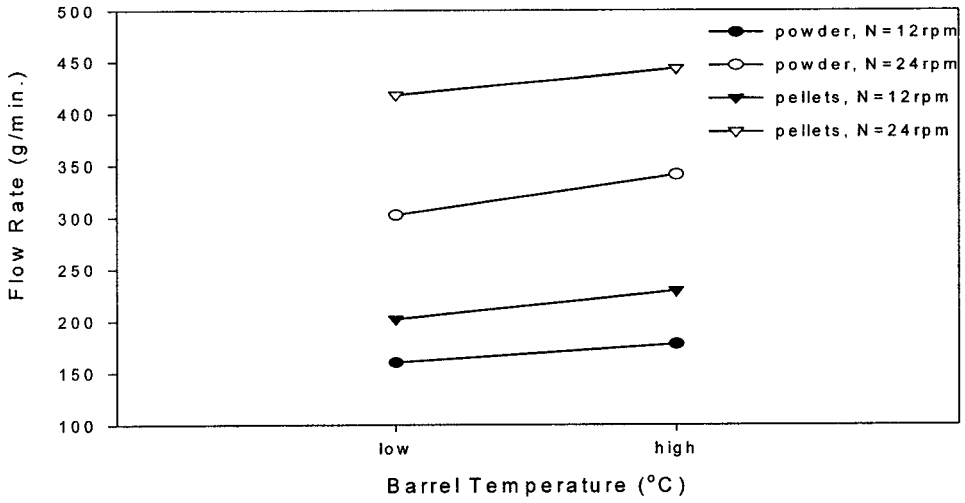

(A) Effect of the barrel temperature (applied pressure=0.48 MPa, low temperature=70°C~80°C, high temperature=130°C.

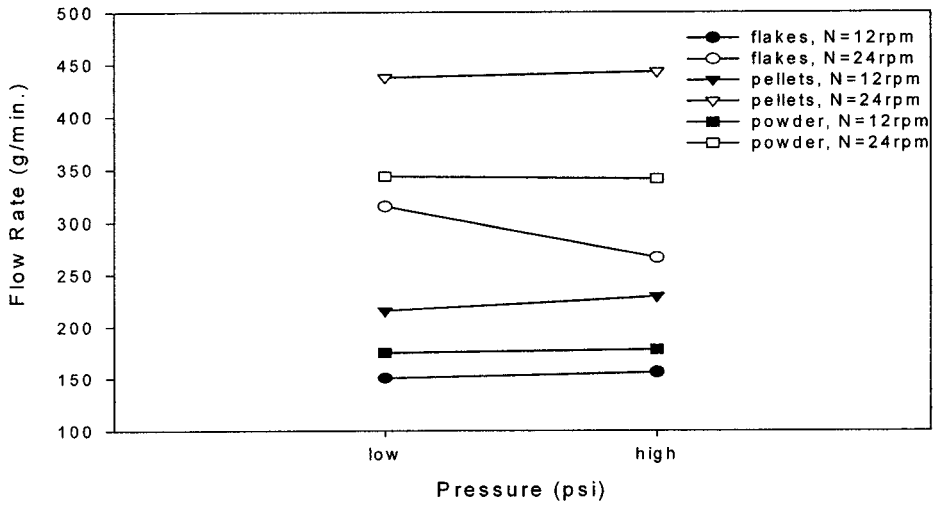

(B) Effect of the applied pressure (temperature=130 °C, low pressure=0.21 MPa, high pressure=0.48 MPa).

Figure 5.8 Flow rate comparison for the three shapes of PVC

5.4 Comparison with numerical results

5.4.1 Parameters used in model simulations

Solids conveying rates and pressure build-up at different operation conditions were calculated using the models. Our model was compared to Tadmor-Broyer model combined with Schneider's theory. The input geometric and operational parameters for the models are: helix angle, channel height, channel length, flight thickness, channel width, barrel diameter, rotational speed. (table 5-2 and 5-3.)

Table 5- 3 Geometric values used in simulations

Extruder barrel diameter (m)	D_b	0.445
Extruder length (m)	L	0.37
Thickness of flight (m)	e	0.006
Helix height (m)	H	0.009
Width of the screw (m)	W_b	0.0385
Helix angle (°C)	θ_b	17.6

It was found that the friction coefficients have a very strong effect on the resulting pressure and temperature variation in the extruder. The larger the difference between f_b and f_s the earlier the compaction, and the temperature rise. When f_b and f_s are equal, the pressure does not increase, confirming the need to use a rough barrel surface for improving the compaction of the polymer material. The friction coefficients f_b (between the polymer particles and the barrel surface), f_s (between the polymer particles and screw surface), as well as f_i (between the polymer particles) were estimated by using curve fits

with both temperature and pressure (Appendix III). Lower limits on the friction coefficients were assumed as temperatures or pressures exceeded the range of the experimental data. The lower limits of friction coefficient were chosen very carefully according to the coefficients trend. For example, at P=8.8 MPa, the COF decreased very slightly for temperatures above 90°C, therefore we considered a constant COF for higher temperature. Mathematic models of COF are shown in chapter 3.4.2.

Splading et al (1997) showed that the compaction behavior of the resin is another important factor for modeling the solids conveying. The bulk density of a polymer at ambient condition depends on the particle size on shape and on the solid density of the material. When a pressure is exerted on solid particles, they rearrange and deform to fill void spaces. They further pack or break (in case of brittle polymers) while under pressure. The bulk density is also a function of material temperature. At high temperature, the bulk modulus of the material will decrease and the particles will deform more easily at a given pressure, leading to an increase in the bulk density. It was found that the bulk densities of three shapes PVC were different. The deviations of the bulk densities depend on the void volume of the bulk material. Higher void volume leads to lower bulk density. For PVC powder, flakes and pellets, powder has the highest bulk density and pellets and flakes have the similar bulk densities. The bulk density of PVC is a function of pressure and temperature (Gamache, 1999) and corrected by PVC shape parameters in the simulation. It is described by the following equation:

$$\rho = -710 * e^{-0.00498+0.00372*T-6.929e-5*T^2*P} + 1420 \qquad 5\text{-}1$$

(Temperature: °C; Pressure: MPa.)

5.4.2 Tadmor-Broyer model modified by lateral stress ratio

Splading et al. (1997) used a one-dimensional compression cell to measure the lateral stress ratio K defined as the ratio of the compressive stress in horizontal direction to the compressive stress in the axial direction. The lateral stress ratio can be related to the pressure in the solids conveying as follows:

$$K = \frac{pressure \quad at \quad barrel(screw) \quad surface}{pressure \quad in \quad the \quad helical \quad direction} = \frac{P_b (or P_s)}{P_z} \qquad 5\text{-}2$$

z represents the down channel direction. However, as shown in figure 5.7, the compaction load of the solids conveying is triaxial. Therefore the experimental measurements are a simplification of the real mechanism. Obtaining accurate values using triaxial testing may be difficult.

Experience in the field of soil mechanics indicated that the lateral stress in granular media can be determined from shear strength parameters obtained from different types of laboratory tests (GoGos, et al., 1994). Data obtained by Splading, (1997) showed that K value of polymers with pelletized forms exhibit widely varying trends with increasing temperature, depending on the nature of the polymer. However, contact area is another important factor. Experiments utilizing a pressure transducer to measure the horizontal stress in the polymer specimens have been performed. The surface area of most pressure transducers is not large enough to effectively measure the average stress in a granular material. The local particle stress may be either much higher or lower than the average stress, depending on how many particles actually rest on the pressure transducer diaphragm. In soil mechanics, where testing of granular materials is routinely performed, a specimen's minimum dimension should measure at least a minimum of 20 grain diameters to eliminate the effect of particles size in a uniformly graded material. With the large size of polymer pellets (for example LDPE pellets), very few grains would actually be in contact with the pressure transducer diaphragm. This limits the

reliability of the method for the evaluation of the average stress. Thus, we believe that the results of lateral stress ratio in the reference may be adversely affected by the experimental method measuring the lateral stress. However, the trends established for variation in temperature and pressure may be correct, but the actual values may be compromised by the stress measuring technique. The test results on polymer powder may be more correct, because the grain sizes are much smaller and thus could be considering as a continuum.

The Tadmor-Broyer model (1972) was modified to include the lateral stress ratio relating the pressure at the surface to the pressure at the center of the channel. The pressures at the interfaces are assumed to be equal to the product of helical pressure (down channel pressure) at the center of the channel and the lateral stress ratio. Equations I-1, and I-8 to 10 of Darnell-Mol model becomes:

$$F_1 = Kf_b PW_b dz_b \qquad 5\text{-}3$$

$$F_3 = Kf_s (PHd\bar{z} + F^*) \qquad 5\text{-}4$$

$$F_4 = Kf_s PHd\bar{z} \qquad 5\text{-}5$$

$$F_5 = Kf_s W_s d\bar{z} \qquad 5\text{-}6$$

The magnitude of the lateral stress ratio is a function of temperature and pressure, as well as measuring device. Since the magnitude of the lateral stress for PVC as a function of temperature and pressure is not known, we used a constant value in each simulation (K is about 0.1~0.9 for polymers). For K=1, the pressures at the metal interfaces are assumed to be equal to the pressure at the center of the channel: it is the standard Tadmor-Broyer model without lateral stress ratio. The value of K was adjusted for each operation conditions in order to fit the experimental data. As a result of the simulation, a

series of computed results of K values are obtained (Appendix IV). We analyze the simulation results of K later in this chapter.

The modified Tadmor-Broyer model was used to predict the pressure, temperature, and solid bed density profiles in the extruder. The initial pressure for the simulation, P_0, at the start of the screw channel, was assumed to be a small. Figure 5.10 show the variation of pressure, temperature and density, in the solid conveying region for the different shapes of PVC at a discharged pressure 0.21 MPa, and a screw speed of N=12 rpm. The variations of the friction factors f_b and f_s as a function of pressure and temperature are discussed in chapter 3.

Figure 5.9 (A) gives the pressure profiles for PVC pellets, powder and flakes. As shown by the experiment the pellets have the biggest pressure build-up, while flakes have the smallest pressure build-up. Consequently, the calculated values of the lateral stress ratio are 0.32 for pellets, 0.29 for powder, and only 0.25 for flakes. Values reported by Spalding (1997) are in 0.3-0.4, and our calculation values are correlative to the experimental values.

Figure 5.9 (B) and (C) show the temperature and density profile for the three types of PVC. The temperature profiles are almost the same for pellets, powder, and flakes. This is because lateral stress ratio K does not relate to thermal effect directly, and the pressure is only one of the factors affecting the temperature profile. For the bulk density profiles, the three shapes of PVC have the same density at the beginning, and density for pellets and powder rises more quickly than for flakes. At the end of the solid conveying region, powder and pellets present similar densities whereas flakes have the smallest density. This result coincides with the pressure profile since the material bulk density is a function of pressure and temperature.

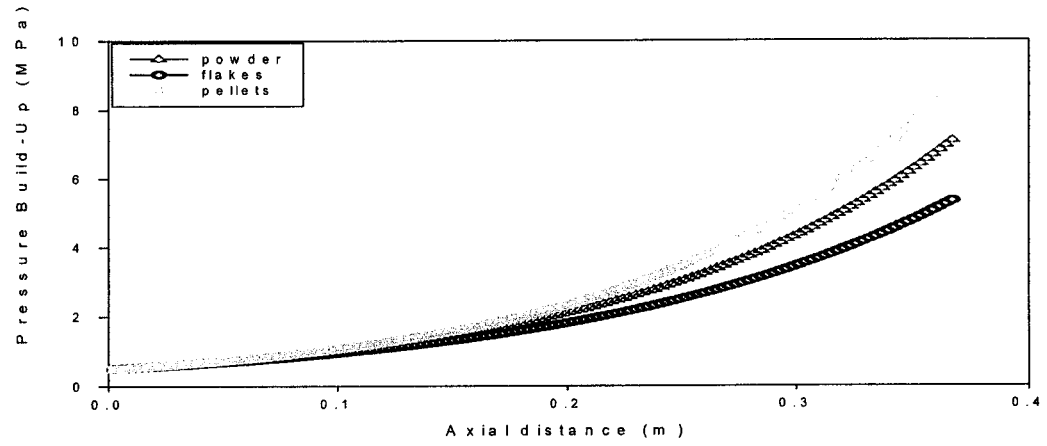

(A)

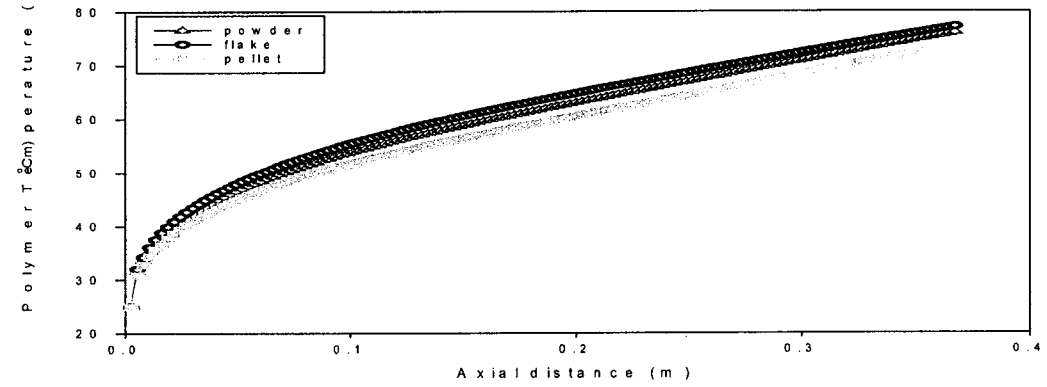

(B)

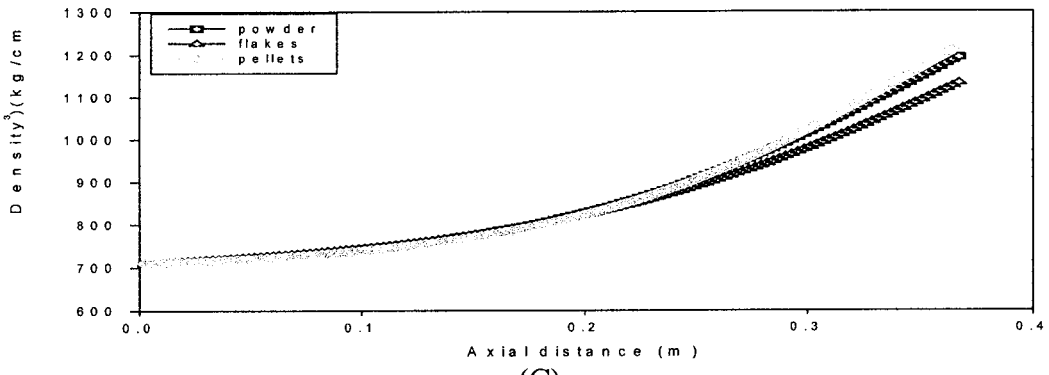

(C)

Figure 5.9: (A) Pressure profiles, (B) Temperature profiles, (C) Density profiles for the three shapes of PVC resin by using modified Tadmor-Broyer model. N=12 rpm, P=0.21 Mpa.

The effect of the screw speed, barrel temperature and discharged pressure on PVC pellets have been examined.

Figure 5-10 (A) shows the pressure profile for pellets at screw speed 12 rpm and 24 rpm, barrel temperature 130°C and 110°C, for two different discharged pressure of 0.21 MPa and 0.48 MPa. The pressure build-up increases with the increased screw speed, barrel temperature, and applied pressure.

Figure 5-10 (B) shows the temperature profile for pellets at different operating conditions. It seems that the modified Tadmor-Broyer model is not sensitive to certain operating conditions. For example, the temperature profiles are practically the same for the two rotational speed and applied pressure. At relative low barrel temperature (110°C), polymer has lower temperature to that at high temperature (130°C). According to thermal theory, we expect a higher temperature as N or applied P, are increased.

Figure 5.10 (C) shows the density profile. Density is a function of local pressure and temperature, and will increase when pressure and temperature increase.

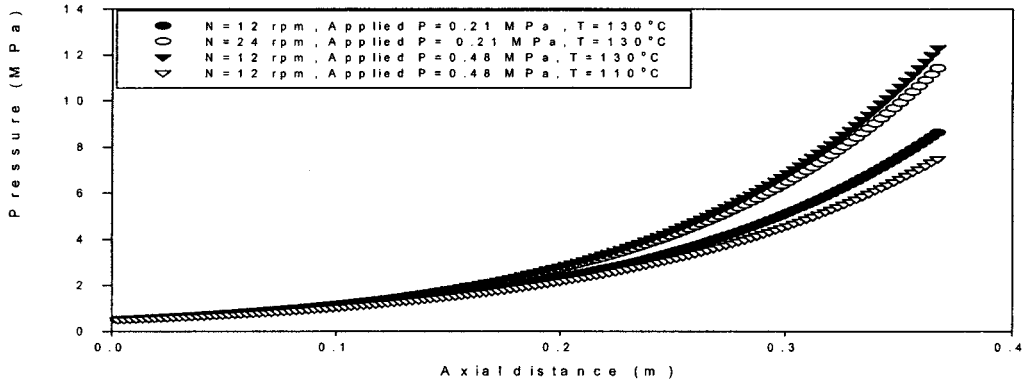

(A)

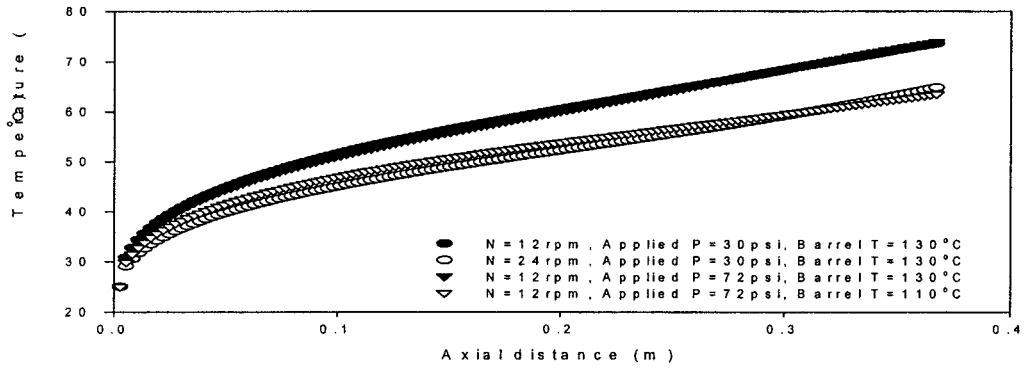

(B)

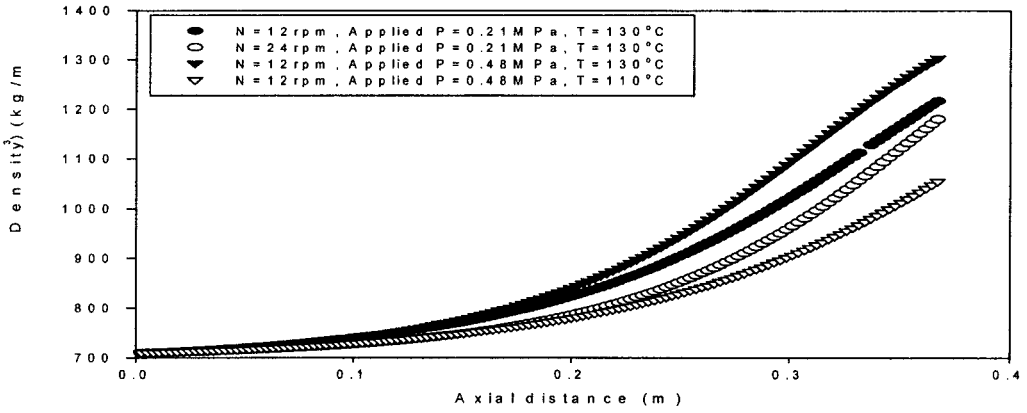

(C)

Figure 5.10 (A) Pressure profiles, (B) Temperature profiles, (C) Density profiles, for PVC pellets at different operating conditions by using modified Tadmor-Broyer model.

Data in literature (Rankine, 1972) indicate that K is affected by test temperature. It is found that K do not reduce in the early period after compacted at a relatively slow speed, and the value of K tends to increase immediately after compaction at a relatively fast speed. The simulation results for PVC pellets verified the experimental data. For example, at barrel temperature 110°C, screw speed 12 rpm, and discharged pressure 0.48 MPa, K=0.3; as temperature raise to 130°C, screw speed and pressure kept unchanged, K value increased to 0.32; as screw speed increased to 24 rpm, temperature kept at 130°C, K value increased to 0.36. For PVC powder, there is no simple relationship between K values and temperature.

It is clear that K_{flakes} $K_{powder} < K_{pellets.}$ A three level factorial design was used to analyze the effect of applied pressure, screw speed and barrel temperature on K. Since flakes could not be processed at low temperature, only pellets and powder were studied in this analysis.

For pellets, temperature, screw speed, and pressure were found to be significant factors affecting K value (figure 5.11 A). K value increases with temperature, pressure and screw speed. The surface graphs are shown in appendix IV.

For powder, only pressure and temperature were found to be significant factors. As shown in figure 5.11(B), K increases with the pressure and decreases as temperature is raised.

It seems that lateral stress K does not only depend on operating conditions, but also on material shape, size, and characteristics. Therefore, K is a complex function of all the above factors.

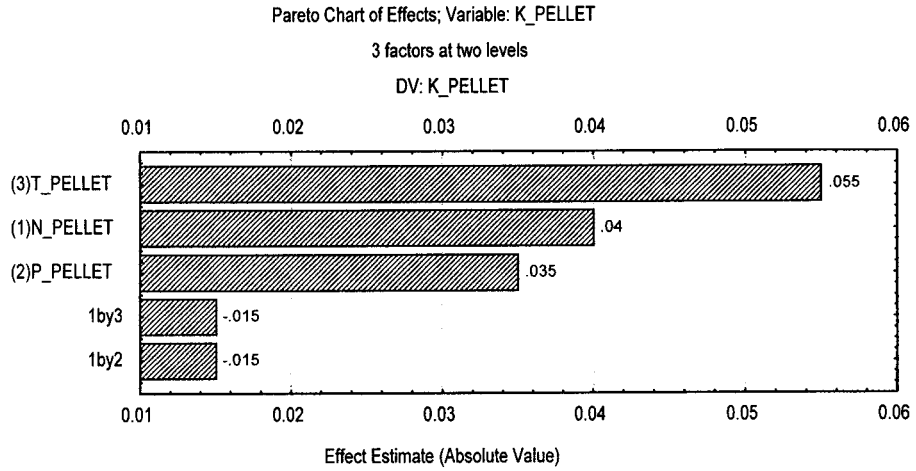

(A)

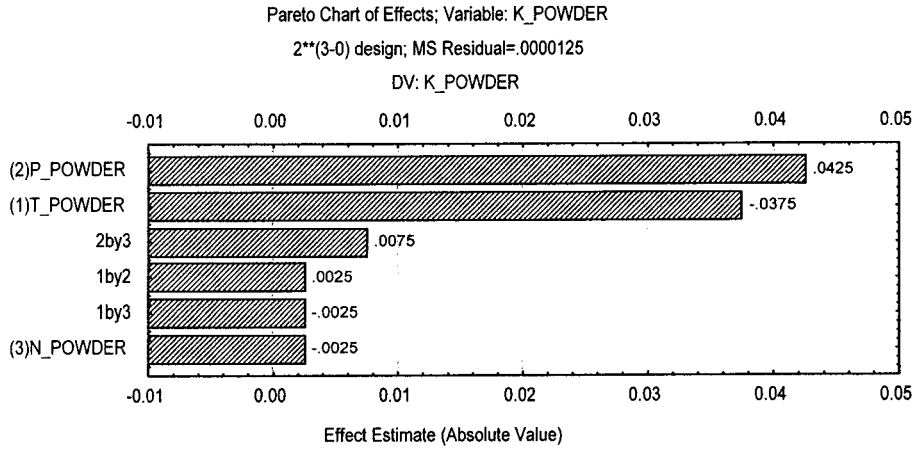

(B)

Figure 5.11: Statistic analysis pareto chart of effects for lateral stress ratio K. (A) pellets (B) powder.

5.4.3 A new non-plug solid flow model

This new model incoporates two new parameters: internal frictional force and material shear modulus. Our observations demonstrated the existence of relative motion between polymer granules during the extrusion. Actually, internal friction is dominant over the relative motion between solids granules, and should be taken into account in the mathematical model. Furthermore, we consider the solid material in the screw channels as bulk pellets instead of a "rigid solid plug". According to the elastic mechanism theory, when a solid is subjected to stress, it deforms a fixed amount independent of time. On removal of stresses, the elastic solid recovers instantaneously and completely to its original state. Thus the stiffness or elasticity modulus E, which is the relation between stress and deformation (strain), is unique for a solid. In shear, the stress τ causes a deformation dx in the direction of the stress, however, the strain is very small (figure 5.12), and shear strain is defined as:

$$\frac{dx}{dy} = \tan\gamma \cong \gamma \qquad 5\text{-}7$$

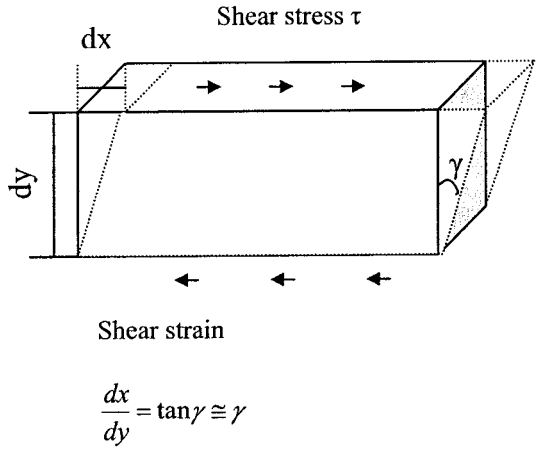

Figure 5.12 Shear strain

Shear modulus G (modulus of rigidity) is defined as τ/γ. It is affected by material shape, surface characteristics, temperature, and pressure. G is very difficult to measure, and we do not know the magnitude of the shear modulus for PVC as a function of temperature, pressure, and screw speed, a constant G value was used in all the simulation. The value of G was fitted for every operation condition in order to obtain the test results for flow rate and pressure build-up.

Simulations were performed using the new non-plug solid flow model just like we did before for the modified Tadmor-Broyer model. As shown in figure 5.13 (A), the pressure profile for three shapes of PVC is similar to the results from modified Tadmor-Broyer model. That is to say: $P_{pellets} > P_{powder} > P_{flakes}$, and the simulation results showed that pellets have the highest shear modulus value G, 6.1e+4 Pa at screw speed N=12 rpm and applied pressure P=0.21 MPa. Powder has an intermediate value, G=3.8e+4 Pa, and flakes have the smallest shear modulus G=2.5e+4 Pa. Therefore $G_{pellet} >> G_{powder} > G_{flakes}$. The material shear modulus value controlled the pressure build-up at the end the extruder. For the temperature profile, the three shapes of PVC present similar curves. The local pressure increases exponentially in the down channel direction, so will the rate of heat generation. This will usually lead to a nearly exponentially increasing temperature profile as well, although of course, the temperature will also depend on the rate of heat removed by conduction through the barrel wall and rate of barrel cooling. Figure 5.13 (C) indicated that the bulk density curves for the three shapes of PVC were similar. Bulk density is a function of local pressure and temperature, and also shows an exponential increase.

Figure 5.14 (A) and (B) show the pressure and temperature profile for different operating conditions. As expected, the pressure and temperature increase more rapidly at higher rotation speed. Similarly, applied pressure and barrel temperature affected the two profiles. A larger speed results in greater frictional force between the PVC particles

and extruder surfaces, leading to earlier compaction. The inner barrel temperature and material bulk temperature start increasing before the heated zone of the extruder is reached. This is caused by the friction heat generation at the interface. We know that the higher the speed, the larger the pressure and larger the heat generation. At very low speeds, the polymer temperature does not rise until the heated zone is reached. A larger applied pressure results in earlier compaction of polymer particles and larger heat generation. A higher barrel temperature makes the polymer particles softer and easy to be compacted. Of course, the higher barrel temperature results in higher material temperature.

Simulation results of G were analyzed by means of a statistic program. The Pareto's charts of effect are shown in figure 5.15 (A) and (B). Only pellets and powder were studied just as we did for K values. For pellets, temperature, pressure and screw speed were found to be significant factors, shear modulus G increased with the increasing of temperature, pressure, and screw speed. (Figure 5.15 A) For powder, the significant factors were the same than for pellets, G value increased as pressure increased, but decreased as temperature or screw speed increased (see appendix IV). These results shown that G, the same as lateral stress ratio K, is a complex function of material shape, size, surface characteristic and operating conditions.

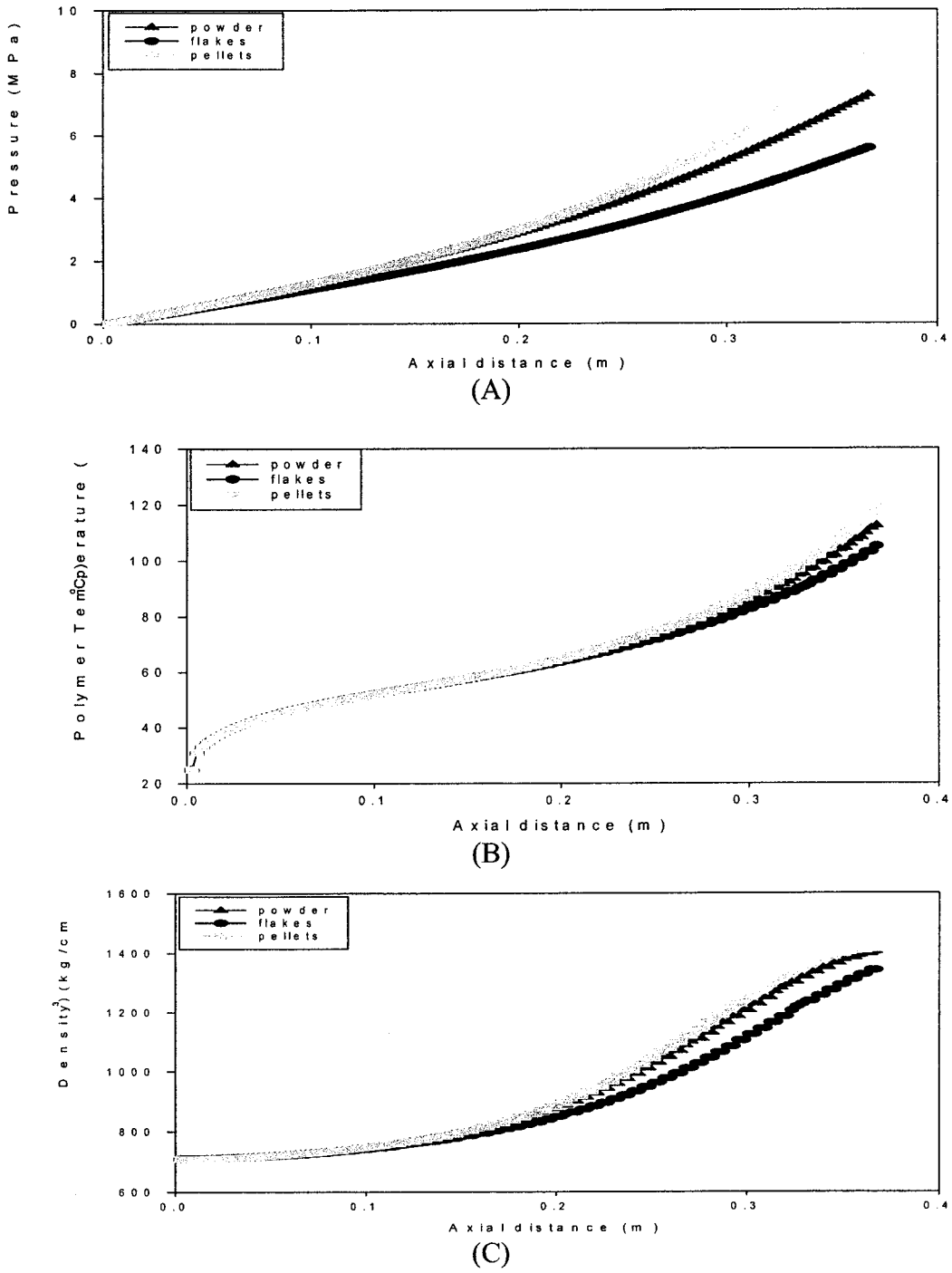

Figure 5.13: (A) Pressure profiles, (B) Temperature profiles, (C) Density profiles, for three shape of PVC resin by using new non-plug solid flow model.

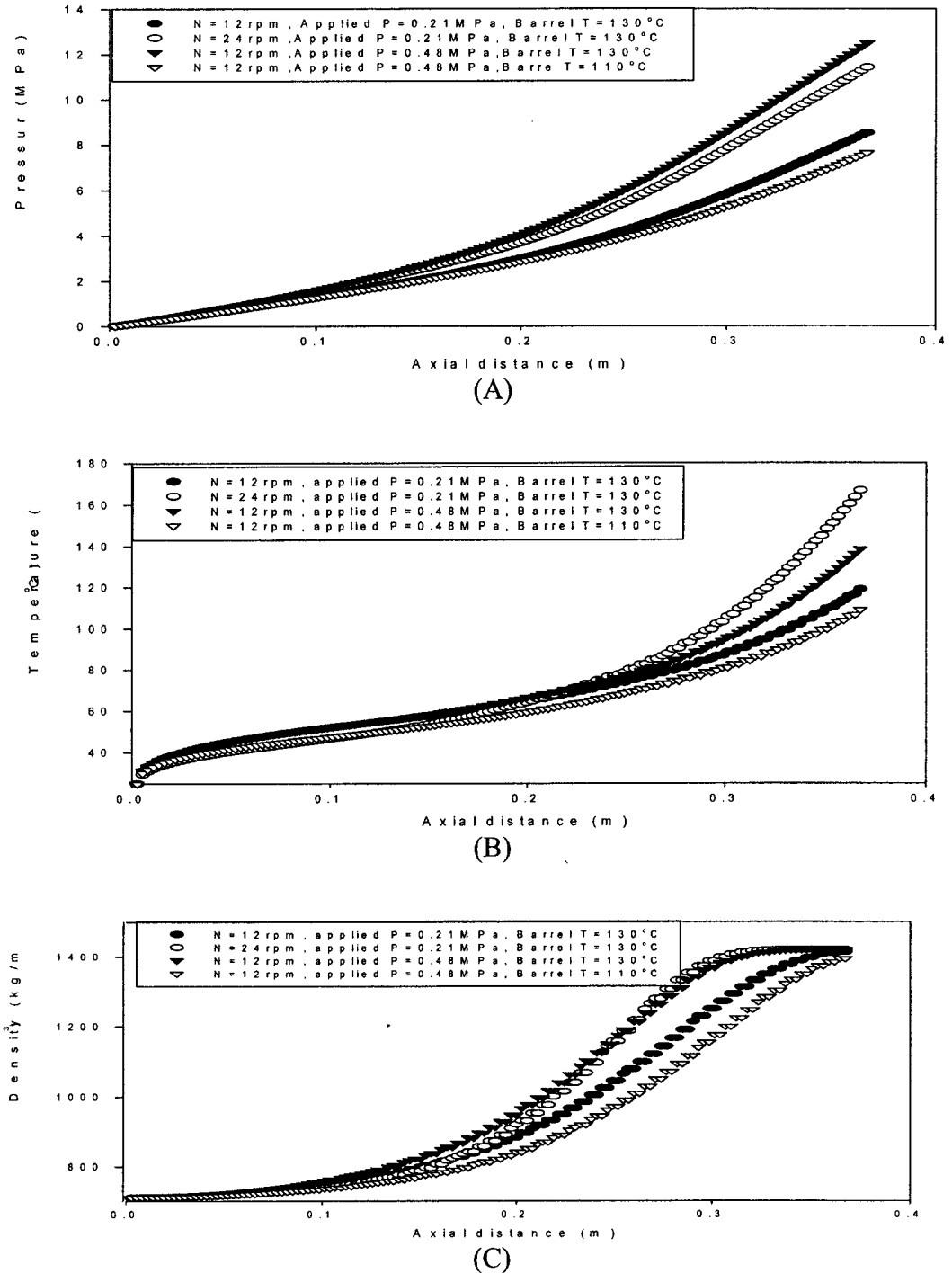

Figure 5.14: (A) Pressure profiles, (B) Temperature profiles, (C) Density profiles, for PVC pellets at different operation conditions by using new non-plug solid flow model.

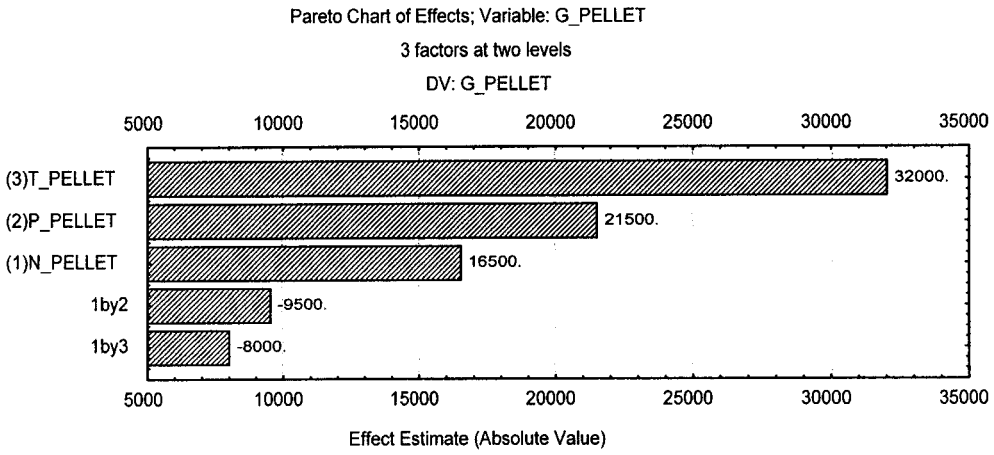

(A)

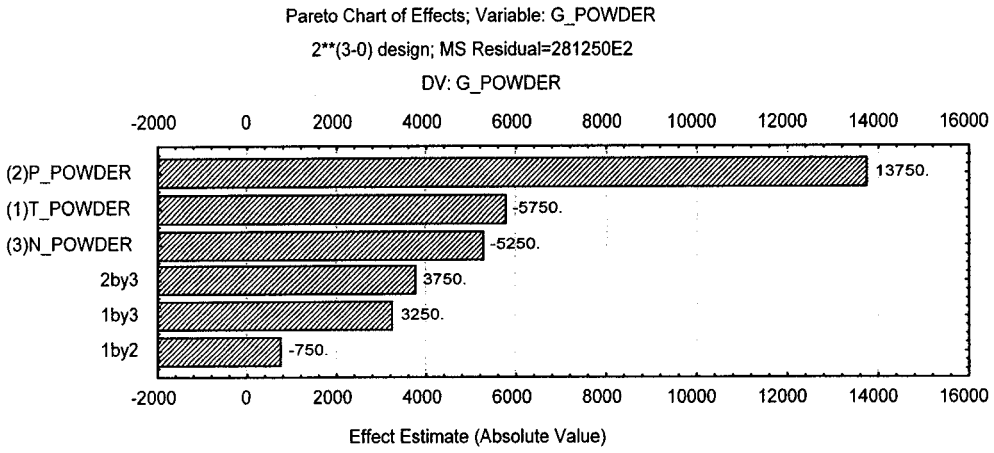

(B)

Figure 5.15: Statistic analysis pareto chart of effect for shear modulus G. (A) pellets (B) powder.

Due to the total lack of information on the values of the material shear modulus, which occurred in our model, we cannot tell whether it is. However, the simulation results also gave us some information about shear modulus G.

5.4.4 Comparison of two models

The measured temperature at the end of the screw was compared to the calculated one using Tadmor-Broyer and Non-plug flow model. The measured temperature is underestimating a little bit the temperature at the end of the solids conveying section. We believe that the true value will be a little higher than the measured one. Table 5-4 shows that the Non-plug model over predict the temperature while the Tadmor-Broyer has a tendency to under predict.

Table 5- 4: Comparison of experimental mass temperature and simulation temperature at the end of screw.

	Screw speed (rpm)	Measured P at end of screw (MPa)	Measured mass T at the end of screw (C)	Calculated T (T-B-S) C	Calculated T (Non-plug) C
Flakes	12	5.52	105	77	105
	24	6.89	110	67	132
	12	9.05	119	79	121
	20	12.00	116	72	161
Pellets	12	8.40	115	74	119
	24	11.39	119	65	167
	12	12.42	122	74	138
	24	13.15	112	65	183
Powder	12	7.20	124	76	112
	24	6.96	122	66	133
	12	10.28	117	77	127
	24	10.34	120	68	159

T-B-S: Tadmor-Broyer model modified by Schneider's lateral stress ratio

Non-plug: new non-plug flow model

As indicated by figure 5.16, the Tadmor-Broyer model, including the lateral stress ratio, show a lower pressure build-up than that of the new non-plug solid flow model along the solids conveying region. The end pressure is the same since the shear modulus and lateral stress ration were fitted to obtain the experimental value. Broyer-Tadmor's non-isothermal model indicated that the exponentially increasing pressure leads to a nearly exponentially surface temperature profile; an incorrect pressure profile will cause low or high-predicted temperature profile. The calculated mass temperature at the end of the screw for the modified Tadmor-Boryer model was lower than the experimental results (table 5-4), due to an under predicted pressure profile. Even though the lateral stress ratio was included in Tadmor-Broyer model since stress distributions (or pressure) are anisotropic in polymer compacts. A more detailed analysis of the pressure distribution in the pellets, taking into account the geometry of the channel, may improve the simulation. The new non-plug solid flow model was able to predict a temperature profile closer to the experimental value, and also probably a better pressure profile.

5.5 Conclusion

To verify the new model (Non-plug solids flow for solids conveying), a special extruder that could measure solids conveying rate as a function operation conditions was built. The extrusion behavior of three different PVC resin (powder, pellets and flakes) was observed experimentally. Different compressive situations, as well as different pressure build-up were found. Comparisons also were done between Tadmor-Broyer model with the lateral stress ratios and the new non-plug solid flow model.

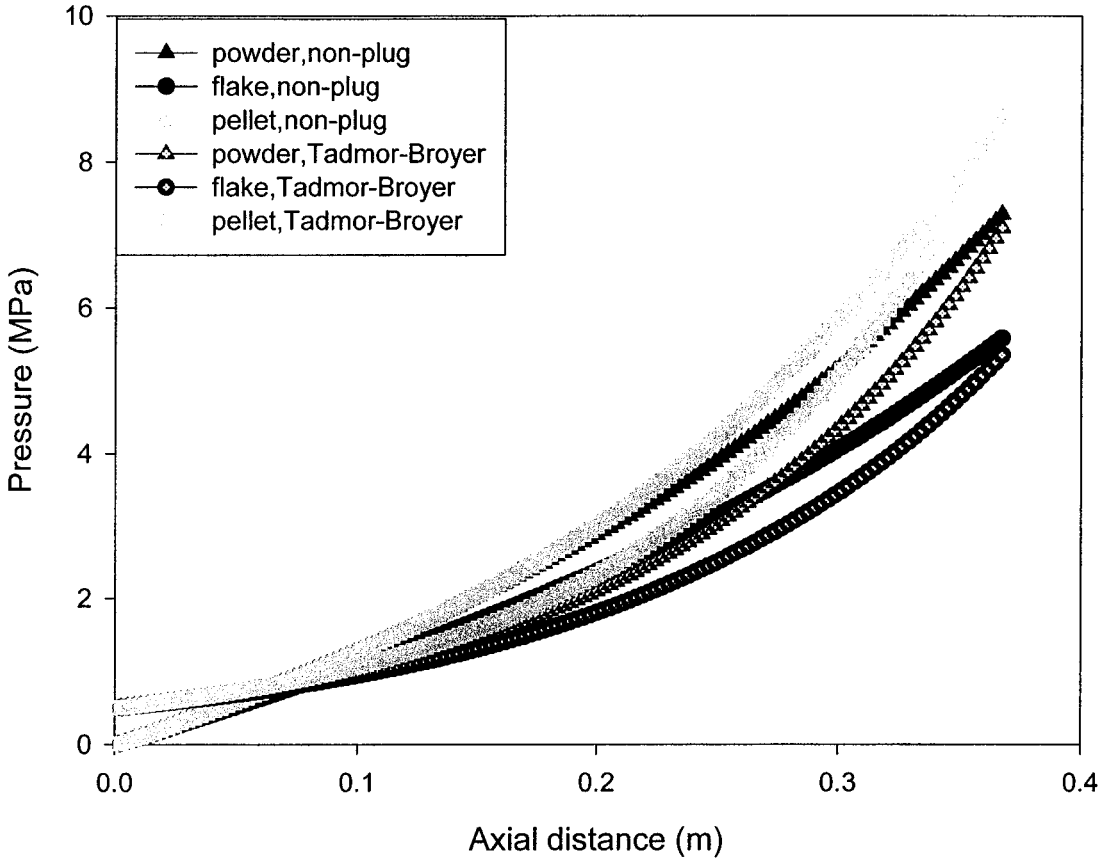

Figure 5.16: Comparison of pressure profiles for modified Tadmor-Broyer model and new non-plug solid flow model.

CHAPTER 6: CONCLUSION AND FUTURE WORKS

6.1 Conclusion

A new friction measurement device was designed for data collection at typical extrusion conditions for three types of plates, representing the polymer/barrel, polymer/screw and polymer/polymer interfaces. The experimental results showed that, for PVC resin, friction factors at barrel and the screw, as well as internal friction decreased with increasing pressure and interface temperature, whereas rotation speed slightly affected friction coefficient. It was clear that the frictional behavior of a polymer depends on temperature, pressure and speed in a complicated manner and can be quite different from one polymer to another. Therefore, a simple extrapolation of the frictional coefficient in terms of temperature, pressure and speed is not recommended.

A new non-plug solid flow model, which allowed material deformation, was introduced in this work. This model is based on the bulk pellets system mechanism combined with a two-dimensional stress analysis on a single element of the solid pellets. A new parameter, G, (material shear modulus) was also introduced since the internal frictional force between polymer and polymer was the dominant force of the relative movement of solid pellets. Taking into account changes in bulk density as material is compressed, changes in frictional behavior as material heats up and compacts, and changes in pressure across the channel, this model can be used to predict the flow rate, pressure build-up, velocity, density profile, as well as temperature profile.

To validate the new non-plug flow model, a device capable of giving detailed information on the compaction and solid bed conveying phenomena in single screws

was designed. Solids conveying rates were measured and shown to be a complicated function of process conditions and of the physical properties of the resin. The complicated effect of the discharged pressure on the solids conveying rate was shown. For the first time, three shapes of PVC resin were studied to describe the compressive situation and solids conveying behavior in single-screw extruders. These data were then used to compare the simulation results of two models: lateral stress modified Tadmor-Broyer model and the new non-plug solid flow model. Moreover, the physical property data affecting solids conveying were measured and used in the simulations.

The simulation data indicated that the Tadmor-Broyer model with the lateral stress ratio under predict the pressure build-up and temperature profile for a given flow-rate. It seems that the simple addition of the lateral stress ratio to the Tadmor-Broyer could not describe the real stress distribution in the extrusion. A more detailed analysis of the anisotropic pressure distribution in the compacted may improve the accuracy of the simulation.

It was shown that the new non-plug solid flow model was in good agreement with the experimental data. Furthermore, this model also gave a better correlation between material shapes and extrusion behavior by introducing a shear modulus G. From the simulation results, it was shown that the shear modulus G is a function of local pressure, temperature, material physical properties (solid granules shape, size, surface characteristics), and extrusion behaviors.

6.2 Future works

There are some recommendations for future works: For the COF measurement, a more powerful heater band is required in order to expand the experimental temperature range,

and the values close to the experimental extrusion temperature. This will improve the accuracy of the simulation results.

The new non-plug solid flow model is based on a two-dimensional stress analysis neglecting the friction force on the screw flight. To make this model more realistic, we should develop a new-plug flow model based on a three-dimensional stress analysis.

Because of the limitations of the COF measurement device, the solids conveying rates were measured at relative low temperatures. More experiments should be performed at higher temperatures in order to understanding the effect of barrel temperature. The material shear modulus is a new parameter introduced in the new non-plug solid flow model and no data are available on the nature of G during extrusion. Experimental data coupled with a statistical plan of experiments could be used to analyze how the operating conditions (temperature, pressure, and screw speed), material physical properties (solid particles shapes, density, surface characteristic) affect the shear modulus.

REFERENCE

Attalla, G., Podio-Guidugli, P., 1980 "On Modeling the Solids Conveying Zone of a Plasticating Extruder", Polym. Eng. Sci., Vol. 20, 709-715.

Broyer, E., Tadmor, Z., 1972 "Solids Conveying in Screw Extruders Part I: A modified Isothermal Model", Polym. Eng. Sci., Vol. 12 12-24.

Campbell, G. A., Dontula, N., 1995 "Solids Transport in Extruders", Intern. Polymer Processing X 1 (1995) 30-35.

Campbell, G. A., Wang, C., 1996 "The Use of Video and the Development of Solids Conveying Theory", ANTEC '96/3595-3600.

Chung, C. I., 1970 "conveying in Screw Extruders ", SPE Journal, Vol. 26, 33-44.

Chung, C. I., 1971 "Plasticating Single-Screw Extrusion Theory", Polym, Eng. Sci., Vol. 11, 93-98.

Chung, C. I., Hennessey, W. J., Tusim, M. H., 1977 "Frictional Behavior of Solid Polymers on a Metal Surface at Processing Conditions", Polym. Eng. Sci. Vol. 17, 9-20.

Darnell, W. H., Mol, E. A. J., 1956, Soc. Plastics Eng. J., 12 20.

De Witt, D.P., Incropera, F. P., 1996 "Fundamental of heat and mass transfer", John Wiley & Sons.

Fang, S., Chen, L., Zhu, F., 1991 "Studies on the Theory of Single Screw Plasticating Extrusion. Part II: Non-Plug Flow Solid Conveying", Polym. Eng. Sci., Vol. 31, 1117-1122.

Fisher,E. G., 1976 "Extrusion of Plastic"

Gamache, E., Lafleur, P. G., 1999 "Measurement of the Coefficient of Dynamic Friction at Extrusion Processing Conditions", Polym. Eng. Sci. Vol. 39, 1604-1613.

Gogos, C. G., Zafar, M., Sebastian, D., Todd, D. B., 1994 "A Device to Study Solids Compaction and Conveying in Single Screw Extrusion", ANTEC '94, 288-292.

Hyun, K. S., Spalding, M. A., 1990 " Bulk Density of Solid Polymer Resins as a Function of Temperature and Pressure", Polym. Eng. Sci. Vol. 30, 571-576.

Hyun, K. S., Spalding, M. A., Hinton, C. E., 1997 "Theoretical and Experimental Analysis of Solids Conveying in Single-Screw Extruders", Journal of Reinforced Plastics and Composites, Vol. 16, 1210-1219.

Jaluria, Y. Liu, Y., Chiruvella, R. V., 1999 "Modeling and Simulation of the Solids Conveying and Unfilled Regions in Polymer Extrusion", Journal of Reinforced Plastics and Composites. Vol. 18, 15-26.

Kirkpatrick, D. E., Hyun, K. S., Chung, C. I., 1993 "Friction and Its Effect on the Mechanical-to-thermal Energy Conversion During Extrusion of Poly(Vinylidence Chloride)", Polym. Eng. Sci. Vol. 33, 1261-1269.

Liu, C., O'Brien, K. T., 1991 "The Interparticulate Friction Behavior of Acetal Copolymer Pellets With Biobal and Trilobal Cross-Section", Polym, Eng. Sci. Vol. 31, 1637-1646.

Lovegrove, J. G. A., 1974 "Pressure Generation Mechanisms in the Feed Section of Screw Extruders", Polym. Eng. Sci., Vol. 14, 589-594.

Potente, H., Pohl, T. C., 2001 "Simulation and Analyses of the Polymer-Pellet-Flow into the first Section of a Single Screw", ANTEC 2002.

Schneider, K., 1969 "Technical Report on Plastic Processing in the Feeding Zone of an Extruder", Chemie Ing. Tech., 41, 364-371

Shoot, K. V., 1952 Proc. Roy. Soc., 212, 488.

Simonds, H. R., Weith, A. J., and Schack, W., 1952 "Extrusion of Plastics, Rubber, and Metals", New York, Reinhold Publishing Corp.

Smith, N. M., Parnaby, J., 1980 "Bulk Density Versus Hydrostatic Pressure Characteristics of Plastics in Powder and Pellet Form", Polym. Eng. Sci. Vol. 20, 830-833.

Spalding, M. A., Strand, S. R., 1992 "Modeling of the Solids-Conveying Section of a Starve-Fed Single-Screw Plasticating Extruder", Plastics Engineering, July.

Spalding, M. A., Kirkpatrick, D. E., Hyun, K. S., 1993 "Coefficients of Dynamic Friction for Low Density Polythylene", Polym. Eng. Sci. Vol. 33, 423-430.

Spalding, M. A., Hyun, K. S., 1995 "Coefficients of Dynamic Friction as a function of Temperature, Pressure, and Velocity for Several Polyethylene Resins", Polym. Eng. Sci. Vol 35, 557-562.

Spalding, M. A., Hyun, K. S., Jenkins, S. R., Kirkpatrick, D. E., 1995 "Coefficients of Dynamic Friction and the Mechanical Melting Mechanism for Vinylidene Chloride Copolymers", Polym. Eng. Sci. Vol. 35, 1907-1916.

Spalding, M. A., Hyun, K. S., Hughes, K. R., 1997 "Stress Distribution in Solid Polymer Compacts", Journal of Reinforced Plastics and Composites. Vol. 16, 1231-1240.

Stevens, M.J., Covas, J.A., 1995 "Extruder Principles and Operation".

Tadmor, Z., Broyer, E., 1972 "Solids Conveying in Screw Extruders Part II: Non-Isothermal Model ", Polym, Eng. Sci., Vol. 12 378-386.

Tadmor, Z., Klein, I., 1970 "Engineering Principle of Plasticating Extrusion", Van Nostrand, New York.

Tedder, W., 1971 "A New Theory of Solids Conveying in Single Screw Extruder", SPE J., 27, oct., 68-73.

Trumbull, W. A., Hyun, K.S., Kling, T. J., 1984 "Peletize VDC resin improves processing", Modern Plastic, December 1984.

Umeya, K., Hara, R., 1978 "Rheological Studies of Compaction for Polystyrene Powder", Polym. Eng. Sci. Vol. 18, 366-371.

Yamamuro, J. A., Penumadu, D., 1998 "Modeling Solids Conveying in Polymer Extruders", Intern. Polymer Processing XIII (1998) 1 3-8.

Zhu, F., Chen, L., 1991 "Studies on the Theory of Single Screw Plasticating Extrusion. Part I: A New Experimental Method for Extrusion", Polym. Eng. Sci., Vol. 31, 1113-1116.

Appendix I

1. Darnell-Mol model

The force and torque balance of Darnell-Mol model (figure 2-5)

$$F_1 = f_b P W_b dz_b \qquad \text{I- 1}$$

F_1 may be broken up into two components:

$$\begin{cases} F_{1l} = f_b P W_b dz_b \sin\phi \\ F_{1\theta} = f_b P W_b dz_b \cos\phi \end{cases} \qquad \text{I- 2}$$

Since the pressure gradient dp/dz is uniform across the plug at any given z, the net force F_6-F_2 due to the pressure drop in the down channel direction:

$$F_6 - F_2 = H\overline{W}dp \qquad \text{I- 3}$$

This force can also be broken up into an axial and a tangential component. These will respectively be:

$$\begin{cases} (F_6 - F_2)_l = H\overline{W}dp \sin\overline{\theta} \\ (F_6 - F_2)_\theta = H\overline{W}dp \cos\overline{\theta} \end{cases} \qquad \text{I- 4}$$

F_7 and F_8 are the forces that the flights exert on the plug. They are both normal to the flights.

$$F_8 = PHd\bar{z} \qquad \text{I- 5}$$

$$F_7 = PHd\bar{z} + F^* \qquad \text{I- 6}$$

F_7 is composed of two terms, one equal to F_8, and the other, an additional normal force, F*.

The components of these opposing two forces, F_7 and F_8, in the axial and tangential directions are:

$$(F_7 - F_8)_l = F^* \cos\bar{\theta}$$
$$(F_7 - F_8)_\theta = F^* \sin\bar{\theta} \qquad \text{I- 7}$$

F_3, F_4, F_5, are the friction forces on the two flights and on the root of the screw:

$$F_3 = F_7 f_s = (PHd\bar{z} + F^*) f_s \qquad \text{I- 8}$$

$$F_4 = F_8 f_s = PHd\bar{z} f_s \qquad \text{I- 9}$$

$$F_5 = PW_s d\bar{z} f_s \qquad \text{I- 10}$$

Every one of above forces may be broken up into axial and tangential components:

$$F_{3l} = (PHd\bar{z} + F^*) f_s \sin\bar{\theta} \qquad \text{I- 11}$$

$$F_{3\theta} = (PHd\bar{z} + F^*) f_s \cos\bar{\theta} \qquad \text{I- 12}$$

$$F_{4l} = PHd\bar{z} f_s \sin\bar{\theta} \qquad \text{I- 13}$$

$$F_{4\theta} = PHd\bar{z} f_s \cos\bar{\theta} \qquad \text{I- 14}$$

$$F_{5l} = PW_s d\bar{z} f_s \sin\theta_s \qquad \text{I- 15}$$

$$F_{5\theta} = PW_s d\bar{z} f_s \cos\theta_s \qquad \text{I- 16}$$

Since the plug has a constant axial velocity component, the sum of all the forces in the axial direction should be zero:

$$F_{1l} + (F_6 - F_2)_L - (F_7 - F_8)_L + F_{3L} + F_{4L} + F_{5L} = 0 \qquad \text{I- 17}$$

Introduce into Eq.I-17 the above derived corresponding component, one obtains:

$$PW_b dz_b f_b \sin\phi + H\overline{\overline{W}} dP \sin\overline{\vartheta} - F^* \cos\bar{\theta} + (PHd\bar{z} + F^*) f_s \sin\bar{\theta}$$
$$+ PHd\bar{z} f_s \sin\bar{\theta} + PW_s d\bar{z} f_s \sin\theta_s = 0 \qquad \text{I- 18}$$

Defining:

$$A_1 \equiv f_b W_b \sin\phi + 2Hf_s \sin\theta_b + W_s f_s \sin\theta_b \qquad \text{I- 19}$$

$$A_2 \equiv H\overline{W}\sin\overline{\theta} \qquad \text{I- 20}$$

and introducing them into Eq.I-18 one obtains:

$$F^* = \frac{A_1 P dz_b + A_2 dp}{\cos\overline{\theta} - f_s \sin\overline{\theta}} \qquad \text{I- 21}$$

In a similar way a torque balance about the axis of the screw can be made on an element of the plug in Figure 2-5:

$$F_{1\theta}\frac{D_b}{2} - (F_6 - F_2)_\theta \frac{\overline{D}}{2} - (F_7 - F_8)\frac{\overline{D}}{2} - F_{3\theta}\frac{\overline{D}}{2} - F_{4\theta}\frac{\overline{D}}{2} - F_{5\theta}\frac{D_s}{2} = 0 \qquad \text{I- 22}$$

Once again, introducing the previously derived components into Eq. I-22 one obtains:

$$\begin{aligned} &f_b P W_b dz_b \cos\phi D_b - H\overline{W} dP \cos\overline{\theta D} - F^* \sin\overline{\theta D} - (PH d\bar{z} + F^*) f_s \cos\overline{\theta D} \\ &- PH d\bar{z} f_s \cos\overline{\theta D} - PW_s dz_s f_s \cos\overline{\theta}_b D_s = 0 \end{aligned} \qquad \text{I- 23}$$

Defining:

$$B_1 \equiv f_b W_b \cos\phi - 2Hf_s \sin\theta_b \cot an\overline{\theta}\frac{\overline{D}}{D_b} - W_s f_s \sin\theta_b \cot an\theta_s \frac{D_s}{D_b} \qquad \text{I- 24}$$

and

$$B_2 \equiv H\overline{W}\cos\overline{\theta}\frac{\overline{D}}{D_b} \qquad \text{I- 25}$$

and substituting then into Eq. I-23 one obtains:

$$F^* = \frac{B_1 P dz_b - B_2 dP}{\frac{\overline{D}}{D_b}(\sin\overline{\theta} + f_s \cos\overline{\theta})} \qquad \text{I- 26}$$

By eliminating F* from the force and torque balance (Eq.I-21 and Eq. I-26) one obtains:

$$\frac{A_1 P dz_b + A_2 dP}{\cos\overline{\theta} - f_s \sin\overline{\theta}} = \frac{B_1 P dz_b - B_2 dP}{\frac{\overline{D}}{D_b}(\sin\overline{\theta} + f_s \cos\overline{\theta})} \qquad \text{I- 27}$$

Defining

$$K \equiv \frac{\overline{D}}{D_b}\frac{\sin\overline{\theta} + f_s\cos\overline{\theta}}{\cos\overline{\theta} - f_s\sin\overline{\theta}} \qquad \text{I- 28}$$

and substituting it into Eq. I-27 gives

$$A_1 KPdz_b + A_2 KdP = B_1 Pdz_b - B_2 dP \qquad \text{I- 29}$$

which after integration from z_b=0 where P=P_1 to a down channel distance z_b, where P=P_2, becomes:

$$(A_1 K - B_1)z_b = -(A_2 K + B_2)\ln\frac{P_2}{P_1} \qquad \text{I- 30}$$

Eq. I-30 indicates an exponential rise of pressure across the solids conveying zone. Substituting Eqs I-19, I-20, and I-24, and I-25 into Eq. I-30 yields an expression for the pressure drop in terms of the angle Φ:

$$\cos\phi = K\sin\phi + 2\frac{H}{W_b}\frac{f_s}{f_b}K\sin\theta_b + \frac{f_s}{f_b}\frac{W_s}{W_b}K\sin\theta_b + 2\frac{H}{W}\frac{f_s}{f_b}\frac{\overline{D}}{D_b}\sin\theta_b\cot an\overline{\theta}$$
$$+\frac{W_s}{W_b}\frac{f_s}{f_b}\frac{D_s}{D_b}\sin\theta_b\cot an\theta_s + \frac{\overline{W}}{W_b}\frac{H}{z_b}\frac{1}{f_b}\left(K\sin\overline{\theta} + \frac{\overline{D}}{D_b}\cos\overline{\theta}\right)\ln\frac{P_2}{P_1} \qquad \text{I- 31}$$

2. Lovegrove and Williams model

The output of a solids conveying screw is expressed as follows:

$$\frac{Q}{\pi^2 ND^3 RES} = \frac{\tan\alpha\tan\phi_2}{\tan\alpha + \tan\phi_2} \qquad \text{I- 32}$$

Where:

Q = volumetric flow rate

N = rotational screw speed

R = channel depth/screw diameter (h/D)

E = (D-h)/D

s = axial channel width/pitch ratio

Φ_2 = helix angle at barrel surface.

Consideration of the equilibrium of the pressure generating forces along the channel leads to an expression for A in Eq.2-19 of the following form, (this is before body forces are included);

$$A = A_1 k_b - A_2 k_f - A_3 k_s \qquad \text{I- 33}$$

A_1k_b represents the driving force provided by the barrel and A_2k_f, A_3k_s represent the drag from the screw flight and root respectively. k_b, k_f and k_s are lateral stress ratio for barrel, screw flight and root. k is the ratio of the lateral to the axial stress in a compression. Test on granular materials in an enclosed container. Authors defines A_1, A_2 and A_3 as follows:

$$A_1 = \frac{\mu_b(\cos\alpha - K\sin\alpha)}{RE\cos\phi_f(K\tan\phi_f + E)} \qquad \text{I- 34}$$

$$A_2 = \frac{2\mu_f}{st\cos\phi_f} \qquad \text{I- 35}$$

$$A_3 = \frac{\mu_s C * \cos\phi_s(K\tan\phi_s + C)}{RE\cos\phi_f(K\tan\phi_f + E)} \qquad \text{I- 36}$$

and t = pitch/diameter ratio

C = (D-2h)/D

$\mu_{b,s,f}$ = coefficient of friction on the barrel, screw, and flight respectively

Φ_f = helix angle at mean channel depth

Φ_s = helix angle at screw root

$K = E(\sin\Phi_f + \mu_f \cos\Phi_f)/(\cos\Phi_f - \mu_f \sin\Phi_f)$

3. New non-plug solid flow model

From Figure 2-5, one obtains:

$$F_b = f_b * \sigma_B * \cos(\theta + \phi) \qquad \text{I- 37}$$

$$F_s = f_s * \sigma_s \qquad \text{I- 38}$$

F_b and F_s are the frictional force on barrel surface and screw surface. The stress balance along the y direction is:

$$\sigma_B - \sigma_s = \tau_s - \tau_B = F_b - F_s \qquad \text{I- 39}$$

With Eq. I-37,38, Eq. I-39 becomes equation II

$$\sigma_B - \sigma_s = \tau_s - \tau_B = -f_s \sigma_s + f_b \cos(\theta + \phi)\sigma_B \qquad \text{II}$$

Appendix II

Table II.1: Design of experiments for polished steel plate.

No.	Temperature (°C)	P (MPa)	Speed (rpm)	COF values
1	41	4.03	5.0	0.55
2	41	4.03	8.5	0.55
3	41	4.03	12.0	0.55
4	41	8.80	5.0	0.43
5	41	8.80	8.5	0.43
6	41	8.80	12.0	0.42
7	41	13.47	5.0	0.39
8	41	13.47	8.5	0.38
9	41	13.47	12.0	0.35
10	60	4.03	5.0	0.51
11	60	4.03	8.5	0.47
12	60	4.03	12.0	0.47
13	60	8.80	5.0	0.37
14	60	8.80	8.5	0.37
15	60	8.80	12.0	0.36
16	60	13.47	5.0	0.35
17	60	13.47	8.5	0.35
18	60	13.47	12.0	0.34
19	81	4.03	5.0	0.44
20	81	4.03	8.5	0.39
21	81	4.03	12.0	0.39
22	81	8.80	5.0	0.35
23	81	8.80	8.5	0.35
24	81	8.80	12.0	0.34
25	81	13.47	5.0	0.34
26	81	13.47	8.5	0.33
27	81	13.47	12.0	0.32

Table II.2: Design of experiments for rough steel plate.

No.	Temperature (°C)	P (MPa)	Speed (rpm)	COF
1	41	4.03	8.5	0.61
2	41	8.80	8.5	0.50
3	41	13.47	8.5	0.47
4	60	4.03	8.5	0.60
5	60	8.80	8.5	0.48
6	60	13.47	8.5	0.45
7	70	4.03	8.5	0.40
8	70	8.80	8.5	0.39
9	70	13.47	8.5	0.38

Table II.3: Design of experiments for PVC plate.

No.	Temperature (°C)	P (MPa)	Speed (rpm)	COF
1	52.5	0.94	8.5	0.66
2	52.5	1.94	8.5	0.58
3	52.5	2.95	8.5	-
4	60.0	0.94	8.5	0.58
5	60.0	1.94	8.5	0.54
6	60.0	2.95	8.5	0.54
7	67.0	0.94	8.5	0.52
8	67.0	1.94	8.5	0.51
9	67.0	2.95	8.5	0.50

Appendix III

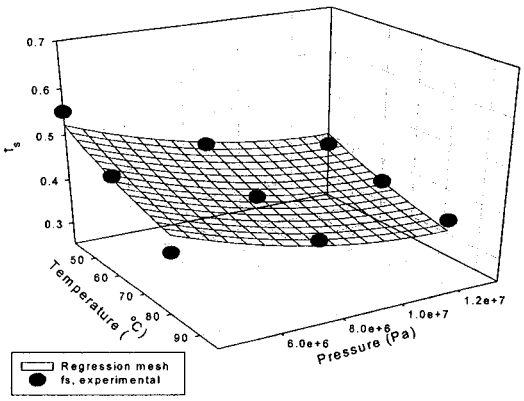

$f_s = 0.8187-(5.249e-3)*T-(3.53e-8)*P+(2.342e-5)*T^2+(1.304e-15)*P^2$

Figure III.1

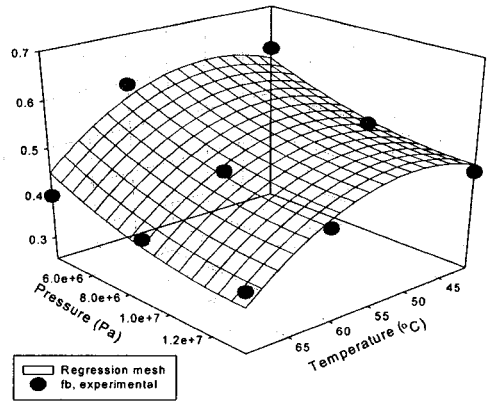

$f_b = -0.2577+(3.927e-2)*T-(3.009e-8)*P-(3.962e-4)*T^2+(1.108e-15)*P^2$

Figure III.2

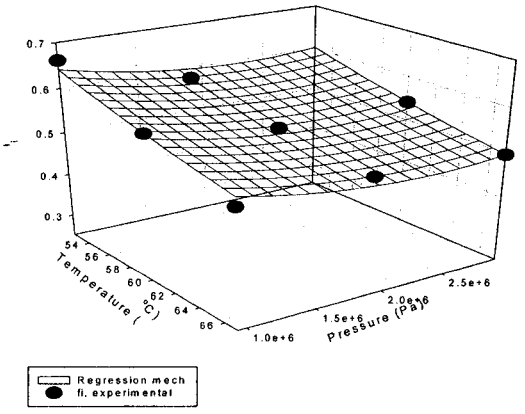

$f_i = 1.478-(1.99e-2)*T-(1.127e-7)*P+(1.073e-4)*T^2+(2.385e-14)*P^2$

Figure III.3

Figure III.1: 3D Regression surface for polished steel plate.

Figure III.2: 3D Regression surface for rough steel plate.

Figure III.3: 3 D Regression surface for PVC plate.

Appendix IV

Figure IV 1: Simulation Results.

	Operation Condition			Measured value		New non-plug		B-T-S	
	T °C	N (rpm)	Air P (psi)	P (Mpa)	Q (kg/s)	P (MPa)	G (Pa)	P (MPa)	K
Flake	130°C	12	32	5.52	0.00251	5.58	2.5e+4	5.3	0.25
		24	32	6.89	0.00525	6.87	3.13e+4	6.62	0.28
		12	70	9.05	0.00260	9.04	3.85e+4	9.63	0.33
		20	70	12.00	0.00444	12.2	5.1e+4	11.95	0.36
Pellets	130°C	12	30	8.40	0.00359	8.5	6.1 e+4	8.6	0.32
		24	50	11.39	0.00729	11.41	7.9e+4	11.4	0.36
		12	70	12.41	0.00382	12.48	9.2e+4	12.30	0.37
		24	70	13.15	0.00738	13.26	9.1e+4	13.20	0.38
Powder	130°C	12	30	7.20	0.00291	7.28	3.8e+4	7.63	0.30
		24	30	6.96	0.00572	7.01	3 .6e+4	7.07	0.29
		12	72	10.28	0.00297	10.17	5.1e+4	10.23	0.34
		24	72	10.34	0.00568	10.13	4.9e+4	10.22	0.34
Powder	82	12.5	40	9.76	0.00293	9.70	5.0e+4	10.15	0.34
	91	24	50	9.26	0.00444	9.38	3.4e+4	9.6	0.33
	86	12	80	12.67	0.00267	12.66	5.7e+4	12.74	0.37
	94	23.7	80	13.91	0.00504	13.86	5.6e+4	13.77	0.38
Pellet	111	12	72	7.58	0.00336	7.61	5.2e+4	7.48	0.30
		24	72	9.98	0.00696	9.92	6.7e+4	9.9	0.34

Figure IV. 2: Statistic analysis results of k value for PVC pellets and powder.

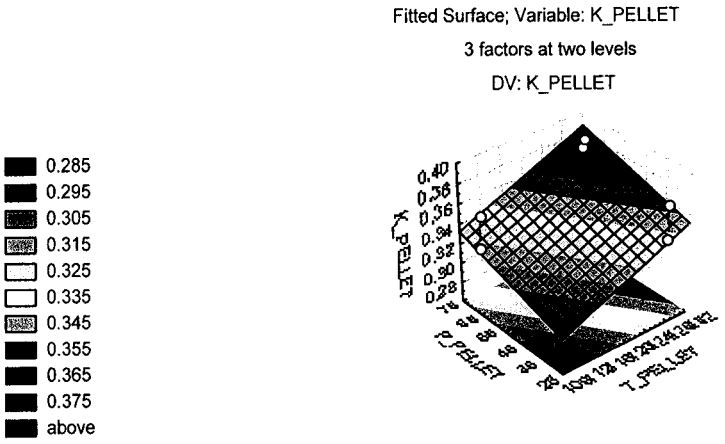

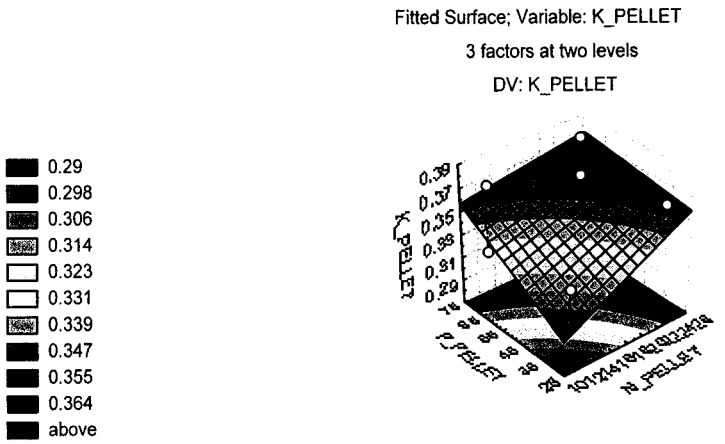

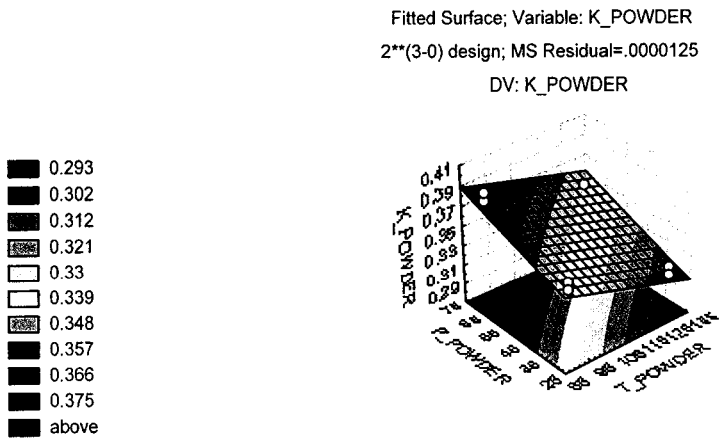

Figure IV. 3: Statistic analysis results of G value for PVC pellets and powder:

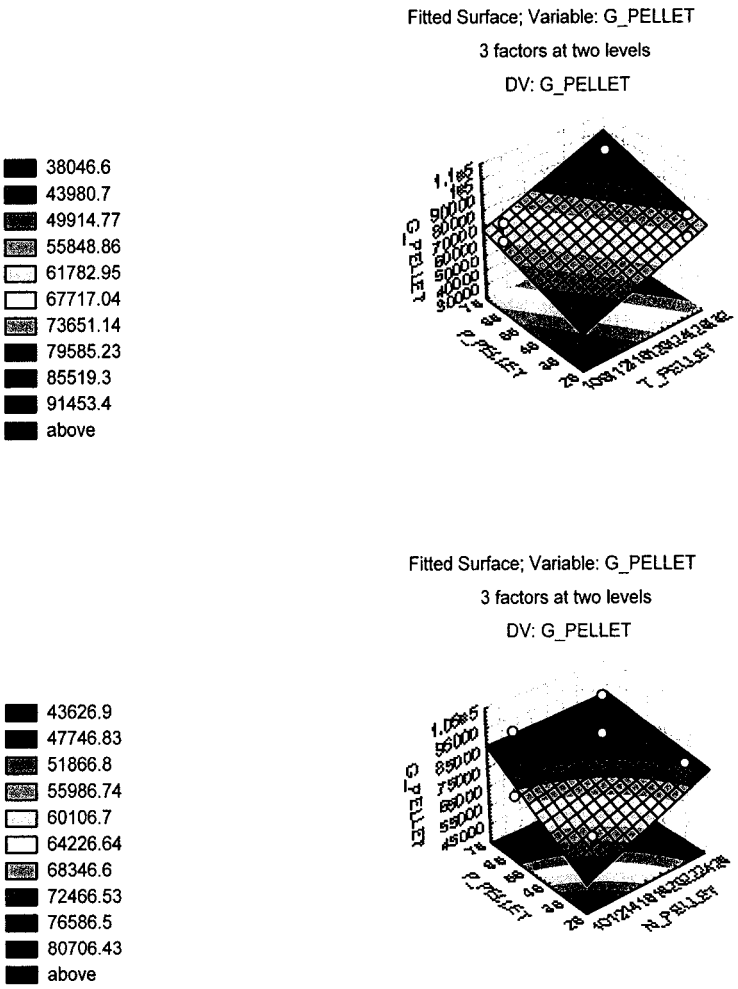

Fitted Surface; Variable: G_POWDER
2**(3-0) design; MS Residual=281250E2
DV: G_POWDER

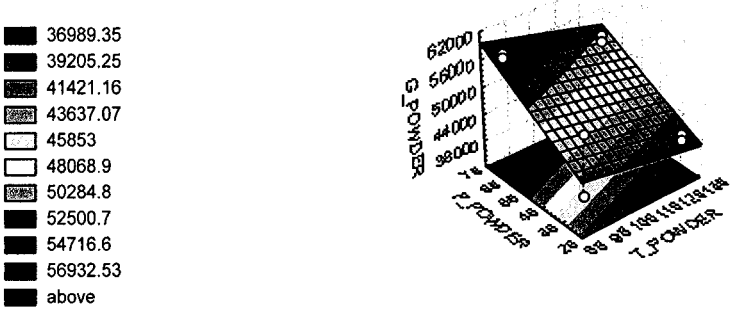

Fitted Surface; Variable: G_POWDER
2**(3-0) design; MS Residual=281250E2
DV: G_POWDER

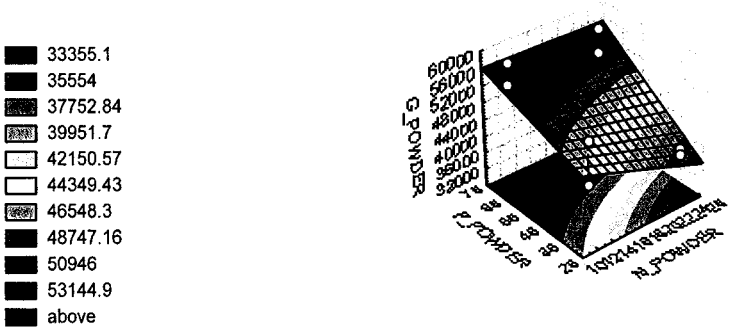

Appendix V

Figure V.1: Mini-screw geometry.

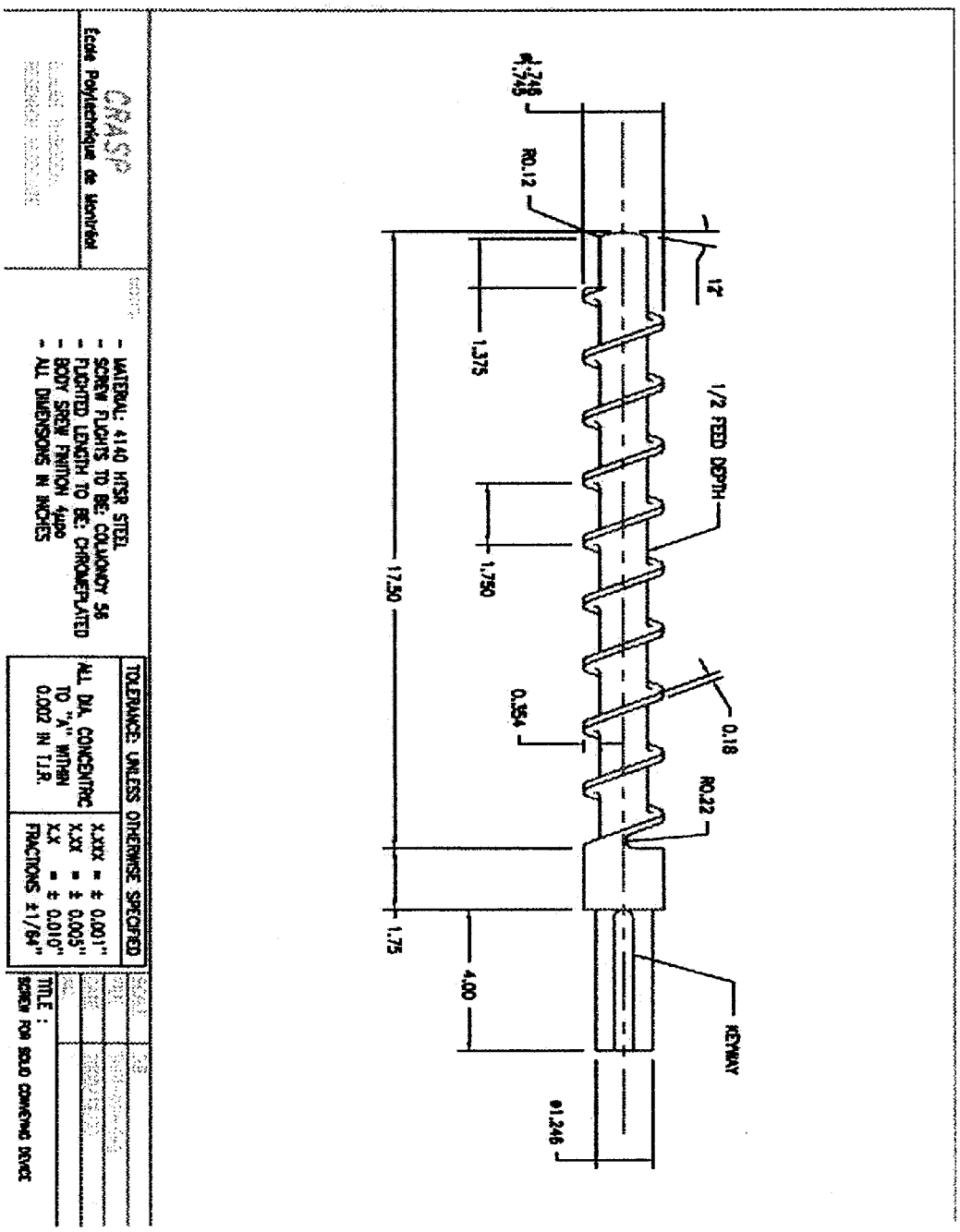

Figure V.2: Screw geometry (large pitch and small pitch).